

# Inhibiting macrophage-derived lactate transport restores cGAS–STING signalling and enhances antitumour immunity in glioblastoma

Received: 30 January 2025

Accepted: 13 November 2025

Published online: 06 January 2026

 Check for updates

Daqi Li<sup>1,2,3,17</sup>, Gaoyuan Cui<sup>1,2,17</sup>, Kailin Yang<sup>4,17</sup>, Chenfei Lu<sup>1,2,5,17</sup>, Yuhang Jiang<sup>1,2,17</sup>, Le Zhang<sup>6,17</sup>, Qiulian Wu<sup>3</sup>, Deobrat Dixit<sup>7</sup>, Zhe Zhu<sup>8</sup>, Ryan C. Gimple<sup>9</sup>, Danling Gu<sup>1,2</sup>, Jiancheng Gao<sup>1,2</sup>, Qiankun Lin<sup>1,2</sup>, Hang Yu<sup>1,2</sup>, Zhumei Shi<sup>5</sup>, Yun Chen<sup>2</sup>, Qianghu Wang<sup>2</sup>, Guangfu Jin<sup>2</sup>, Fan Lin<sup>1</sup>, Junfei Shao<sup>10</sup>, Qigang Zhou<sup>11</sup>, Chong Liu<sup>12,13</sup>, Chaojun Li<sup>2</sup>, Yongping You<sup>5</sup>, Nu Zhang<sup>14</sup>, Junxia Zhang<sup>5</sup>, Xu Qian<sup>2,15</sup>, Qian Zhang<sup>1,2</sup>, Jeremy N. Rich<sup>3</sup> & Xiuxing Wang<sup>1,2,5,11,16</sup>

Glioblastoma (GBM) is a malignancy with a complex tumour microenvironment (TME) dominated by GBM stem cells (GSCs) and infiltrated by tumour-associated macrophages (TAMs) and exhibits aberrant metabolic pathways. Lactate is a critical glycolytic metabolite that promotes tumour progression; however, the mechanisms of lactate transport and lactylation in the TME of GBM remain elusive. Here we show that lactate is transported from TAMs to GSCs via MCT4–MCT1. TAMs provide lactate to GSCs, promoting GSC proliferation and inducing lactylation of the non-homologous end joining protein KU70 at lysine 317 (K317), which inhibits cGAS–STING signalling and remodels the immunosuppressive TME. Inhibition of lactate transport or targeting the lactylation of KU70, in combination with the immune checkpoint blockade, demonstrates additive therapeutic benefits in immunocompetent xenograft models. This study unveils TAM-derived lactate and lactylation as critical regulators in GSCs to enforce an immunosuppressive microenvironment, opening avenues for developing combinatorial therapy for GBM.

Glioblastoma (GBM) is an aggressive primary brain tumour with rapid invasion and proliferation, showing poor prognosis despite advances in surgery and radiochemotherapy<sup>1–3</sup>. The average survival of patients is only 14–16 months, with the 5-year survival rate under 5% (refs. 4,5). GBM stem cell (GSC) is a subpopulation of cells that possess stem cell properties, including self-renewal, differentiation and tumour formation<sup>6,7</sup>. Intrinsic genetic aberrations in GSC shape the tumour microenvironment (TME) by promoting

angiogenesis and immune suppression, thereby driving tumour growth and progression<sup>8</sup>.

The TME is a specialized ecosystem supporting the tumour growth and invasion, containing neoplastic cells, vascular components, immune populations, extracellular matrix and soluble factors<sup>9–11</sup>. The aberrant metabolism of tumour cells triggers metabolic reprogramming in immune populations, resulting in an immunosuppressive milieu impacting immunotherapy efficacy<sup>12–14</sup>. Tumour-associated

A full list of affiliations appears at the end of the paper. ✉ e-mail: [zjx232@njmu.edu.cn](mailto:zjx232@njmu.edu.cn); [xqianmedres@njmu.edu.cn](mailto:xqianmedres@njmu.edu.cn); [zhangqian01@njmu.edu.cn](mailto:zhangqian01@njmu.edu.cn); [drjeremyrich@gmail.com](mailto:drjeremyrich@gmail.com); [drxiuxingwang@163.com](mailto:drxiuxingwang@163.com)

macrophages (TAMs) are the predominant immune population and contribute to the immunosuppressive hallmarks of GBM<sup>15,16</sup>. However, their metabolic interplay with tumour cells remains underexplored.

Lactate is a metabolic byproduct in the tumour metabolism, as identified by previous studies on the Warburg effect<sup>17,18</sup>. Lactylation, a lactate-induced post-translational modification, links lactate to proteins via lactyl-CoA and regulates gene expression and protein activity<sup>19,20</sup>. As a signalling metabolite, lactate undergoes transmembrane shuttling via monocarboxylate transporters (MCTs). Lactate delivered by MCT1 drives Snail-mediated lactylation, promoting endothelial-to-mesenchymal transition<sup>21</sup>. MCT1–MCT2 mediate lactate efflux and influx in neural stem cells maintaining homeostasis and promoting proliferation<sup>22</sup>. MCT4-mediated lactate secretion polarizes macrophages toward a protumoural phenotype, which suppresses T cell function and blunts anticancer therapy<sup>23</sup>. Tumour-derived lactate drives macrophage polarization toward an M2 phenotype<sup>24</sup>; however, the role of immune cells in shaping TME through lactate transport remains elusive.

Metabolic reprogramming critically regulates genomic and epigenomic stability. DNA damage repair is essential for preserving genomic integrity and underpins the radioresistance of GSC<sup>25,26</sup>. DNA damage repair comprises a complex, multistep cascade among the most lethal lesions, double-strand breaks (DSBs) are repaired by two distinct pathways: error-free homologous recombination (HR) and faster-but-error-prone non-homologous end joining (NHEJ)<sup>27–29</sup>. Lactylation regulates HR-based DNA repair through lactylation of meiotic recombination 11 (MRE11) and Nijmegen breakage syndrome 1 (NBS1), in response to DNA damage<sup>30,31</sup>. The precise role of TME-derived lactate in DNA repair remains to be elucidated.

Here, we demonstrate that lactate transport from TAMs to GSCs promotes GSC proliferation and NHEJ repair. Mechanistically, TAM-derived lactate induces KU70 K317 lactylation in GSCs, which suppresses cGAS–type I IFN signalling to enforce an immunosuppressive TME. Our findings highlight lactate transporters and KU70 lactylation as potential targets for GBM immunotherapy.

## Results

### Lactate metabolism and transporter characteristics in GSCs and TAMs

Lactate, as a key glycolytic metabolite, shapes the TME; however, the scope of its roles across multiple cell types within the TME remains undefined. To uncover the underlying mechanism of lactate metabolism and lactate transmembrane transport in GBM, we assembled a single-cell RNA sequencing (scRNA-seq) dataset (HRA004899) encompassing seven isocitrate dehydrogenase (IDH) wild-type (WT) patients

with GBM samples and concurrently integrated two publicly available scRNA-seq datasets (GSE182109 and GSE256490) for our comprehensive analysis. We observed notable enrichment of the glycolysis pathway in TAMs, particularly in macrophages (in contrast to microglia, which exhibited a low glycolysis signature) and in GSC-like tumour cells (Fig. 1a and Extended Data Fig. 1a). The lactate transmembrane transport signature was highly expressed within macrophages and tumour cells (Fig. 1b,c and Extended Data Fig. 1b,c). Among the six genes involved in lactate transmembrane transport using the The Cancer Genome Atlas (TCGA) GBM dataset, *SLC16A1* and *SLC16A3* were highly enriched in GBM compared with normal brain tissues in TCGA GBM dataset (Extended Data Fig. 1d). Analysis of the scRNA-seq dataset showed that *SLC16A3*, which encodes a transporter that secretes lactate (MCT4), was predominantly expressed in the TAM compartment, whereas *SLC16A1*, which encodes a transporter that imports lactate (MCT1), was enriched in GSC-like tumour cells (Fig. 1d and Extended Data Fig. 1e,f). We further observed a colocalization of MCT1 with the GSC marker, SOX2 (Fig. 1e), and colocalization of MCT4 with a marker for TAM, CD163 (Fig. 1f) in GBM specimens. Analysis of scRNA-seq data revealed a high degree of overlap between *SLC16A1* expression with the malignant cell marker *BSG* (Extended Data Fig. 2a) and *SOX2* (Extended Data Fig. 2b), and *SLC16A3* expression with the pan-macrophage marker *AIF1* (Extended Data Fig. 2c) and *CD163* (Extended Data Fig. 2d). The spatial distribution of *SLC16A1* and *SLC16A3* in GBM was consistent with that of GSCs and TAMs, respectively (Extended Data Fig. 2e). High expression of lactate transmembrane transport and expression of *SLC16A1* and *SLC16A3* showed an association with poor prognosis in patients with GBM datasets (Extended Data Fig. 2f,g).

To verify our hypothesis that GSCs uptake lactate derived from TAMs, we quantified lactate levels in TAM supernatants following transduction with shCONT or shMCT4, observing about a 70% decrease in lactate upon MCT4 depletion (Fig. 1g). We treated GSCs at different ratios with shCONT-TAM or shMCT4-TAM supernatants and measured intracellular lactate (Fig. 1h and Supplementary Fig. 1a,b). Reciprocally, we also monitored the effect of MCT1 knockdown of GSCs for the uptake of lactate from TAM-derived supernatants across the same ratios (Fig. 1i and Supplementary Fig. 1c,d). Our data showed a large amount of the absorbed lactate in GSCs was derived from the secretion from TAMs. The concentration of isotope labelled L-lactate of GSCs after coculture with TAMs was determined using liquid chromatography–mass spectrometry (LC–MS) as shown in (Fig. 1j). TAMs were preloaded with D-glucose (U-<sup>13</sup>C<sub>6</sub>) for 12 h and placed in a transwell chamber with GSCs transduced with shCONT or shMCT1 on the bottom. As expected, GSCs transduced with shMCT1 showed a decreased uptake of <sup>13</sup>C-labelled lactate, supporting their affinity for lactate uptake from TAMs (Fig. 1k). The metabolic flux analysis revealed that

### Fig. 1 | Lactate metabolism and transporter characteristics in GSCs and TAMs.

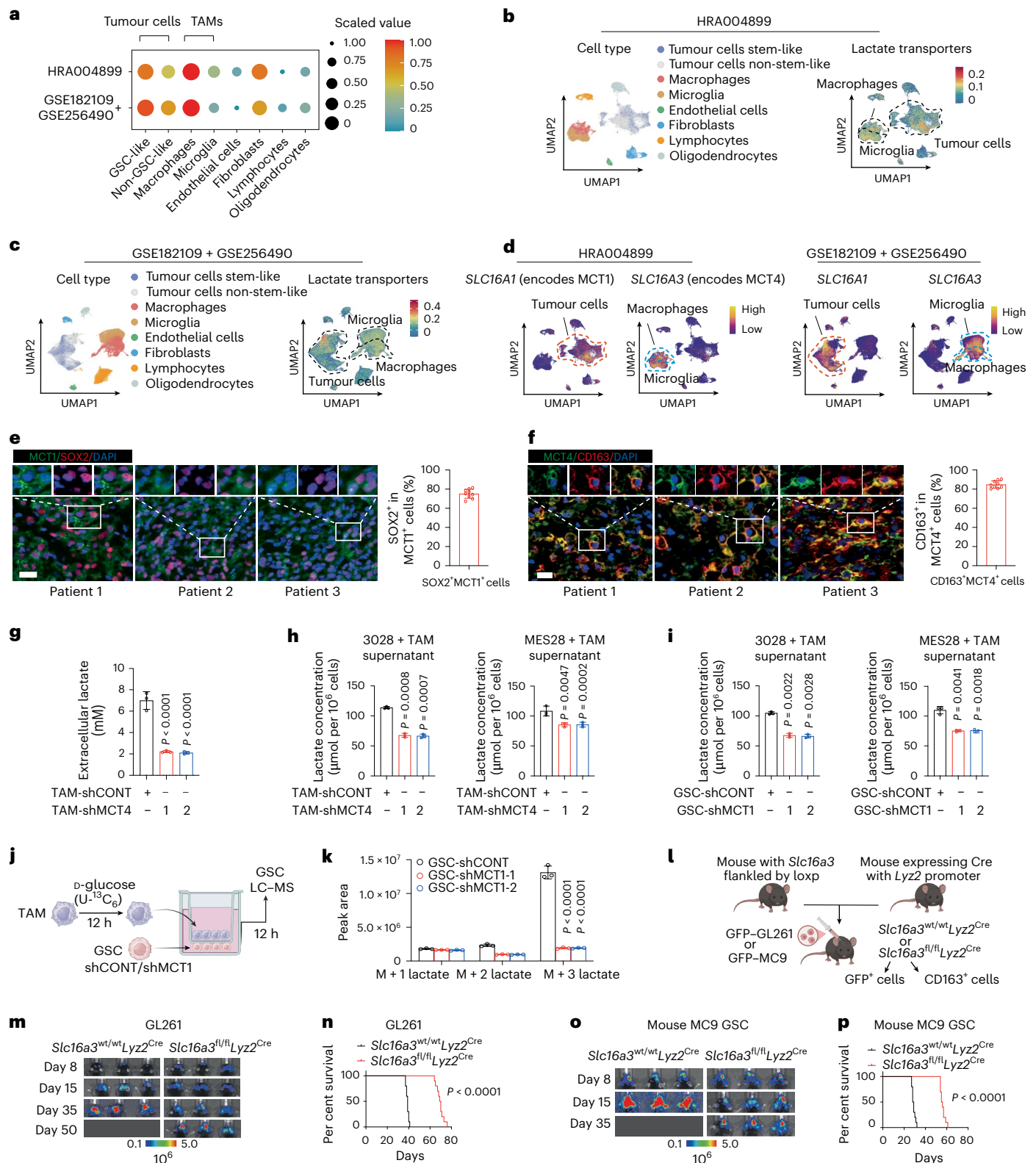
**a**, A dot plot of the analysed HALLMARK\_GLYCOLYSIS pathway in different cell types using scRNA-seq data. **b**, A UMAP dimensional reduction of the basis of the expression pattern of lactate transmembrane transport in cell-type clusters using HRA004899 dataset. **c**, A UMAP dimensional reduction of the basis of the expression pattern of lactate transmembrane transport in cell-type clusters using GSE182109 and GSE256490 datasets. **d**, A UMAP plot showing the expression pattern of *SLC16A1* and *SLC16A3* using scRNA-seq data. **e**, Immunofluorescence staining and quantitative analysis ( $n = 9$  randomly selected fields examined over three GBM samples) shows the fraction of SOX2<sup>+</sup> cells in MCT1<sup>+</sup> cells in patients with GBM from GBM specimens. Scale bar, 50  $\mu$ m. **f**, Immunofluorescence staining and quantitative analysis ( $n = 9$  randomly selected fields examined over three GBM samples) shows the fraction of CD163<sup>+</sup> cells in MCT4<sup>+</sup> cells in patients with GBM from GBM specimens. Scale bar, 50  $\mu$ m. **g**, L-lactate concentration of the supernatant of  $1.5 \times 10^6$  TAMs after transduction with shCONT or shMCT4 from three different patients ( $n = 3$ ). **h**, L-lactate concentration in  $1.5 \times 10^6$  GSCs after treated with supernatant of  $1.5 \times 10^6$  TAMs by transduced with shCONT or shMCT4, as measured by a colorimetric assay ( $n = 3$ ). **i**, L-lactate concentration in  $1.5 \times 10^6$  GSCs after transduction with shCONT or shMCT1 under the stimulation

of supernatant of  $1.5 \times 10^6$  TAMs ( $n = 3$ ). **j**, A schematic model shows the assay performed in **k**. **k**, Fractional abundance of M + 1 lactate, M + 2 lactate and M + 3 lactate in MES28 transducing with shCONT or shMCT1 after coculture with TAMs ( $n = 3$ ). **l**, A schematic model showing the construction of *Slc16a3*-conditional-knockout on myeloid cells. **m**, In vivo bioluminescence imaging of tumour growth was performed in *Ly2z-Cre* with *Slc16a3*<sup>wt/wt</sup> and *Ly2z-Cre* with *Slc16a3*<sup>fl/fl</sup> C57BL/6J mice bearing  $5 \times 10^4$  mouse glioma cell line GL261 on days 8, 15, 35 and 50. The control groups (*Ly2z-Cre* with *Slc16a3*<sup>wt/wt</sup> C57BL/6J mice) on day 50 were dead. **n**, Kaplan–Meier survival curves of immunodeficiency mice with intracranial GL261 in control and *Slc16a3*-knockout groups ( $n = 10$ ). **o**, In vivo bioluminescence imaging of tumour growth was performed in *Ly2z-Cre* with *Slc16a3*<sup>wt/wt</sup> and *Ly2z-Cre* with *Slc16a3*<sup>fl/fl</sup> C57BL/6J mice bearing  $5 \times 10^4$  mouse glioma stem cell on days 8, 15 and 35. The control groups (*Ly2z-Cre* with *Slc16a3*<sup>wt/wt</sup> C57BL/6J mice) on day 35 were dead. **p**, Kaplan–Meier survival curves of immunodeficiency mice with intracranial mouse glioma stem cell in control and *Slc16a3*-conditional-knockout groups ( $n = 10$ ). The data are presented as the mean  $\pm$  s.d. The statistical significance was determined by a two-tailed Student's *t*-test for **g**–**i** and **k** or two-tailed log-rank test for **n** and **p**. Panels **j** and **l** created with BioRender.com.

approximately 55% of lactate was isotopically labelled in the control group, whereas this proportion dropped to 20% in MCT1-knockdown GSCs (Supplementary Fig. 1e). Moreover, the coculture of TAMs with MCT1-knockdown GSCs did not substantially alter the intracellular levels of M+O lactate, indicating that MCT1 perturbation did not influence intrinsic lactate production (Supplementary Fig. 1f).

In addition, C57BL/6J mice were intracranially implanted with mouse MC9 GSC to establish an immunocompetent GBM model. The

stemness of MC9 GSC was confirmed with the stem cell markers Prom1 and Sox2 in both GSC and its differentiated GBM cell (DGC) counterparts (Supplementary Fig. 1g,h). Macrophages and microglia were isolated from brain tissues of tumour-bearing C57BL/6J mice, and extracellular lactate measurements indicated that microglia secreted significantly less lactate than macrophages (Supplementary Fig. 1i). We further constructed the *Slc16a3*-conditional-knockout mice in myeloid cells using *Lyz2*-cre and *Slc16a3*-floxed mice. GFP-labelled GL261



tumour cells or GFP-MC9 GSC were implanted into the cerebral cortex of *Slc16a3<sup>fl/fl</sup>Lyz2<sup>Cre</sup>* and the control *Slc16a3<sup>wt/wt</sup>Lyz2<sup>Cre</sup>* genotype (Fig. 1l). Mice with myeloid-specific *Slc16a3* deletion (*Slc16a3<sup>fl/fl</sup>Lyz2<sup>Cre</sup>*) that were engrafted with either GL261 tumour cells or MC9 GSC exhibited prolonged survival and reduced tumour volume compared with *Slc16a3<sup>wt/wt</sup>Lyz2<sup>Cre</sup>* control (Fig. 1m–p, Extended Data Fig. 2h,i and Supplementary Fig. 1j). GFP-labelled tumour cells were sorted and lactate concentration was quantified, coinciding with the timepoint when the control mice had succumbed. Consequently, we found that lactate concentration in tumour cells markedly decreased (decreased by approximately 40% than control groups) and that lactate accumulation was observed in TAMs in *Slc16a3<sup>fl/fl</sup>Lyz2<sup>Cre</sup>* mice (Extended Data Fig. 2j,k). These data directly support our conclusion that TAM-secreted lactate is taken up by GSCs, which promotes GBM progression.

### Lactate transporting between GSCs and TAMs via MCT1–MCT4 supports GSC proliferation

To investigate the role of lactate in the function of GSC proliferation and self-renewal, we supplemented exogenous lactate within the supernatant of two patient-derived GSCs (3028 and MES28) *in vitro*. We found that GSC proliferation increased in a dose-dependent manner across lactate concentrations from 0 to 10 mM (Fig. 2a). Exposure to other MCT1-transportable monocarboxylates, specifically pyruvate and acetate, did not substantially influence GSC proliferation, whereas  $\beta$ -hydroxybutyrate exhibited a modest inhibitory effect on GSCs, which indicated that among MCT1-transported monocarboxylates, only lactate promotes GSC proliferation (Extended Data Fig. 3a–c). To evaluate TAM-derived lactate, we silenced MCT4 in TAMs and exposed GSCs to their supernatants. Control-TAM supernatant increased GSC proliferation compared with GSC monoculture, whereas MCT4-knockdown supernatant reduced GSC viability. Exogenous lactate or MCT4 re-expression restored both GSC viability *in vitro* (Fig. 2b,c and Extended Data Fig. 3d–f) and tumour growth *in vivo* (Fig. 2d,e), confirming that TAM-secreted lactate promotes GSC proliferation and tumour formation in an MCT4-dependent manner.

Compared with GSCs, DGCs expressed less MCT1 and were unresponsive to TAM-derived lactate (Extended Data Fig. 3g–i). MCT1 knockdown abrogated lactate-induced GSC proliferation, whereas MCT1 re-expression rescued the suppressed proliferation (Fig. 2f,g and Extended Data Fig. 3j). MCT1 knockdown in GSCs impaired TAM-supernatant-mediated stimulation of viability and neurosphere formation; MCT1 re-expression completely rescued GSC proliferation (Fig. 2h,i). To evaluate MCT1 function *in vivo*, we cotransplanted shCONT-GSCs or shMCT1-GSCs with TAMs into xenograft mouse brains, shMCT1-GSCs prolonged survival and reduced tumour volume

compared with shCONT-GSCs, whereas MCT1 re-expression rescued tumour growth (Fig. 2j,k). Seahorse assay revealed that MCT1 disruption in GSCs reduced mitochondrial energy metabolism, accounting for the greater survival benefit versus MCT4 knockdown in TAMs (Extended Data Fig. 3k,l). Collectively, these data establish that lactate promotes GSC proliferation in the TME via the dual role of MCT4-mediated lactate export and MCT1-mediated lactate import.

### TAM-derived lactate promotes GSC proliferation through lactylation of the DNA damage repair protein KU70 at residue K317

Exogenous lactate did not affect the proliferation of non-neoplastic neural stem cells (NSCs) (Extended Data Fig. 4a), and liquid chromatography–mass spectrometry analysis revealed that NSCs uptake less lactate than GSCs (Extended Data Fig. 4b). GPR81 is a G $\alpha$ i/o-coupled receptor that suppresses cyclic AMP (cAMP)–PKA activation in response to acute lactate stimulation<sup>32</sup>. Gene set enrichment analysis (GSEA) using Gene Ontology gene sets of RNA sequencing (RNA-seq) data revealed no significant enrichment for the cellular response to cAMP signalling between GSCs and NSCs<sup>33</sup> (Extended Data Fig. 4c). Moreover, GPR81 knockdown in lactate-treated GSCs did not affect pan-lactylation levels, indicating GPR81 is dispensable for lactylation-dependent functions in GSCs (Extended Data Fig. 4d). We hypothesize that GPR81-independent lactate uptake in GSCs drives lactylation linked to proliferation and oncogenesis.

We then measured the lactylation level in GSCs. GSCs exhibited higher level of lactylation and MCT1 expression compared with NSCs (Fig. 3a). Treating GSCs with shMCT4-TAM supernatant reduced the overall lactylation level compared with the control group (Fig. 3b). Lactate dose-dependently increased GSC lactylation level, whereas MCT1 knockdown blocked this effect (Fig. 3c). These data suggest that the extent of GSC lactylation level is regulated through crosstalk between GSCs and TAMs via the MCT1–MCT4 transporters.

Lactylation profiling and enrichment analysis with mass spectrometry showed NHEJ DNA-repair factors are differentially lactylated in GSCs (Fig. 3d and Extended Data Fig. 4e), with KU70 at the lysine 317 residue (K317) being highly lactylated compared with NSCs, yet total KU70 protein level remained unchanged (Fig. 3e–h). Silencing MCT1 in GSCs reduced KU70 K317 lactylation without altering total KU70 protein level, suggesting that MCT1 regulates KU70 K317 lactylation via modulating lactate levels (Fig. 3i). We constructed KU70 WT and KU70 K317-to-arginine (K317R) to restore KU70 function in KU70-knockdown GSCs and showed that lactylation at K317 promotes GSC proliferation, as assessed with CellTiter-Glo assay and neurosphere formation *in vitro* (Fig. 3j,k and Extended Data Fig. 4f). To examine the *in vivo* function of KU70 K317 lactylation in tumour propagation, we

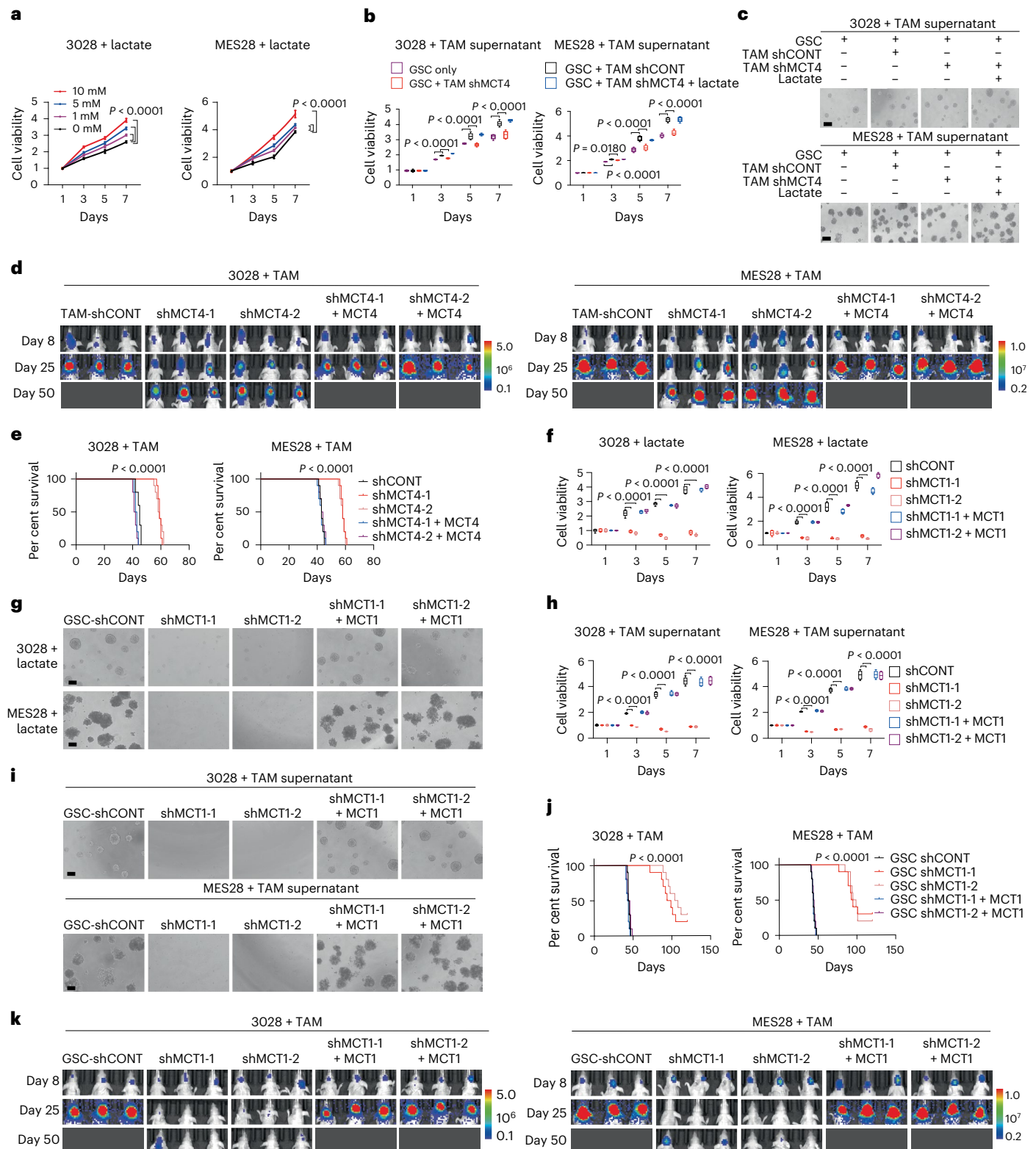
### Fig. 2 | Lactate transporting via MCT1–MCT4 between GSCs and TAMs supports GSC proliferation. a, Cell viability detections after different concentrations (0–10 mM) of lactate-stimulated GSCs. The results were measured by a CellTiter-Glo assay ( $n = 6$ ). b, Cell viability detections of GSCs individually or treated with the supernatant of TAMs transduced with control shRNA or shMCT4 or rescued with lactate ( $n = 6$ ). c, Representative images of neurospheres of 3028 (top) and MES28 (bottom) individually or treated with supernatant of TAMs transduced with control shRNA or shMCT4 or rescued with lactate ( $n = 6$ ). Scale bar, 100 $\mu$ m. d, *In vivo* bioluminescence imaging of tumour growth was performed in nude mice bearing GBM xenografts derived from $5 \times 10^4$ GSCs (3028 and MES28) and $5 \times 10^4$ TAMs transduced with shCONT, shMCT4-1 and shMCT4-2 and rescued by MCT4 on days 8, 25 and 50. The control groups (mice bearing GSCs and TAMs transduced with shCONT and rescued groups) on day 50 were dead. e, Kaplan–Meier survival curves of immunodeficiency mice with intracranial 3028 or MES28 GSCs and TAMs expressing shCONT, shMCT4-1 or shMCT4-2 and rescued by MCT4 ( $n = 10$ ). f, Cell viability detections of GSCs transduced with shCONT, shMCT1-1 and shMCT1-2 and rescued by MCT1 after being stimulated with 10 mM lactate. The results were measured by a CellTiter-Glo assay ( $n = 6$ ). g, Representative images of neurospheres of 3028

and MES28 transduced with shCONT, shMCT1-1 and shMCT1-2 and rescued by MCT1 after stimulated with 10 mM lactate ( $n = 6$ ). Scale bar, 100  $\mu$ m. h, Cell viability detections of GSCs transduced with shCONT, shMCT1-1 and shMCT1-2 and rescued by MCT1 after being stimulated with the supernatant of TAMs ( $n = 6$ ). i, Representative images of neurospheres of 3028 and MES28 transduced with shCONT, shMCT1-1 and shMCT1-2 and rescued by MCT1 after being stimulated with the supernatant of TAMs ( $n = 6$ ). Scale bar, 100  $\mu$ m. j, Kaplan–Meier survival curves of immunodeficiency mice with TAMs and intracranial 3028 or MES28 GSCs expressing shCONT, shMCT1-1 and shMCT1-2 and rescued by MCT1 ( $n = 10$ ). k, *In vivo* bioluminescence imaging of tumour growth was performed in nude mice bearing GBM xenografts derived from  $5 \times 10^4$  TAMs and  $5 \times 10^4$  GSCs (3028 and MES28) transduced with shCONT, shMCT1-1 and shMCT1-2 and rescued by MCT1 on days 8, 25 and 50. The control groups (mice bearing TAMs and GSCs transduced with shCONT and rescued groups) on day 50 were dead. The data are presented as the mean  $\pm$  s.d. In a, the box plots show the median (centre) and the 25th and 75th percentiles (bounds of box), and the whiskers indicate the minimum and maximum values for b, f and h. The statistical significance was determined by a two-tailed Student's *t*-test for a, b, f and h or a two-tailed log-rank test for e and j.

transplanted shRNA-transduced GSCs into the immunocompromised mice. shKU70-GSCs prolonged survival and reduced tumour volume, compared with the complete rescue achieved by KU70 WT, the K317R rescue exhibited only partial recovery, with extended survival and reduced tumour volume (Fig. 3l,m).

In addition to KU70, FEN1 of the base excision repair pathway and LIG1 of the DNA replication pathway are the differentially lactylated proteins (Extended Data Fig. 4e). To investigate whether FEN1 and LIG1

from the base excision repair and DNA replication pathway are necessary for GSC proliferation, we constructed FEN1 or LIG1-WT and FEN1 mutant K201R or LIG1-K226R to rescue the function of FEN1 or LIG1 knock-down. Re-expression of FEN1 WT fully restored proliferation, whereas the K201R did so partially, with no substantial difference in altering phospho-H2AX ( $\gamma$ -H2AX) levels, a marker of DNA damage. Conversely, re-expression of either WT or K226R LIG1 fully restored proliferation and displayed equivalent  $\gamma$ -H2AX levels (Extended Data Fig. 4g–j). These



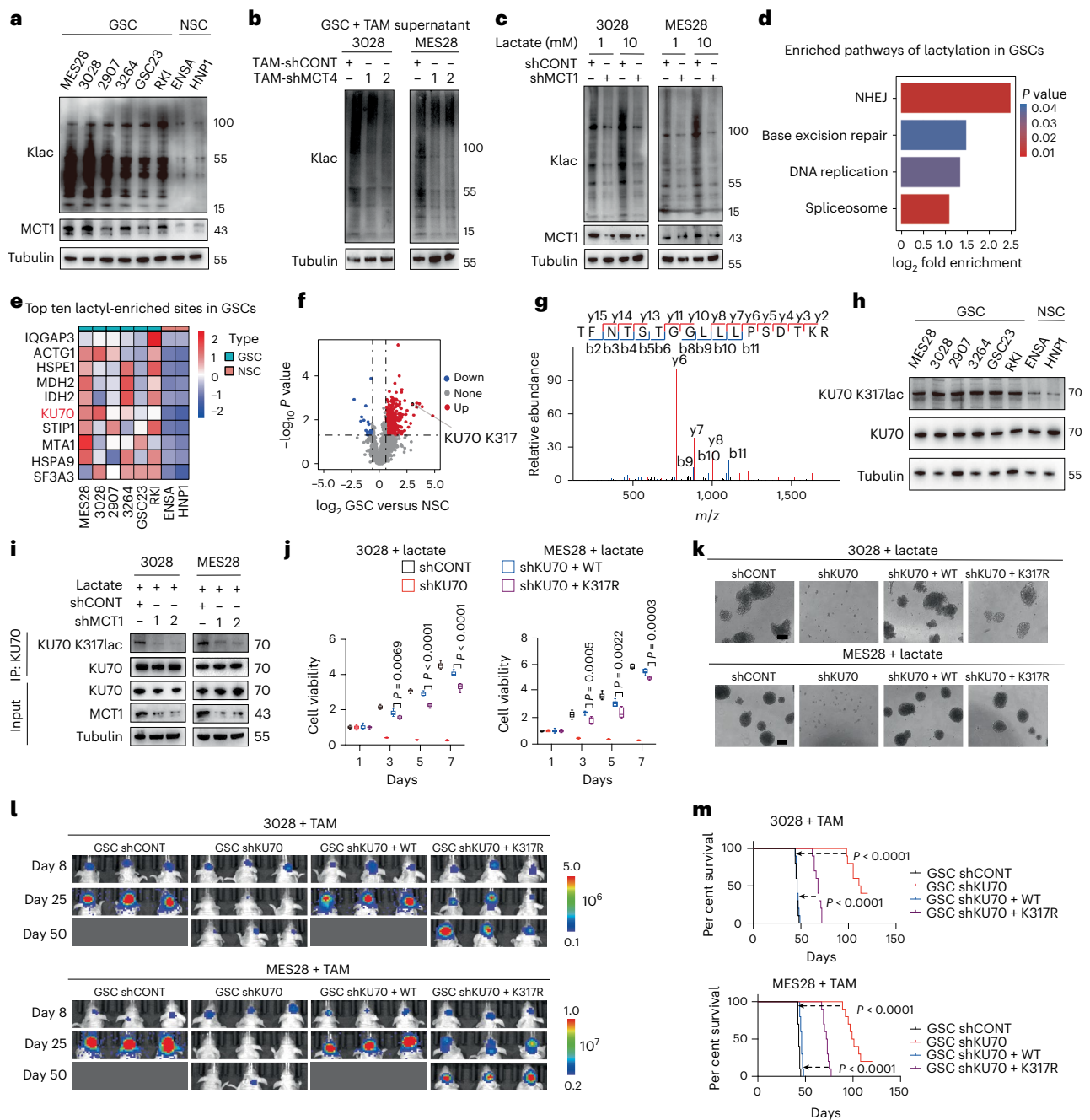


**Fig. 3 | TAM-derived lactate induced the lactylation of DNA damage repair KU70 K317 leads to GSC proliferation.** **a**, An immunoblot analysis of pan-lactylation level in six GSCs and two NSCs after being stimulated with 10 mM lactate. **b**, An immunoblot analysis of pan-lactylation level of 3028 (left) and MES28 (right) after treated with the supernatant of TAMs transduced with control shRNA or shMCT4. **c**, An immunoblot analysis of the pan-lactylation level of 3028 (left) and MES28 (right) after transduction with control shRNA and shMCT1 by stimulating with 1 mM or 10 mM lactate. **d**, Kyoto Encyclopedia of Genes and Genomes signalling pathway analysis of lactylation sites enriched in GSCs detected by mass spectrometry analysis after stimulated with lactate. **e**, A heat map of the top ten lactylated proteins enriched in GSCs. **f**, A volcano plot of differential modification sites in GSCs and NSCs. As indicated by the dotted lines, the cutoff was set as fold change >1.5, *P* value < 0.05. **g**, An illustration of KU70 lactylation at K317, derived from GSC of MES28 identified by mass spectrometry. **h**, An immunoblot analysis of KU70 and KU70 K317lac levels of six GSCs and two NSCs after with lactate. **i**, An immunoblot analysis of KU70 and KU70 K317lac levels after MCT1 knockdown in 3028 (left) and MES28 (right) GSCs by stimulating with 10 mM lactate. **j**, Cell viability detections of GSCs under the stimulation of 10 mM lactate combined

transduced with shCONT, shKU70 and rescued by overexpression of KU70 WT or KU70 K317R after KU70 knockdown. The results were measured by a CellTiter-Glo assay (*n* = 6). **k**, Representative images of neurospheres of 3028 (top) and MES28 (bottom) under the stimulation of 10 mM lactate combined transduced with shCONT and shKU70 and rescued by overexpression of KU70 WT or KU70 K317R after KU70 knockdown (*n* = 6). Scale bar, 100 μm. **l**, In vivo bioluminescence imaging of tumour growth was performed in nude mice bearing GBM xenografts derived from 5 × 10<sup>4</sup> TAMs and 5 × 10<sup>4</sup> GSCs (3028 and MES28) transduced with shCONT and shKU70 and rescued by overexpression of KU70 WT or KU70 K317R after KU70 knockdown on days 8, 25, 50. The control groups (mice bearing GSCs transduced with shCONT) and the groups rescued by KU70 K317R on day 50 were dead. **m**, Kaplan–Meier survival curves of immunodeficiency mice with intracranial 3028 or MES28 GSCs expressing shCONT and shKU70 and rescued by overexpression of KU70 WT or KU70 K317R after KU70 knockdown (*n* = 10). The box plots show the median (centre) and the 25th and 75th percentiles (bounds of box), and the whiskers indicate the minimum and maximum values. The statistical significance was determined by a two-tailed Student's *t*-test for **j** or two-tailed log-rank test for **m**.

indicated that FEN1 lactylation promoted GSC proliferation independently of DNA repair, whereas LIG1 lactylation had no effect on GSC proliferation. Moreover, IQGAP3, the top enriched lactylation protein in GSCs, is required for GSC maintenance, IQGAP3 WT and K981R mutant both rescued GSC proliferation, indicating that site-specific lactylation of IQGAP3 is dispensable for GSC function (Extended Data Fig. 4k,l).

The KU70 K317 residue is conserved among species and we hypothesized that differential lactylation of this residue may alter DNA damage responses and mediate maintenance of key biological functions (Extended Data Fig. 5a,b). P300 was previously reported to catalyse lactylation using lactyl-CoA, which promotes cancer cell proliferation, survival and immune evasion<sup>20</sup>. To differentiate the role of P300 in KU70 K317 lactylation, we generated and validated a site-specific antibody that selectively recognizes lactylation at KU70 K317 (Extended Data Fig. 5c–e), together with another antibody to detect KU70 K317 acetylation. With purified WT and KU70 K317R proteins, we demonstrated that P300 is indispensable for KU70 K317 lactylation but not acetylation, and KU70 K317 acetylation antibody did not recognize this lactylation (Extended Data Fig. 5f–h). The lactylation modified peptide effectively prevented the KU70 K317 lactylation antibody (Extended Data Fig. 5i). Silencing P300 in GSCs led to a reduction in lactate-induced KU70 K317 lactylation without affecting acetylation (Extended Data Fig. 5j). Cell viability and neurosphere formation experiments validated the function of P300 expression (Extended Data Fig. 5k,l).

As reported in the previous study, the KU70 K317 acetylation may potentially be catalysed by the acetyltransferase CREB-binding protein (CBP) or p300/CBP-associated factor (pCAF, also known as KAT2B)<sup>34</sup>. We validated whether CBP or KAT2B can induce KU70 K317 lactylation or acetylation and found that the CBP/KAT2B and acetyl-CoA acetylate KU70 K317 but are dispensable for its lactylation (Extended Data Fig. 5m,n). shCBP or shKAT2B reduced KU70 K317 acetylation without affecting lactylation (Extended Data Fig. 5o,p), suggesting that KU70 K317 lactylation is independent of both factors. Taken together, these data suggest that lactylation of DNA damage repair protein KU70 at K317 promotes GSC proliferation and tumourigenicity.

### Lactylation of KU70 K317 enhances the NHEJ function and maintains the stemness of GSCs

The NHEJ pathway is a critical repair mechanism for DSBs<sup>35</sup>. The KU70–KU80 heterodimer is one of the first complexes to bind broken DNA ends, a critical step to initiate subsequent repair<sup>36</sup>. NHEJ and HR reporter assays revealed that MCT1 silencing impaired the NHEJ pathway in the

presence of exogenous lactate but had no effect on either HR or NHEJ when exogenous lactate is absent (Fig. 4a), demonstrating that GSCs import lactate via MCT1 to promote the NHEJ pathway. MCT1 attenuation in GSCs caused an increase of  $\gamma$ -H2AX, following lactate stimulation or treatment with TAM supernatant, as determined by immunoblotting (Fig. 4b) and immunofluorescence (Fig. 4c). Given the role of KU70 in the NHEJ pathway, we transduced GSCs with shCONT, shKU70 alone and shKU70 rescued by overexpression of KU70 WT or K317R mutant. NHEJ and HR reporter assays confirmed that KU70 lactylation at K317 affected the NHEJ pathway (Fig. 4d). In the absence of exogenous lactate, KU70 K317 lactylation is decreased, whereas its acetylation level remains unchanged (Extended Data Fig. 6a). A difference in NHEJ and  $\gamma$ -H2AX levels between KU70 WT and K317R rescue effects was only observed after exogenous lactate addition (Fig. 4d). KU70 K317 lactylation promoted the NHEJ repair as indicated by the rescue of elevated  $\gamma$ -H2AX levels in KU70-silenced GSCs upon re-expression of KU70 K317R (Fig. 4e,f). COMET assay revealed that KU70 knockdown generated the increased level and longer duration of tail moment compared with control cells. Rescue with KU70 WT or K317R showed that KU70 K317 lactylation is required for efficient repair of large number of DSBs (Extended Data Fig. 6b). KU70 knockdown activated ATM and p53 phosphorylation, increased P21 expression and promoted apoptosis and senescence. Rescue with KU70 WT or K317R indicated that lactylation at K317 suppresses apoptosis and senescence (Extended Data Fig. 6c–e).

To further investigate how KU70 lactylation at K317 in the NHEJ pathway maintains GSC function, we found that MCT1 silencing reduced stemness markers SOX2, OLIG2 and MYC expression following stimulation with lactate (Fig. 4g). Moreover, KU70 K317 lactylation completely rescued the reduction of stemness compared with K317R (Fig. 4h). The neurosphere formation experiment and extreme limiting dilution assays similarly indicated that the MCT1 expression and lactylation level of KU70 K317 correlate to the self-renewal of GSCs (Extended Data Fig. 7a–d). To verify the relationship between NHEJ and stemness of GSCs, we treated GSCs with an inhibitor of NHEJ (NU7441) (Fig. 4i and Extended Data Fig. 7e), which increased DNA damage and negatively impacted GSC stemness.

KU70 is mainly assembled with three domains, the vWA region of the N-terminus, the Ku core region and the C-terminal domain. To identify the specific domain of KU70 that directly binds KU80 to induce downstream of NHEJ pathway, HA-tagged full-length of KU70 (1–609 aa) and three HA-tagged deletion mutants were generated: (1) KU70-HA (1–260 aa), (2) KU70-HA (261–468 aa) and (3) KU70-HA

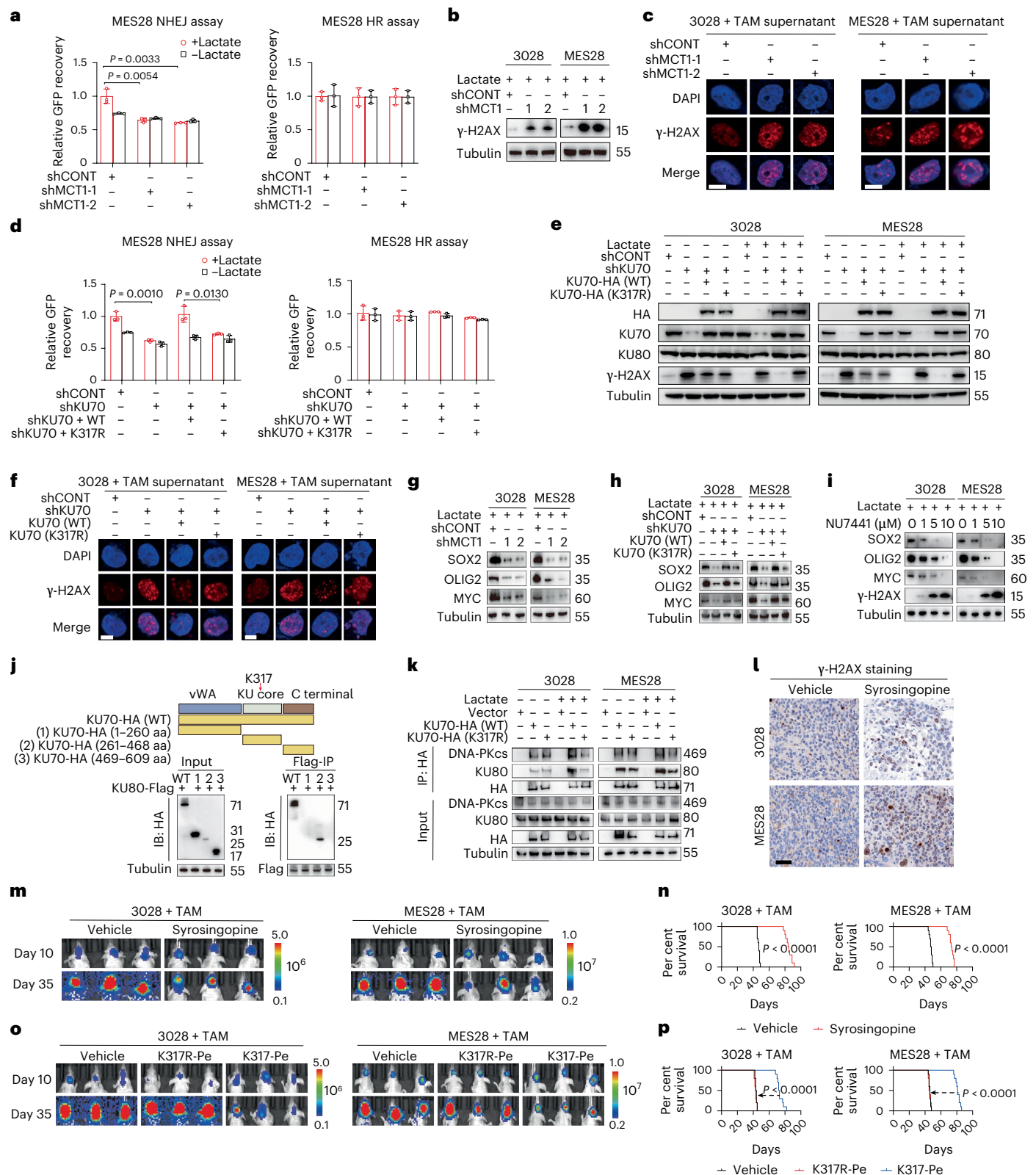
### Fig. 4 | Lactylation of KU70 K317 enhances the NHEJ function and maintains the stemness of GSC. a, A diagram of the NHEJ and HR reporter assay. Effects of MCT1 knockdown on the efficiency of NHEJ and HR in MES28 GSC with or without the stimulation of lactate ( $n = 3$ ). b, Immunoblot (IB) analysis of $\gamma$ -H2AX level after MCT1 knockdown in 3028 (left) and MES28 (right) GSCs by stimulating with lactate. c, Immunofluorescence staining of $\gamma$ -H2AX after MCT1 knockdown in 3028 (left) and MES28 (right) GSCs by stimulating with the supernatant of TAMs. Scale bar, 10 $\mu$ m. d, Effects of KU70 knockdown and rescued by overexpression of KU70 WT or KU70 K317R on the efficiency of NHEJ and HR in MES28 GSC with or without the stimulation of lactate ( $n = 3$ ). e, IB analysis of GSCs KU80 and $\gamma$ -H2AX level with or without the stimulation of 10 mM lactate combined transduced with shCONT and shKU70 and rescued by KU70 WT or KU70 K317R after KU70 knockdown. f, Immunofluorescence staining of $\gamma$ -H2AX under the stimulation of supernatant of TAMs combined transduced with shCONT and shKU70 and rescued by overexpression of KU70 WT or KU70 K317R after KU70 knockdown in 3028 and MES28 GSCs. Scale bar, 10 $\mu$ m. g, IB results show that the knockdown of MCT1 in 3028 and MES28 GSCs under the stimulation of 10 mM lactate decreased the protein levels of stemness markers SOX2, OLIG2 and MYC. h, IB showing GSCs transduced with shCONT and shKU70 and rescued by overexpression of KU70 WT or KU70 K317R after KU70 knockdown combined with lactate stimulation decreased the protein levels of stemness markers SOX2, OLIG2 and MYC. i, IB results show the protein levels of stemness markers (SOX2, OLIG2 and MYC) and $\gamma$ -H2AX of 3028 and MES28 GSCs bearing different concentrations of NU7441

combined with lactate. j, Top: fragments of KU70. Bottom: western blot of immunoprecipitation with anti-Flag antibody in MES28 GSC expressing Flag-tagged of full-length KU80 and HA-tagged of KU70 deletion mutant from the top panel under the stimulation of lactate. k, IB results showing the interaction between KU70 WT or KU70 K317R and KU80 or DNA-PKcs with anti-HA antibody in 3028 and MES28 GSCs with or without the 10 mM lactate stimulated. l, Representative images showing immunohistochemically stained with  $\gamma$ -H2AX in as indicated brain sections of the indicated mice on day 25 after injection of GSCs. Scale bar, 50  $\mu$ m. m, In vivo bioluminescence imaging of tumour growth was performed in nude mice bearing GBM xenografts derived from  $5 \times 10^4$  TAMs and  $5 \times 10^4$  luciferase-expressing GSCs (3028 and MES28) on days 10 and 35, showing the effect of treatment of 10 mg kg<sup>-1</sup> syringopine every 2 days on tumour growth. n, Kaplan–Meier survival curves of immunodeficiency mice with TAMs and intracranial 3028 or MES28 GSCs after treatment of syringopine ( $n = 10$ ). o, In vivo bioluminescence imaging of tumour growth was performed in nude mice bearing GBM xenografts derived from  $5 \times 10^4$  TAMs and  $5 \times 10^4$  luciferase-expressing GSCs (3028 and MES28) on days 10 and 35, showing the effect of treatment of 5 mg kg<sup>-1</sup> KU70 K317-Peptide or KU70 K317R-Peptide every 2 days on tumour growth. p, Kaplan–Meier survival curves of immunodeficiency mice with TAMs and intracranial 3028 or MES28 GSCs after treatment of KU70 K317-Peptide or KU70 K317R-Peptide ( $n = 10$ ). The data are presented as the mean  $\pm$  s.d. The statistical significance was determined by a two-tailed Student's *t*-test for a and d or two-tailed log-rank test for n and p.

combined with lactate. j, Top: fragments of KU70. Bottom: western blot of immunoprecipitation with anti-Flag antibody in MES28 GSC expressing Flag-tagged of full-length KU80 and HA-tagged of KU70 deletion mutant from the top panel under the stimulation of lactate. k, IB results showing the interaction between KU70 WT or KU70 K317R and KU80 or DNA-PKcs with anti-HA antibody in 3028 and MES28 GSCs with or without the 10 mM lactate stimulated. l, Representative images showing immunohistochemically stained with  $\gamma$ -H2AX in as indicated brain sections of the indicated mice on day 25 after injection of GSCs. Scale bar, 50  $\mu$ m. m, In vivo bioluminescence imaging of tumour growth was performed in nude mice bearing GBM xenografts derived from  $5 \times 10^4$  TAMs and  $5 \times 10^4$  luciferase-expressing GSCs (3028 and MES28) on days 10 and 35, showing the effect of treatment of 10 mg kg<sup>-1</sup> syringopine every 2 days on tumour growth. n, Kaplan–Meier survival curves of immunodeficiency mice with TAMs and intracranial 3028 or MES28 GSCs after treatment of syringopine ( $n = 10$ ). o, In vivo bioluminescence imaging of tumour growth was performed in nude mice bearing GBM xenografts derived from  $5 \times 10^4$  TAMs and  $5 \times 10^4$  luciferase-expressing GSCs (3028 and MES28) on days 10 and 35, showing the effect of treatment of 5 mg kg<sup>-1</sup> KU70 K317-Peptide or KU70 K317R-Peptide every 2 days on tumour growth. p, Kaplan–Meier survival curves of immunodeficiency mice with TAMs and intracranial 3028 or MES28 GSCs after treatment of KU70 K317-Peptide or KU70 K317R-Peptide ( $n = 10$ ). The data are presented as the mean  $\pm$  s.d. The statistical significance was determined by a two-tailed Student's *t*-test for a and d or two-tailed log-rank test for n and p.

(469–609 aa) (Fig. 4j, top). Flag-tagged full-length KU80 and each HA-tagged KU70 deletion mutant were co-expressed in MES28 GSC, followed by immunoprecipitation with an anti-Flag antibody. Only the Ku core region (261–468 aa) was co-immunoprecipitated with the KU80 domain, indicating that this region that includes the K317 lactylation site, is key for this interaction (Fig. 4j, bottom). Under lactate stimulation, KU70 K317R overexpression decreased the combination

levels of KU80 and DNA-dependent protein kinase catalytic subunit (DNA-PKcs) compared with KU70 WT overexpression, whereas without lactate KU70 WT and KU70 K317R bound DNA-PKcs and KU80 equally (Fig. 4k and Extended Data Fig. 7f). Upon overexpression of the P300 catalytic domain, the increased KU70 lactylation was accompanied by an enhanced binding to KU80 (Extended Data Fig. 7g). The structure of the KU70–KU80 heterodimer shows that K317 could form a salt bridge



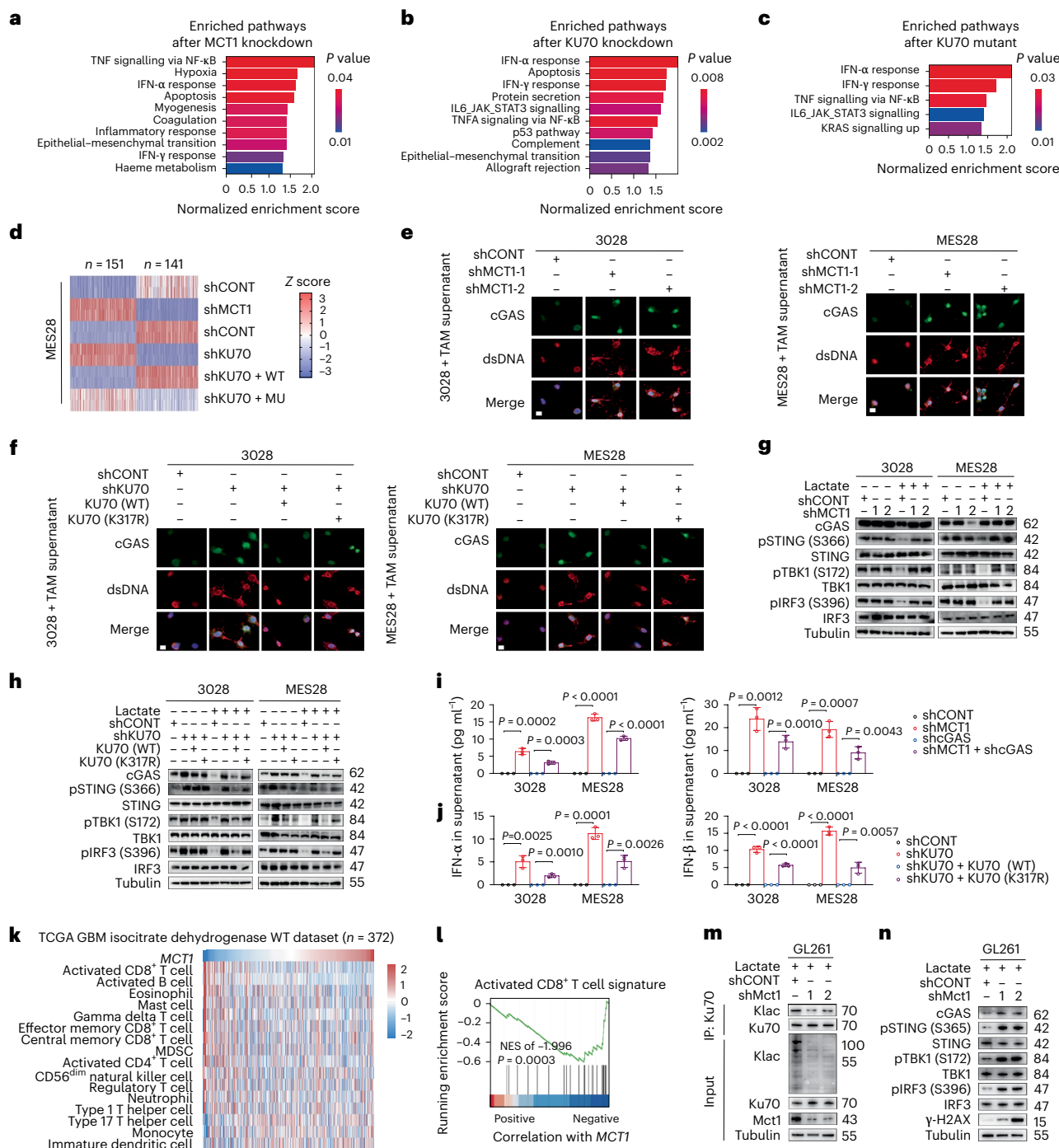


**Fig. 5 | Lactylation of KU70 K317 inhibits cGAS–STING signalling and maintains the immunosuppressive TME. a**, Top ten of Hallmark signalling pathway enrichment analysis after MCT1 knockdown in MES28 GSC. **b**, Hallmark pathway enrichment analysis after KU70 knockdown in MES28 GSC. **c**, Enriched pathways in rescued KU70 with KU70 K317R than KU70 WT after KU70 knockdown in MES28 GSC. **d**, A summary of upregulated and downregulated genes in MCT1 knockdown, KU70 knockdown and rescued KU70 with KU70 WT and KU70 K317R after KU70 knockdown in MES28 GSC. **e**, Immunofluorescence staining of cGAS (green) and dsDNA (red) after MCT1 knockdown in 3028 (left) and MES28 (right) GSCs while treating with supernatant of TAMs. Scale bar, 30  $\mu$ m. **f**, Immunofluorescence staining of cGAS (green) and dsDNA (red) of GSCs while treating with supernatant of TAMs combined transduced with shCONT and shKU70 and rescued by overexpression of KU70 WT or KU70 K317R after KU70 knockdown. Scale bar, 30  $\mu$ m. **g**, Immunoblot analysis of the cGAS–STING signalling pathway after MCT1 knockdown in 3028 (left) and MES28 (right) GSCs with or without the stimulation of 10 mM lactate. **h**, Immunoblot analysis of

the cGAS–STING signalling pathway with or without the stimulation of lactate combined transduced with shCONT, shKU70 or shKU70 rescued with KU70 WT or KU70 K317R. **i**, ELISA experiments detecting the levels of type I interferon (IFN- $\alpha$  and IFN- $\beta$ ) while 3028 and MES28 GSCs expressing shMCT1 and shcGAS or combination of shMCT1 and shcGAS ( $n = 3$ ). **j**, ELISA results showed type I interferon levels of GSCs transduced with shCONT and shKU70 and rescued by overexpression of KU70 WT or KU70 K317R after KU70 knockdown ( $n = 3$ ). **k**, The single-sample GSEA for correlation of MCT1 expression level with corresponding immune cell lineages in the TCGA GBM (IDH WT) dataset. **l**, GSEA scores calculated for the TCGA GBM dataset show that MCT1 negatively correlates with activated CD8 $^{+}$  T cell signature. **m**, Immunoblot analysis showing the pan-lactylation level and the lactylation level of Ku70 in GL261 after Mct1 knockdown. **n**, Immunoblot analysis of the cGAS–STING signalling pathway after Mct1 knockdown in GL261. The data are presented as the mean  $\pm$  s.d. The statistical significance was determined by a two-tailed Student's *t*-test for **i** and **j**. IP, immunoprecipitation; MU, mutant; NES, normalized enrichment score.

with glutamate 330 (E330)<sup>34</sup>. We introduced the E330A mutation by replacing E330 with alanine. After KU70 knockdown under lactate stimulation, KU70 E330A overexpression exhibited no substantial difference in KU70–KU80 heterodimer formation or  $\gamma$ -H2AX levels compared with the KU70 WT (Extended Data Fig. 7h). NHEJ assay confirmed that the KU70 E330A mutation did not affect NHEJ function (Extended Data Fig. 7i).

Furthermore, inhibition of lactate transporters MCT1 and MCT4 with syrosingopine in animal models revealed that lactate transport in the TME facilitates tumourigenesis. Syrosingopine enhanced  $\gamma$ -H2AX staining in xenograft tumour models, suggesting that lactate transport positively correlates with NHEJ function and that targeting MCT1–MCT4 enhanced DNA damage and extends mice survival in vivo (Fig. 4l–n). We then designed a cell-penetrating peptide (CPP) to target lactylation of KU70 K317. We synthesized K317-Peptide (termed as K317-Pe) and a peptide variant, designated as K317R-peptide (termed as K317R-Pe). KU70 K317-peptide markedly reduced KU70 lactylation, impairing DSB repair and raising  $\gamma$ -H2AX levels (Extended Data Fig. 7j). The treatment of KU70 K317-Peptide in vivo effectively prolonged survival and reduced tumour volume (Fig. 4o,p). Collectively, these data suggested that GSCs import TAM-derived lactate to induce KU70 K317 lactylation, which maintains the stemness and proliferation through enhancing NHEJ function.

### Lactylation of KU70 K317 inhibits cGAS–STING signalling and maintains the immunosuppressive TME

To elucidate how MCT1-mediated lactate import induces KU70 K317 lactylation in GSCs, we performed RNA-seq in MES28 GSC. GSEA revealed an enrichment of the interferon  $\alpha$  (IFN- $\alpha$ ) response pathway following depletion of KU70 K317 lactylation via MCT1, KU70 deletion or KU70 K317 mutation (Fig. 5a–c). RNA-seq revealed that the expression of 292 genes was induced upon the loss of MCT1, KU70 or the lactylation of KU70 K317, uncovering analogously regulated downstream pathways (Fig. 5d). Gene Ontology analysis revealed that IFN- $\alpha$ /interferon beta (IFN- $\beta$ ) production signatures positively correlate with *MCT1* expression (Extended Data Fig. 8a), as well as with those of *KU70* expression and KU70 K317 lactylation (Extended Data Fig. 8b,c). GSEA of the TCGA GBM dataset verified that *MCT1* and *KU70* expression correlate with immune response (Extended Data Fig. 8d,e). Considering the NHEJ reduction may cause chromosomal instability and double-strand DNA release, we identified the double-strand DNA released into cytoplasm after silencing of MCT1 or KU70 by immunofluorescence. Similar result was observed upon KU70 K317R overexpression after silencing KU70 in GSCs stimulated with TAM supernatant (Fig. 5e,f). Immunoblotting showed that exogenous lactate activated cGAS–STING signalling in MCT1 or KU70 knockdown GSCs, but this activation was suppressed by KU70 K317 lactylation (Fig. 5g,h).

Enzyme-linked immunosorbent assay (ELISA) experiments verified that MCT1 knockdown increased IFN- $\alpha$ /IFN- $\beta$  levels in GSCs supernatant, which was rescued by cGAS silencing or KU70 K317R overexpression (Fig. 5i,j). The reduction in stemness caused by MCT1 knockdown was not rescued by decreasing cGAS expression, indicating that MCT1 regulates GSC stemness independently of cGAS signalling (Extended Data Fig. 8f).

To identify the immune compartment affected by lactate-absorbing GSCs, we analysed the TCGA GBM dataset, single-sample GSEA revealed that *MCT1* was negatively correlated with CD8<sup>+</sup> T cell signature (Fig. 5k,l). Furthermore, we used mouse glioma cell line GL261 to validate the similar mechanism of lactate-induced murine Ku70 lactylation and enhanced NHEJ. NHEJ instead of HR function was reduced after silencing murine Mct1 in GL261 with stimulation of lactate (Extended Data Fig. 8g). Mct1 knockdown in GL261 cells restricted lactate uptake, reducing Ku70 lactylation without affecting Ku70 protein level (Fig. 5m), also leading to increased  $\gamma$ -H2AX, cGAS–STING activation and elevated IFNs secretion (Fig. 5n and Extended Data Fig. 8h).

Moreover, we detected MC9 GSC stemness and profiled the immune landscape of *Slc16a3*-conditional-knockout mice with flow cytometry, to quantify GSC and major immune compartments. We observed that *Slc16a3*-conditional-knockout mice showed decreased GSC Prom1 and Sox2 expression (Extended Data Fig. 8i,j). Compared with controls, CD8<sup>+</sup> T cell frequency was markedly elevated, whereas macrophage numbers declined, a reduction attributable to *Slc16a3* deletion-dependent lactate accumulation. Other immune populations displayed largely unchanged (Extended Data Fig. 9a and Supplementary Fig. 2a–i). We therefore focused on the CD8<sup>+</sup> T cell. Mice bearing MC9 GSC co-implanted with bone marrow-derived macrophages (BMDMs) that were treated with KU70 K317-Pe exhibited prolonged survival and reduced tumour volume than those treated with K317R-Peptide (Extended Data Fig. 9b–e), an outcome associated with elevated levels of CD8<sup>+</sup> T cells activation and exhaustion (Extended Data Fig. 9f,g). Treatment with syrosingopine increased PD-1 (encoded by *PDCD1*) expression on CD8<sup>+</sup> T cells (Extended Data Fig. 9h). Integrating the expression of lactate transport signature with *PD-1* showed an association with poor prognosis in GBM datasets (Extended Data Fig. 9i). To detect the T cell-mediated functional cytotoxicity, we cocultured GSCs with human peripheral blood mononuclear cell (PBMC)-induced macrophages, treated with syrosingopine, and found that PBMC-derived CD8<sup>+</sup> T cells exhibited cytotoxic activity when combined with anti-PD-1 antibody treatment (Extended Data Fig. 9j). The IFN- $\gamma$  level was detected and observed that the cytotoxicity of CD8<sup>+</sup> T cells was upregulated after the treatments (Extended Data Fig. 9k). Collectively, TAM-derived lactate induced KU70 K317 lactylation and reduced cytotoxic CD8<sup>+</sup> T cells function.

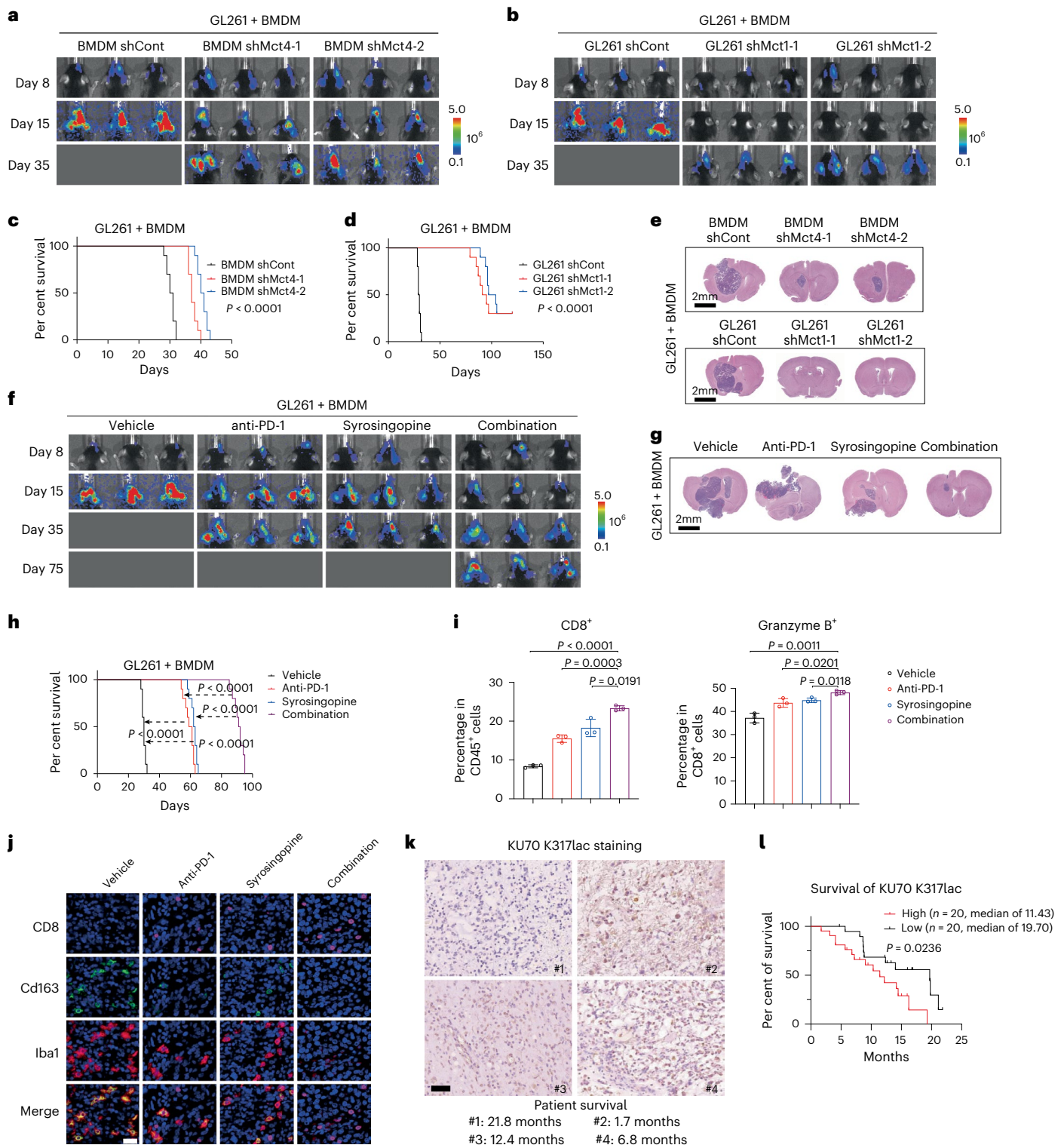
**Fig. 6 | Therapeutic efficacy of lactate transporter inhibitor combined with PD-1 antibody in GBM. a**, In vivo bioluminescence imaging of tumour growth was performed in C57BL/6j mice bearing  $5 \times 10^4$  mouse glioma cell line GL261 and  $5 \times 10^4$  BMDMs transduced with shCont, shMct4-1 or shMct4-2 on days 8, 15 and 35. The control groups (mice bearing GL261 and BMDMs transduced with shCont) on day 35 were dead. **b**, In vivo bioluminescence imaging of tumour growth was performed in C57BL/6j mice bearing  $5 \times 10^4$  BMDMs and  $5 \times 10^4$  GL261 transduced with shCont, shMct1-1 or shMct1-2 on days 8, 15 and 35. The control groups (mice bearing BMDMs and GL261 transduced with shCont) on day 35 were dead. **c**, Kaplan–Meier survival curves of immunocompetent mice bearing GL261 and BMDMs transduced with shCont, shMct4-1 or shMct4-2 derived intracranial tumours ( $n = 10$ ). **d**, Kaplan–Meier survival curves of immunocompetent mice bearing BMDMs and GL261 after knockdown of Mct1 derived intracranial tumours ( $n = 10$ ). **e**, Representative images of haematoxylin and eosin staining of mouse brains collected on day 25 after transplantation of GL261 and BMDMs separated knockdown of Mct1 and Mct4. Scale bar, 2 mm. Each image is representative of at least three similar experiments. **f**, In vivo bioluminescence imaging of tumour growth was performed in immunocompetent mice bearing

GL261 and BMDMs using combination of the Mct1–Mct4 inhibitor and PD-1 antibody. **g**, Representative images of haematoxylin and eosin staining of mouse brains collected on day 25 after transplantation of GL261 and BMDMs treated with Mct1–Mct4 inhibitor and PD-1 antibody. Scale bar, 2 mm. Each image is representative of at least three similar experiments. **h**, Kaplan–Meier survival curves of immunocompetent mice after being treated with Mct1/4 inhibitor and PD-1 antibody ( $n = 10$ ). **i**, Flow cytometry analysis of treated CD8<sup>+</sup> T cells and granzyme B<sup>+</sup> CD8<sup>+</sup> T cells ( $n = 3$  biologically independent mice) in BMDMs and GL261-derived tumours at day 25 after injection. **j**, Immunofluorescence staining shows the pan-macrophage marker Iba-1 (green), tumour-promoting macrophage marker Cd163 (red) and CD8 (magenta) from GL261-derived tumours. Scale bar, 50  $\mu$ m. **k**, Representative images showing human samples immunohistochemically stained with the antibody against KU70 K317lac. Scale bar, 50  $\mu$ m. **l**, Kaplan–Meier plots of the overall survival rates in specimens by high and low expression of KU70 K317lac. The experiments were performed three times independently for **j** and **k**. The data are presented as the mean  $\pm$  s.d. The statistical significance was determined by a two-tailed log-rank test for **c**, **d**, **h** and **l** or two-tailed Student's *t*-test for **i**.

## Inhibition of lactate transporters synergizes with immune checkpoint inhibitor to prolong survival in GBM models

To interrogate the therapeutic potential of TAM-GSC metabolic crosstalk and immunomodulation, we designed a preclinical study with cotransplantation in an immunocompetent orthotopic xenograft model. Knockdown of Mct4 in BMDMs or knockdown of Mct1 in GL261 prolonged tumour latency and reduced tumour volume (Fig. 6a–e). To evaluate potential combinatorial therapeutic efficacy *in vivo*, meanwhile, to prevent CD8<sup>+</sup> T cells exhaustion caused by sustained tumouricidal activity, mice cotransplanted with GL261 and BMDMs were treated with one of

four approaches: vehicle control, anti-PD-1, syrosingopine or the combination of anti-PD-1 and syrosingopine. Tumour volume was assessed, revealing a minimal decrease in tumour volume in the anti-PD-1 group, a moderate reduction in the syrosingopine group and a more pronounced decrease in the combination group (Fig. 6f–h). Combined blockade of lactate transporters and PD-1 inhibition improved survival and reduced tumour volume compared with either monotherapy or vehicle control. Enhanced CD8<sup>+</sup> T cells infiltration and activity were observed after the combined treatment of anti-PD-1 antibody and syrosingopine, which was similar to the increased T cells data in mice bearing Mct1-depleted



GL261 cells with BMDMs (Fig. 6i and Extended Data Fig. 10a). The combined treatment of syrosingopine and anti-PD-1 antibody showed the enhanced infiltration of CD8<sup>+</sup> T cells and the lower abundance of TAMs, as measured by Cd163, and pan-macrophage marker Iba-1 (Fig. 6j). Lactate transport inhibition via MCT4 loss in TAMs or Mct4 loss in BMDMs increased TAM apoptosis and decreased immunosuppressive markers expression (Extended Data Fig. 10b). We found that Ku70 inhibition combined with cgas suppressed tumour progression that was exacerbated by cgas loss (Extended Data Fig. 10c–f). The synergistic administration of anti-PD-1 and KU70 K317-Pe reduced tumour volume and improved overall survival compared with monotherapy or the vehicle control group in intracranial xenograft models (Extended Data Fig. 10g–i). Furthermore, we analysed human GBM samples with immunohistochemistry staining using anti-KU70 K317 lactylation antibody (Fig. 6k). The strong lactylation level of KU70 K317 correlated with the decreased overall survival (Fig. 6l). Collectively, targeting MCT1–MCT4 or KU70 K317 lactylation synergizes with anti-PD-1 antibody to generate an additive antitumour effect.

## Discussion

The establishment of an immunosuppressive environment is closely related to metabolites generated within the TME<sup>37,38</sup>. Although tumour cells were long considered the primary lactate source, it is now evident that immune and stromal populations also engage in Warburg metabolism and contribute to lactate accumulation and protein lactylation in the tumour milieu<sup>39,40</sup>. However, how lactate specifically induces proteins lactylation in GSC remains unknown. In this study, we revealed that TAM-derived lactate drives GSC proliferation and KU70 lactylation, suppressing cGAS–type I IFN signalling and fostering an immunosuppressive TME via CD8<sup>+</sup> T cells dysfunction. Pharmacological blockade of MCT1 and MCT4 or targeting KU70 K317 lactylation, combined with anti-PD-1 therapy, showed potent efficacy against GSC and TME, offering strategies for GBM treatment (Extended Data Fig. 10j,k).

Transmembrane lactate transporters encoded by the SLC16 family, including the widely expressed MCT1 and MCT4, facilitate proton-coupled, bidirectional monocarboxylate transport<sup>41</sup>. Their synergy shuttles lactate between glycolytic and oxidative cells, preserving tissue lactate homeostasis<sup>42–44</sup>. Existing studies of lactate transport have focused on tumour-derived lactate promoting GBM proliferation, migration and tumourigenesis<sup>45</sup>. TME-derived lactate and its function on immunosuppressive TME remain unclear. Interestingly, we found that lactate transport signatures were enriched in TAMs and tumour cells, further experiments indicated that GSCs can take up lactate from TAMs via MCT1–MCT4. Using *Slc16a3*<sup>fl/fl</sup>/*Ly2z*<sup>Cre</sup> genotype mouse model, we showed that myeloid-specific deletion of *Slc16a3* markedly reduced lactate concentration in tumour cells. These results corroborated our hypothesis that TAMs-derived lactate is transported to tumour cells, facilitating GBM progression.

Accumulating evidence links cancer cell glucose metabolism and lactate production to alterations in DNA repair mechanisms that correlate with antitumoural treatment failure<sup>46,47</sup>. NHEJ, a DNA repair pathway frequently dysregulated in cancer, represents a key target for synthetic lethality. Unlike HR, it directly ligates DNA breaks without a homologous template, making it faster but error prone<sup>47</sup>. The KU70–KU80 heterodimer and DNA-PKcs complex form its core machinery<sup>48,49</sup>. Our finding uncovered that TAM-derived lactate via MCT1/4, induced KU70 K317 lactylation that maintains GSC proliferation and stemness through facilitating KU70–KU80–DNA-PKcs complex formation. Pharmacological inhibition of the NHEJ pathway with DNA-PKcs inhibitor NU7441 reduced GSC viability and stemness. Blockage of MCT1–MCT4 with syrosingopine resulted in persistent DNA damage and improper repair. We designed KU70 K317 lactylation targeting CPP, which reduced tumour volume and extended survival in vivo. Silencing MCT1 or KU70 induced cytosolic DNA accumulation, which activated cGAS–IFN signalling to trigger antitumour immunity via cytotoxic CD8<sup>+</sup> T cells.

Given its pivotal role in tumourigenesis and immune regulation, lactate metabolism represents a promising target to improve cancer immunotherapy. Early attempts to inhibit the lactate production focused on targeting of glycolysis via the PI3K-AKT-mTOR-HIF axis<sup>50</sup>. The combination of the LDH inhibitor oxamate and anti-PD-1 blockade enhances CD8<sup>+</sup> T cells infiltration and suppresses tumour growth<sup>51</sup>. Inhibiting lactate secretion and proton export via MCT1–4 by diclofenac<sup>52,53</sup> or MCT inhibitors<sup>54</sup> reduced myeloid-derived suppressor cells, whereas increasing CD8<sup>+</sup> T cells infiltration in the TME. Our study demonstrates that combinatorial treatment with anti-PD-1 and syrosingopine, an MCT1 and MCT4 inhibitor, distinctly blocked tumourigenesis and enhanced immunotherapy.

Collectively, we unveil that TAM-derived lactate, transported via MCT1–MCT4, promotes GSC growth and stemness by inducing NHEJ protein KU70 lactylation, which remodels the TME via type I IFN signalling. Therefore, targeting lactate transport-induced lactylation and activation of the NHEJ pathway represent promising strategies to enhance the tumour immunotherapies.

## Online content

Any methods, additional references, Nature Portfolio reporting summaries, source data, extended data, supplementary information, acknowledgements, peer review information; details of author contributions and competing interests; and statements of data and code availability are available at <https://doi.org/10.1038/s41556-025-01839-y>.

## References

- Louis, D. N., Perry, A. & Wesseling, P. The 2021 WHO classification of tumors of the central nervous system: a summary. *Neuro. Oncol.* **23**, 1231–1251 (2021).
- Miller, K. D. et al. Brain and other central nervous system tumor statistics, 2021. *CA Cancer J. Clin.* **71**, 381–406 (2021).
- Ye, Z. et al. Targeting microglial metabolic rewiring synergizes with immune-checkpoint blockade therapy for glioblastoma. *Cancer Discov.* **13**, 974–1001 (2023).
- Ostrom, Q. T. et al. CBTRUS Statistical Report: primary brain and other central nervous system tumors diagnosed in the United States in 2015–2019. *Neuro. Oncol.* **24**, v1–v95 (2022).
- Tan, A. C., Ashley, D. M. & Lopez, G. Y. Management of glioblastoma: state of the art and future directions. *CA Cancer J. Clin.* **70**, 299–312 (2020).
- Lathia, J. D., Mack, S. C., Mulkearns-Hubert, E. E., Valentim, C. L. & Rich, J. N. Cancer stem cells in glioblastoma. *Genes Dev.* **29**, 1203–1217 (2015).
- Prager, B. C., Xie, Q., Bao, S. & Rich, J. N. Cancer stem cells: the architects of the tumor ecosystem. *Cell Stem Cell* **24**, 41–53 (2019).
- Lan, X. et al. Fate mapping of human glioblastoma reveals an invariant stem cell hierarchy. *Nature* **549**, 227–232 (2017).
- Berg, T. J. & Marques, C. The irradiated brain microenvironment supports glioma stemness and survival via astrocyte-derived transglutaminase 2. *Cancer Res.* **81**, 2101–2115 (2021).
- Dapash, M., Hou, D., Castro, B., Lee-Chang, C. & Lesniak, M. S. The interplay between glioblastoma and its microenvironment. *Cells* **10**, 2257 (2021).
- Hernandez, A. & Domenech, M. Glioblastoma: relationship between metabolism and immunosuppressive microenvironment. *Cells* **10**, 3529 (2021).
- Flint, T. R., Fearon, D. T. & Janowitz, T. Connecting the metabolic and immune responses to cancer. *Trends Mol. Med.* **23**, 451–464 (2017).
- Vilbois, S., Xu, Y. & Ho, P. C. Metabolic interplay: tumor macrophages and regulatory T cells. *Trends Cancer* **10**, 242–255 (2024).
- Xia, L. et al. The cancer metabolic reprogramming and immune response. *Mol. Cancer* **20**, 28 (2021).

15. Khan, F. et al. Macrophages and microglia in glioblastoma: heterogeneity, plasticity, and therapy. *J. Clin. Invest.* **133**, e163446 (2023).
16. Xuan, W., Lesniak, M. S., James, C. D., Heimberger, A. B. & Chen, P. Context-dependent glioblastoma-macrophage/microglia symbiosis and associated mechanisms. *Trends Immunol.* **42**, 280–292 (2021).
17. Certo, M., Tsai, C. H., Pucino, V., Ho, P. C. & Mauro, C. Lactate modulation of immune responses in inflammatory versus tumour microenvironments. *Nat. Rev. Immunol.* **21**, 151–161 (2021).
18. Vander Heiden, M. G., Cantley, L. C. & Thompson, C. B. Understanding the Warburg effect: the metabolic requirements of cell proliferation. *Science* **324**, 1029–1033 (2009).
19. Zhang, D. et al. Metabolic regulation of gene expression by histone lactylation. *Nature* **574**, 575–580 (2019).
20. Li, X. et al. Lactate metabolism in human health and disease. *Signal Transduct. Target Ther.* **7**, 305 (2022).
21. Fan, M. & Yang, K. Lactate promotes endothelial-to-mesenchymal transition via Snail1 lactylation after myocardial infarction. *Sci. Adv.* **9**, eadc9465 (2023).
22. Li, Z. et al. Lactate shuttling links histone lactylation to adult hippocampal neurogenesis in mice. *Dev. Cell* **60**, 1182–1198.e1188 (2025).
23. Qian, Y. et al. MCT4-dependent lactate secretion suppresses antitumor immunity in LKB1-deficient lung adenocarcinoma. *Cancer Cell* **41**, 1363–1380.e1367 (2023).
24. Colegio, O. R. et al. Functional polarization of tumour-associated macrophages by tumour-derived lactic acid. *Nature* **513**, 559–563 (2014).
25. Abad, E., Graifer, D. & Lyakhovich, A. DNA damage response and resistance of cancer stem cells. *Cancer Lett.* **474**, 106–117 (2020).
26. Bao, S. et al. Glioma stem cells promote radioresistance by preferential activation of the DNA damage response. *Nature* **444**, 756–760 (2006).
27. Aleksandrov, R., Hristova, R., Stoyanov, S. & Gospodinov, A. The chromatin response to double-strand DNA breaks and their repair. *Cells* **9**, 1853 (2020).
28. Callen, E. et al. 53BP1 mediates productive and mutagenic DNA repair through distinct phosphoprotein interactions. *Cell* **153**, 1266–1280 (2013).
29. Xu, G. et al. REV7 counteracts DNA double-strand break resection and affects PARP inhibition. *Nature* **521**, 541–544 (2015).
30. Chen, Y. et al. Metabolic regulation of homologous recombination repair by MRE11 lactylation. *Cell* **187**, 294–311.e221 (2024).
31. Chen, H. et al. NBS1 lactylation is required for efficient DNA repair and chemotherapy resistance. *Nature* **631**, 663–669 (2024).
32. Liu, X. et al. Activation of GPR81 by lactate drives tumour-induced cachexia. *Nat. Metab.* **6**, 708–723 (2024).
33. Mack, S. C. et al. Chromatin landscapes reveal developmentally encoded transcriptional states that define human glioblastoma. *J. Exp. Med.* **216**, 1071–1090 (2019).
34. Al Emam, A., Arbon, D., Jeeves, M. & Kysela, B. Ku70 N-terminal lysines acetylation/deacetylation is required for radiation-induced DNA-double strand breaks repair. *Neoplasia* **65**, 708–719 (2018).
35. Tubbs, A. & Nussenzweig, A. Endogenous DNA damage as a source of genomic instability in cancer. *Cell* **168**, 644–656 (2017).
36. Tang, M. & Chen, G. SMYD2 inhibition-mediated hypomethylation of Ku70 contributes to impaired nonhomologous end joining repair and antitumor immunity. *Sci. Adv.* **9**, eade6624 (2023).
37. Li, Z., Sun, C. & Qin, Z. Metabolic reprogramming of cancer-associated fibroblasts and its effect on cancer cell reprogramming. *Theranostics* **11**, 8322–8336 (2021).
38. Wang, H., Franco, F. & Ho, P. C. Metabolic regulation of T<sub>reg</sub> in cancer: opportunities for immunotherapy. *Trends Cancer* **3**, 583–592 (2017).
39. Heuser, C., Renner, K., Kreutz, M. & Gattinoni, L. Targeting lactate metabolism for cancer immunotherapy—a matter of precision. *Semin Cancer Biol.* **88**, 32–45 (2023).
40. Reinfeld, B. I. & Madden, M. Z. Cell-programmed nutrient partitioning in the tumour microenvironment. *Nature* **593**, 282–288 (2021).
41. Felmlee, M. A., Jones, R. S., Rodriguez-Cruz, V., Follman, K. E. & Morris, M. E. Monocarboxylate transporters (SLC16): function, regulation, and role in health and disease. *Pharm. Rev.* **72**, 466–485 (2020).
42. Park, S. J. et al. An overview of MCT1 and MCT4 in GBM: small molecule transporters with large implications. *Am. J. Cancer Res.* **8**, 1967–1976 (2018).
43. Floch, R. L. et al. CD147 subunit of lactate/H<sup>+</sup> symporters MCT1 and hypoxia-inducible MCT4 is critical for energetics and growth of glycolytic tumors. *Proc. Natl Acad. Sci. USA* **108**, 16663–16668 (2011).
44. Sattler, B. & Kranz, M. Preclinical incorporation dosimetry of [<sup>18</sup>F] FACH-a novel <sup>18</sup>F-labeled MCT1/MCT4 lactate transporter inhibitor for imaging cancer metabolism with PET. *Molecules* **25**, 2024 (2020).
45. Li, G. et al. Glycometabolic reprogramming-induced XRCC1 lactylation confers therapeutic resistance in ALDH1A3-overexpressing glioblastoma. *Cell Metab.* **36**, 1696–1710.e1610 (2024).
46. Quinet, A., Tirman, S., Cybulla, E., Meroni, A. & Vindigni, A. To skip or not to skip: choosing repriming to tolerate DNA damage. *Mol. Cell* **81**, 649–658 (2021).
47. Weinstock, D. M., Richardson, C. A., Elliott, B. & Jasin, M. Modeling oncogenic translocations: distinct roles for double-strand break repair pathways in translocation formation in mammalian cells. *DNA Repair (Amst.)* **5**, 1065–1074 (2006).
48. Zhao, B., Rothenberg, E. & Ramsden, D. A. The molecular basis and disease relevance of non-homologous DNA end joining. *Nat. Rev. Mol. Cell Biol.* **21**, 765–781 (2020).
49. Woodbine, L., Gennery, A. R. & Jeggo, P. A. The clinical impact of deficiency in DNA non-homologous end-joining. *DNA Repair (Amst.)* **16**, 84–96 (2014).
50. Kaneda, M. M. et al. PI3Kgamma is a molecular switch that controls immune suppression. *Nature* **539**, 437–442 (2016).
51. Qiao, T. et al. Inhibition of LDH-A by oxamate enhances the efficacy of anti-PD-1 treatment in an NSCLC humanized mouse model. *Front Oncol.* **11**, 632364 (2021).
52. Renner, K. et al. Restricting glycolysis preserves T cell effector functions and augments checkpoint therapy. *Cell Rep.* **29**, 135–150.e139 (2019).
53. Vander Linden, C. et al. Therapy-induced DNA methylation inactivates MCT1 and renders tumor cells vulnerable to MCT4 inhibition. *Cell Rep.* **35**, 109202 (2021).
54. Belouche-Babari, M. & Casals Galobart, T. Monocarboxylate transporter 1 blockade with AZD3965 inhibits lipid biosynthesis and increases tumour immune cell infiltration. *Br. J. Cancer* **122**, 895–903 (2020).

**Publisher's note** Springer Nature remains neutral with regard to jurisdictional claims in published maps and institutional affiliations.

Springer Nature or its licensor (e.g. a society or other partner) holds exclusive rights to this article under a publishing agreement with the author(s) or other rightsholder(s); author self-archiving of the accepted manuscript version of this article is solely governed by the terms of such publishing agreement and applicable law.

© The Author(s), under exclusive licence to Springer Nature Limited 2026

<sup>1</sup>National Health Commission Key Laboratory of Antibody Techniques, Department of Cell Biology, Jiangsu Provincial Key Laboratory of Human Functional Genomics, School of Basic Medical Sciences, Nanjing Medical University, Nanjing, China. <sup>2</sup>Institute for Brain Tumours, Jiangsu Key Lab of Cancer Biomarkers, Prevention and Treatment, Collaborative Innovation Center for Cancer Personalized Medicine, Nanjing Medical University, Nanjing, China. <sup>3</sup>Lineberger Comprehensive Cancer Center, University of North Carolina, Chapel Hill, NC, USA. <sup>4</sup>Department of Radiation Oncology, Holden Comprehensive Cancer Center, Iowa Neuroscience Institute, University of Iowa, Iowa City, IA, USA. <sup>5</sup>Department of Neurosurgery, The First Affiliated Hospital of Nanjing Medical University, Nanjing, China. <sup>6</sup>Analysis Center, Nanjing Medical University, Nanjing, China. <sup>7</sup>Department of Neurology and Herbert Irving Comprehensive Cancer Center, Columbia University, New York, NY, USA. <sup>8</sup>Department of Pathology and Cell Biology, Columbia University Irving Medical Center, New York, NY, USA. <sup>9</sup>Department of Medicine, Washington University School of Medicine, Washington University in St. Louis, St. Louis, MO, USA. <sup>10</sup>The Affiliated Wuxi People's Hospital of Nanjing Medical University, Wuxi People's Hospital, Wuxi Medical Center, Nanjing Medical University, Wuxi, China. <sup>11</sup>Department of Clinical Pharmacology, School of Pharmacy, Nanjing Medical University, Nanjing, China. <sup>12</sup>Department of Neurosurgery of Second Affiliated Hospital, Zhejiang University School of Medicine, Hangzhou, China. <sup>13</sup>Liangzhu Laboratory, MOE Frontier Science Center for Brain Science and Brain–Machine Integration, State Key Laboratory of Brain–Machine Intelligence, Zhejiang University, Hangzhou, China. <sup>14</sup>Department of Neurosurgery, The First Affiliated Hospital of Sun Yat-sen University, Guangdong Provincial Key Laboratory of Brain Function and Disease, Guangdong Translational Medicine Innovation Platform, Guangzhou, China. <sup>15</sup>Department of Nutrition and Food Hygiene, Center for Global Health, School of Public Health, Nanjing Medical University, Nanjing, China. <sup>16</sup>Jiangsu Cancer Hospital, Affiliated Cancer Hospital of Nanjing Medical University, Nanjing, China. <sup>17</sup>These authors contributed equally: Daqi Li, Gaoyuan Cui, Kailin Yang, Chenfei Lu, Yuhuan Jiang, Le Zhang. ✉e-mail: [zjx232@njmu.edu.cn](mailto:zjx232@njmu.edu.cn); [xqianmedres@njmu.edu.cn](mailto:xqianmedres@njmu.edu.cn); [zhangqian01@njmu.edu.cn](mailto:zhangqian01@njmu.edu.cn); [drjeremyrich@gmail.com](mailto:drjeremyrich@gmail.com); [drxiuxingwang@163.com](mailto:drxiuxingwang@163.com)

## Methods

This study was conducted in full compliance with the applicable ethical guidelines. The GBM specimens in this study were obtained from the Department of Neurosurgery, The First Affiliated Hospital of Nanjing Medical University. Written informed consent was obtained from all patients. All patient studies were conducted in accordance with the recognized ethical guidelines of the Declaration of Helsinki and Ethics Committee of the First Affiliated Hospital of Nanjing Medical University (2021-SR-076). Detailed patient information is provided in the 'Reporting summary' section. All animal experiments were approved by the Institutional Animal Care and Use Committee (IACUC-2006033-2) at Nanjing Medical University in accordance with NIH and institutional guidelines. All experiments used in this study were approved by the Institutional Ethics Committee of Nanjing Medical University.

### Patient-derived and cell line models

GBM tissues of GSCs were obtained from excess surgical resection samples from patients who underwent treatment at Case Western Reserve University (Cleveland, OH) after review by neuropathology with appropriate consent and in accordance with an IRB-approved protocol (090401). Some of the cell models were provided as generous gifts by Dr Erik Sulman (Duke Health) and transferred via a material transfer agreement from MD Anderson Cancer Center; detailed cell line information is provided in the 'Reporting summary' section. Patient-derived xenografts were produced and propagated as a renewable source of GSCs, in order to minimize in vitro artifacts from cell culture. STR analyses were performed on the tumour model used for authentication. GSCs were cultured as neurospheres in Neurobasal medium (Invitrogen) supplemented with B27 supplement without vitamin A (Life Technologies), Glutamax (Life Technologies), sodium pyruvate (Life Technologies), penicillin–streptomycin, 20 ng ml<sup>-1</sup> EGF and basic fibroblast growth factor (R&D Systems) at 37 °C with 20% oxygen and 5% carbon dioxide. Matched DGCs were maintained in Dulbecco's modified Eagle's medium (DMEM, Hyclone) supplemented with 10% fetal bovine serum (FBS, Gibco) to maintain the differentiation status.

The nonmalignant NSC models ENSA and HNP1 were used in this study. ENSA (ENStem-A) is a human embryonic stem-derived neural progenitor cell (Millipore Sigma, catalogue no. SCC003). HNP1 (STEMEZ HNP1) is a human neural progenitor cell (Neuro-mics, catalogue no. HN60001). NSCs were cultured in Neurobasal medium supplemented with B27, 20 ng ml<sup>-1</sup> EGF and basic fibroblast growth factor. The 293T cells (ATCC, catalogue no. CRL-3216) were used to generate lentiviral particles and were cultured in DMEM medium contains 10% FBS. GL261 (Cyton, 305225) cells were cultured in DMEM medium contains 10% FBS. Mouse GSC MC9 was provided by Dr Fan Lin (Nanjing Medical University).

### In vivo tumourigenesis and animal experiments

To generate *Slc16a3*<sup>fl/fl</sup> mice, *Lyz2-cre* and *Slc16a3*-flox (T011091) mice were obtained from GemPharmatech. Exon2-exon5 of *Slc16a3*-201 (ENSMUST00000070653.12) transcript is recommended as the knockout region. In brief, constructed and tested Cas/gRNA/loxP-donor samples were microinjected into C57BL/6J mice fertilized eggs. Fertilized eggs were transplanted to obtain positive F0 mice, which were confirmed by polymerase chain reaction (PCR) and sequencing. A stable F1 generation mouse model was obtained by mating positive F0 generation mice with C57BL/6JGpt mice.

These mice were crossed with mice expressing *Lyz2-Cre* (T003822; GemPharmatech), yielding *Slc16a3*<sup>wt/fl</sup>, *Lyz2-Cre*<sup>ki/wt</sup> mice, and these mice crossed with each other. Finally, myeloid-specific *Slc16a3*-knockout mice (*Slc16a3*<sup>cko</sup>, gene type: *Slc16a3*<sup>fl/fl</sup>, *Lyz2-Cre*<sup>ki/ki</sup> or *Slc16a3*<sup>fl/fl</sup>, *Lyz2-Cre*<sup>ki/wt</sup>) were generated, and *Slc16a3*<sup>wt/wt</sup>*Lyz2-Cre*<sup>ki/ki</sup> or *Slc16a3*<sup>wt/wt</sup>*Lyz2-Cre*<sup>ki/wt</sup> mice (*Slc16a3*<sup>wt/wt</sup>) from the same breeding colony were used as controls. Information regarding the construction and identification of the genetically modified mouse model is provided in

the Supplementary Table 1. 50,000 mouse glioma stem cells (MC9) and mouse glioma cells (GL261) were implanted into control group or knockout group individually at a depth of 3.5 mm. Both male and female mice aged 4–6 weeks were used for this animal experiment, with ten mice per group (*n* = 10).

Intracranial xenograft models were established by implanting 50,000 human-derived GSCs (3028 GSC and MES28 GSC) and 50,000 human-derived TAMs into the cerebral cortex of BALB/c-Nude (strain No. D000521, GemPharmatech) mice at a depth of 3.5 mm. Female mice at 4–6 weeks of age were randomly assigned to each treatment group (*n* = 10 mice per group) for the animal experiments used in the study.

Intracranial xenografts of mouse glioma cells were created by implanting 50,000 GL261 and 50,000 induced-BMDMs into the cerebral cortex of C57BL/6J (strain no. N000013, GemPharmatech) mice at a depth of 3.5 mm. Female mice at 4–6 weeks of age were randomly assigned to each treatment group (*n* = 10 mice per group) for the animal experiments used in the study. The mice were group-housed (≤5 per cage) and exposed to a consistent 12-h light–dark cycle, with the light period spanning from 6:00 to 18:00 and the dark period from 18:00 to 6:00. They were housed at a controlled ambient temperature of 23 °C ± 2 °C with approximately 50% humidity and had unrestricted access to food and water. Furthermore, the mice were kept in a specific-pathogen-free environment to ensure a contaminant-free setting. Seven days after GSC implantation, the mice were observed daily and euthanized when they presented neurological signs or became moribund. The brains were collected and fixed in 4% formaldehyde, cryopreserved in 30% sucrose, and then cryosectioned. Sections were stained with hematoxylin and eosin for histologic analysis. The maximum tumour burden permitted by the ethics committee is 1,500 cm<sup>3</sup>, and the tumour burden did not exceed this limit. The use of the animals was approved by the Institutional Review Board at Nanjing Medical University.

### Plasmids and lentiviral transduction

For the overexpression assay, full-length human *SLC16A1*, *SLC16A3*, *XRCC6*, *XRCC5*, *FEN1*, *LIG1* and *IQGAP3*; *KU70* deletion mutants (1–260 aa), (261–468 aa), (469–609 aa) and *EP300* deletion mutant (1287–1663 aa) overexpression plasmids were constructed by cloning the coding sequence of each cDNA into the multiple cloning sites of pcDNA 3.1 vector (Invitrogen, V79020). The *KU70* (K317R), *KU70* (E330A), *KU70* (K317R E330A), *FEN1* (K201R), *LIG1* (K226R) and *IQGAP3* (K981R) mutants were generated using the KOD-Plus-Mutagenesis Kit (SMK-101, Toyobo) according to the manufacturer's instructions. For knockdown experiments, all shRNAs used were obtained from Sigma-Aldrich and are listed in the Supplementary Table 2. Nonoverlapping shRNAs were selected based on knockdown efficiency and were then used for all following experiments. Lentiviral particles were generated in 293T cells in Neurobasal complete medium (Life Technologies) with cotransfection with the packaging vectors psPAX2 (Addgene, 12260) and pMD2.G (Addgene, 12259) using a standard calcium phosphate transfection method in neurobasal complete medium.

### Proliferation and neurosphere formation assays

Cell proliferation experiments were conducted by plating cells of interest at a density of 2,000 cells per well in 96-well plates with six replicates. CellTiter-Glo (Promega) was used to measure cell viability at days 1, 3, 5 and 7. All data were normalized to day 1 and presented as mean ± s.d.

Neurosphere formation was measured by in vitro limiting dilution, as previously described<sup>55</sup>. In brief, decreasing numbers of cells per well (50, 20, 10, 5 and 1) were plated into 96-well plates. The presence and number of neurospheres in each well were recorded on day 10 after plating. Extreme limiting dilution analysis was conducted with software available at <http://bioinf.wehi.edu.au/software/elda>, as previously described<sup>56</sup>. All neurosphere and proliferation experiments were performed six times.

### RNA isolation and quantitative RT-PCR

Total cellular RNA from cells were isolated by Trizol reagent (Takara). The PrimeScript cDNA Synthesis Kit (Takara) was used for reverse transcription into cDNA. Quantitative real-time PCR was performed with an Applied Biosystems StepOne Plus cycler using SYBR-Green PCR Master Mix (Thermo Fisher Scientific). Quantitative PCR (qPCR) primers used in this study were as follows: human *KU70* forward 5'-TTGCTTCTGCCTAGCGATACC-3' and reverse 5'-AAACCTGGATCATCAACCGTT-3', 18S RNA forward 5'-AACCCGTTGAACCCCAT-3' and reverse 5'-CCATCCAATCGGTAGTAGCG-3'.

### Western blotting

For western blot analysis, cells and tissues were collected and lysed in RIPA buffer (50 mM Tris-HCl pH 7.5, 150 mM NaCl, 0.5% NP-40, 0.1% SDS and supplemented with protease inhibitors), then incubated on ice for 30 min. Lysates were centrifuged at 4 °C for 10 min at 16,260g, and supernatants were collected. Supernatants were subjected to SDS-polyacrylamide gel electrophoresis and transferred to polyvinylidene difluoride membranes (Millipore). The membranes were blocked with 5% non-fat milk for 1 h and then immunoblotted with primary antibodies overnight at 4 °C, followed by the HRP-conjugated antibody at room temperature for 2 h. The blots were developed by SuperSignal West Pico PLUS Chemiluminescent Substrate (ThermoFisher). Detailed antibodies information is provided in the 'Reporting summary' section.

### Immunofluorescence

Immunofluorescence experiments were performed using GSCs, samples from GBM surgical specimens and xenografts grown in mice. Tumour samples from patients with GBM or xenografts grown in mice were fixed in 4% paraformaldehyde overnight at 4 °C, followed by stained with primary antibodies and overnight cryoprotection with 20% sucrose in PBS at 4 °C. The next day, the sections were washed three times with blocking buffer and incubated with secondary antibody. For GSCs, GSCs were fixed using 4% paraformaldehyde for 30 min and washed with PBS, permeabilized with 0.45% Triton X-100 for 10 min and blocked in 3% bovine serum albumin at room temperature for 2 h, followed by stained with primary antibodies and overnight in PBS at 4 °C. The next day, the cells were washed three times with blocking buffer and incubated with secondary antibody. The images were captured with a Zeiss LSM700 microscope (Carl Zeiss) and processed using ImageJ software (NIH). Detailed antibody information is provided in the 'Reporting summary' section.

### Immunoprecipitation

GSCs were collected and lysed in immunoprecipitation buffer (20 mM Tris-HCl, 150 mM NaCl, 1% Triton X-100, 0.5% sodium deoxycholate, 1 mM DTT) containing PMSF and cocktail protease inhibitor at 4 °C for 30 min, and followed by centrifugation at 16,260 g for 10 min at 4 °C. The primary antibodies or nonspecific IgG was added to the supernatants and incubated at 4 °C overnight. The supernatants were immunoprecipitated by incubation with Protein A/G Plus Agarose (ThermoFisher) at 4 °C for 2 h. Captured proteins were washed with immunoprecipitation buffer three times before immunoblotting. Detailed antibodies information is provided in the 'Reporting summary' section.

### L-Lactate assay

L-Lactate concentrations in GSCs were measured with L-Lactate Assay Kit (Abcam, ab65331). For MCT4 knockdown performed on TAMs, the supernatant of TAMs was obtained after MCT4 knockdown for 48 h, then detected the lactate concentrations of GSCs after treated with the supernatant of TAMs for 12 h. For MCT1 knockdown performed on GSCs, after transduced with shCONT or shMCT1 in GSCs for 48 h, then treated with the supernatant of TAMs for 12 h, L-lactate

concentrations were measured with L-Lactate Assay Kit according to the manufacturer's protocol.

### <sup>13</sup>C-lactate uptake

For an experiment aiming to prove that tumour cells can absorb lactate which secreted by macrophages, equal D-glucose (U-<sup>13</sup>C<sub>6</sub>) was added into the no glucose RPMI 1640 medium (ThermoFisher) of isolated TAMs for 12 h. After the cocultured of GSCs and TAMs in the transwell system for 12 h, GSCs were collected. To detect the difference between GSCs and NSCs, equally L-lactate (U-<sup>13</sup>C<sub>3</sub>) was added into the Neurobasal medium for 48 h, GSCs and NSCs were collected. To detect the difference of absorbing lactate ability between MES28 GSC and DGC, equal L-lactate (U-<sup>13</sup>C<sub>3</sub>) was added into the Neurobasal medium or DMEM medium for 48 h, GSC and DGC were collected. Organic acids were analysed at LipidALL Technologies. In brief, metabolites were extracted from cells using acetonitrile: water (1:1) and derivatised with 3-nitrophenylhydrazine<sup>57</sup>. Metabolites were analysed on a Jasper HPLC coupled to Sciex 4500 MD system. In brief, individual metabolites were separated on a Phenomenex Kinetex C18 column (100 mm × 2.1 mm, 2.6 μm) using 0.1% formic acid in water as mobile phase A and 0.1% formic acid in acetonitrile as mobile phase B. Undecanoic acid purchased from Sigma-Aldrich were used as internal standards for quantitation.

### Mass spectrometry analysis

To identify the differential sites between GSCs and NSCs, GSCs and NSCs were stimulated by 10 mM lactate for 24 h before collection and then lysed. After the protein quantitation, lysis contained equally protein were sent for mass spectrometry analysis to detect the protein level and lactylation level.

### In vitro lactylation assay

The His-tagged KU70 WT and KU70 K317R proteins were expressed by the ExpiSf Expression System, then incubated with P300/CBP/KAT2B protein and lactyl-CoA was also added. Reactions were incubated at 37 °C for 30 min. Immunoblot analysis were performed after the reaction.

### In vitro acetylation assay

The His-tagged KU70 WT and KU70 K317R proteins were incubated with P300/CBP/KAT2B protein and acetyl-CoA was also added. Reactions were incubated at 37 °C for 30 min. Immunoblot analysis were performed after the reaction.

### GST pull-down assay

The GST-tagged KU70 WT and KU70 K317R proteins were expressed by the ExpiSf Expression System, then incubated with P300 protein and lactyl-CoA was also added. The purified His-tagged KU80 protein was also added into the reaction system. Then the GST pull-down assay was performed based on the instruction (ThermoFisher, 21516).

### Peptide synthesis

CPP was synthesized by GenScript. The sequence of KU70 K317-Peptide is HLYVSPWGGLLLPSDTKRS, the sequence of KU70 K317R-Peptide is HLYVSPWGGLLLPSDTRRS.

### HR and NHEJ assay

DR-GFP and NHEJ-GFP reporter systems were employed to examine the DNA repair efficiency. In brief, GSCs stably expressing the interference plasmid or rescued plasmids or control GSCs were seeded into six-well plates in triplicate. A total of 24 h later, the cells in each well were transfected with a complex that contained 3 μl Lipofectamine 3000, 500 ng DR-GFP or NHEJ-GFP and 500 ng I-SceI plasmids, which were employed to generated DNA DSBs. After transfection 24 h, the cells were treated with indicated reagents. After transfection 48 h, the cells

were collected and analysed by flow cytometric analysis, with sorting by GFP-positive cells. The ratio of repair efficiency was calculated as described previously<sup>58</sup>.

### Comet assay

GSCs expressing shCONT, shKU70, stably expressing KU70 WT or KU70 K317R with endogenous KU70 depleted were seeded into six-well plates with a density of 100,000 cells per well. After treatment with cisplatin as indicated, the cells were collected at the indicated time and then utilized for Comet assays according to the manufacturer's instructions (RD systems, 4250-50-ESK). In brief, the cells were embedded in low melting agarose on a glass slide and then immersed in lysis buffer for 1 h at 4 °C. The slides were then incubated with electrophoresis buffer for about 40 min to unwind DNA. Subsequently, electrophoresis was performed for 25 min at 25 V. Next, the slide was stained with propidium iodide and then covered by cover-glass. For quantification, comets on each gel were observed using a fluorescence microscope. Tail length and tail moment were measured to evaluate the degree of DNA damage.

### Senescence assay

The senescence-associated  $\beta$ -galactosidase (SA- $\beta$ -gal) activity was quantified by means of flow cytometry and The Senescence  $\beta$ -Galactosidase Activity Assay Kit (CST, 35302). In brief, the cells were incubated with Bafilomycin A1 (CST, 54645) at 100 nM for 1 h at 37 °C. Then, SA- $\beta$ -Gal Fluorescent Substrate (CST, 38154) was added, mixed gently and incubated at 37 °C for 3 h. The cells were washed three times with PBS before being trypsinized and inactivated with PBS containing 2% FBS. Then flow cytometry were used to evaluate the percentage of SA- $\beta$ -gal-positive cells.

### Apoptosis analysis

In brief, GSCs expressing shCONT, shKU70, stably expressing KU70 WT or KU70 K317R with endogenous KU70 depleted were collected at the indicated times and costained with Annexin-V-FITC and propidium iodide following manufacturer instructions (BioLegend, 640914).

### Oxygen consumption rate measurement

The oxygen consumption rate was detected Seahorse XF Cell Mito Stress Test Kit (Agilent) according to the manufacturer's protocol. Assembled sensor cartridge and utility plate were placed in a non-CO<sub>2</sub> 37 °C incubator overnight with 200  $\mu$ l water in each well. Water was discarded and each well of the utility plate was filled with 200  $\mu$ l of pre-warmed Seahorse XF Calibrant. The assembled sensor cartridge with the utility plate was placed in a non-CO<sub>2</sub> 37 °C incubator for 45–60 min before loading the drug ports of the sensor cartridge. A total of  $3 \times 10^4$  GSCs were plated on a Seahorse plate coated with Matrigel (Corning) in XF DMEM medium. Oxygen consumption was recorded by a Seahorse XFe96 Analyzer (Agilent) using the Mito Stress Test programme, in which cells were sequentially perturbed by 2  $\mu$ M oligomycin, 0.5  $\mu$ M CCCP and 0.5  $\mu$ M Rot/AA.

### Isolation and differentiation of PBMC

Human PBMC were isolated from human blood by Ficoll-Paque PLUS (GE Healthcare). In brief, human blood was diluted with an equal volume of PBS and thoroughly blended. The blood dilution was then placed over a half-volume of Ficoll-Paque PLUS and centrifuged at 452g for 20 min. The cells from the middle layer were collected in 15 ml tubes. After washing and erythrocyte lysis, cells were cultured in RPMI 1640 medium. Then, suspended cells were washed away with PBS, and the adherent monocytes were trypsinized and subjected to differentiation steps. For the PBMC differentiated to macrophage, the cells were cultured in RPMI 1640 medium with 200 ng ml<sup>-1</sup> M-CSF (PeproTech, 300-25-10). After 7 days, the cells were cultured with 25 ng ml<sup>-1</sup> IL4 and 25 ng ml<sup>-1</sup> IL13 for another 48 h.

### Isolation and activation of cytotoxic T cells

Cytotoxic T cells, also known as CD8<sup>+</sup> T cells, were isolated from human blood by EasySep Direct Human CD8<sup>+</sup> T Cell Isolation Kit (STEMCELL, 19663). To activate the cytotoxic function of CD8<sup>+</sup> T cells, cells were cultured in RPMI 1640 medium with Human T-Activator CD3/CD28 (ThermoFisher, 11161D) and 200 IU ml<sup>-1</sup> IL2 (PeproTech, 200-02).

### T cell-mediated cytotoxicity assay

T cell-mediated cytotoxicity was determined by Cytotox96 nonradioactive cytotoxicity assay kit (Promega, G1780) based on the release of lactate dehydrogenase.

In brief, PBMC-derived tumour-promoting macrophages were cocultured with GSCs in the transwell system with the treatment of syroingopine (10  $\mu$ M) for 24 h at first, after expansion and activation, activated cytotoxic T cells were collected. Isolated GSCs were cocultured with T cells according to different ratios for 5 h with the combination of anti-PD-1 antibody (200 ng). T cell-mediated cytotoxicity on GSCs was assessed according to the manufacturer's instructions.

### BMDMs cell culture

BMDMs were derived from bone marrows isolated from C57BL/6J mice according to an established protocol<sup>59</sup> and cultured in RPMI1640 medium with 10% FBS.

### Flow cytometry

To obtain CD11b<sup>+</sup>/CD163<sup>+</sup> TAMs from human GBMs, cells dissociated from human GBM tumours were incubated with APC-conjugated Rat anti-human CD11b (BD Pharmingen, 553312) and PE-conjugated mouse anti-human CD163 (BD Pharmingen, 556018) for 30 min at 4 °C, followed by flow cytometric using a BD FACSAria II cell sorter. Sorted TAMs were cultured in the RPMI 1640 medium contains 10% FBS for the following experiments.

For the detection of stemness of mouse GSC, cells were stained by anti-CD133 (BioLegend, 141203) and anti-SOX2 (BioLegend, 656103) at 4 °C for 45 min individually. To detect the PD-1 expression of cytotoxic T cells with syroingopine treatment, CD8<sup>+</sup> T cells were collected in PBS after cytotoxicity assay, then cell suspension was incubated with anti-CD279 (BD Pharmingen, 561035) antibodies at 4 °C for 45 min.

For mice experiments, single-cell suspensions were prepared from fresh mouse tumour tissues on day 25 after injection. Brain tumours were dissected, minced and digested with 5 mg ml<sup>-1</sup> collagenase type II (ThermoFisher) and 0.1 mg ml<sup>-1</sup> DNase I recombinant (Sigma-Aldrich) at 37 °C for 30 min. The cells were passed through a 40- $\mu$ m filter to remove clumps and maintain single-cell suspensions. Brain cell suspensions were separated over 30% Percoll gradients at 700g for 30 min at 4 °C to enrich tumour-infiltrating immune cells. For the immune landscape experiment, cell suspension was incubated with anti-CD45 (BD Horizon, 567799), anti-CD11b (BD Pharmingen, 561690), anti-Ly-6G and LY-6C (BD Pharmingen, 553126), anti-F4/80 (BioLegend, 123127), anti-CD11c (BD Pharmingen, 561022) and anti-MHC-II (BioLegend, 107607) antibodies for 45 min on ice to detect the macrophage, microglia, myeloid-derived suppressor cell (MDSC) and dendritic cell populations, cell suspension was incubated with anti-CD45 (BD Horizon, 567799), anti-NK-1.1 (BD Horizon, 563220), anti-CD3 (BD Pharmingen, 561827), anti-CD4 (BD Horizon, 563232), anti-CD8 (BD Pharmingen, 561097) and anti-CD25 (BD Pharmingen, 558642) antibodies at 4 °C for 45 min, followed by fixation and permeabilization for cytokine staining. Then cell suspension was incubated with anti-Foxp3 (eBioscience, 17-5773-82) at 4 °C for another 45 min to detect the CD8<sup>+</sup> T cell, natural killer cell, CD4<sup>+</sup> T cell also the Treg in CD4<sup>+</sup> T cell populations. To quantify T cells and T cell cytokine expression, cells were stained with anti-CD45 (BD Horizon, 567799) and anti-CD8 (BD Horizon, 563786; BD Pharmingen, 561966) antibodies for 45 min on ice, followed by fixation and permeabilization for cytokine staining. After being permeabilized with fixation/permeabilization buffer, the cell suspension

was incubated with anti-granzyme B (BioLegend, 372213) antibodies at 4 °C for 45 min. To evaluate the CD8<sup>+</sup> T cell exhaustion status, cells were stained with anti-CD45 (BD Horizon, 567799), anti-CD8 (BD Pharmingen, 561097), anti-CD279 (BD Pharmingen, 562671) and anti-LAG3 (BD Pharmingen, 552380) antibodies at 4 °C for 45 min.

For the isolation of macrophage and microglia from cell suspensions, cells were stained with anti-CD45 (BD Horizon, 567799), anti-F4/80 (BioLegend, 123127) and anti-CD11b (BD Pharmingen, 561690) antibodies at 4 °C for 45 min. The F4/80<sup>+</sup> in CD11b<sup>+</sup>CD45<sup>high</sup> cell population group was identified as macrophage, and the CD11b<sup>+</sup>CD45<sup>med</sup> cell population group was identified as microglia; then, cell sorting was performed by Flow cytometry. Splenocytes were stained and examined by flow cytometry to characterize the immune phenotype of CD45<sup>+</sup> infiltrating cells.

For mouse GSC isolation *in vivo*, brain cell suspension from *Slc16a3*<sup>wt/wt</sup> *Lyz2-Cre* and *Slc16a3*<sup>n/n</sup> *Lyz2-Cre* bearing mouse MC9-GFP GSC were stained with anti-CD133 (BioLegend, 141203) and anti-SOX2 (BD Pharmingen, 560294) antibodies at 4 °C for 45 min. Sox2<sup>+</sup>Prom1<sup>+</sup> cells in GFP cells were defined as GSC. All flow samples for detection were run on the LSR Fortessa (BD) system and data were analysed using FlowJo (v.10).

### RNA-seq and data analysis

Total RNA was extracted with RNAiso Plus reagent (Takara) according to the manufacturer's instructions. RNA-seq was performed using BGISEQ-500 platforms. FASTQ sequencing reads were trimmed using Trim Galore (RRID:SCR\_011847), and transcript quantification was conducted using Salmon with the quasi-mapping mode<sup>60</sup>. Salmon 'quant' files were converted using Tximport<sup>61</sup>, and differential expression analysis was performed using DESeq2<sup>62</sup>. GSEA was performed by selecting differentially expressed genes (false discovery rate-corrected *P*value <0.05), generating a preranked list and importing the preranked list into the GSEA desktop application (<http://www.gsea-msigdb.org/gsea/index.jsp>).

### scRNA-seq data analysis

Raw sequencing reads were aligned to human genome reference GRCh38 using Cell Ranger (10x Genomics). First, quality controls were performed to remove low-expression genes and low-quality cells. We used DoubletFinder to identify potential single-cell doublets, setting the doublet rate to 7.5%<sup>63</sup>. Genes expressed in <3 cells and low-quality cells containing <500 genes or with a mitochondrial gene ratio >20% or a ribosomal gene ratio >50% were removed. After the removal of low-quality genes and cells, the single-cell matrices were normalized, clustered and visualized using Seurat<sup>64</sup>, and batch effects were corrected using Harmony<sup>65</sup>. Normalization was performed using SCTransform function, and a principal component analysis was conducted on 2,000 variable genes using RunPCA. After correcting for batch effects using RunHarmony, the first 30 principal components were subjected to uniform manifold approximation and projection (UMAP) dimensionality reduction. Cluster analysis was performed using FindNeighbors and FindClusters. The lactate transmembrane transport signature (GOMF\_LACTATE\_TRANSMEMBRANE\_TRANSPORTER\_ACTIVITY) was calculated for each cell using AUCell<sup>66</sup>.

### Spatial transcriptomics data processing

For spatial data analysis, we acquired the spatially resolved RNA-seq datasets using the SPATADData package. Spatial transcriptomic data were imported using the import function SPATA2::initiateSpataObject\_10x (ref. 67), which performed a series of computations such as count normalization, dimensionality reduction and clustering. The runAutoencoderDenoising function was utilized to denoise the data. All subsequent analyses were performed on the denoised expression data.

### Statistics and reproducibility

All statistical data are presented as the mean ± s.d., the box plots show the median (centre) and the 25th and 75th percentiles (bounds of box)

and the whiskers indicate the minimum and maximum values. All experiments were repeated at least three times independently with similar results. Statistical significance was determined by two-tailed unpaired Student's *t*-test performed with Prism 9.2.0 (GraphPad) and a likelihood ratio test comparing the single-hit model to alternative models (two-sided). For Kaplan–Meier survival curves, statistical differences between groups were determined by two-tailed log-rank test. The exact *P* value of some experiments have been listed in the Supplementary Table 3. No statistical methods were used to predetermine sample sizes but our sample sizes are similar to those reported in previous publications (PMID: 34615656, 2022; PMID: 37198486, 2023). No data were excluded from the analyses. The normality and equal variance of data distribution were formally test as appropriate. Unless stated otherwise, the experiments were not randomized and the investigators were not blinded to allocation during experiments and outcome assessment.

### Reporting summary

Further information on research design is available in the Nature Portfolio Reporting Summary linked to this article.

### Data availability

RNA-seq data that support the findings of this study have been deposited in the Gene Expression Omnibus (GEO) under accession code [GSE266884](https://www.ncbi.nlm.nih.gov/geo/query/acc.cgi?acc=GSE266884) (<https://www.ncbi.nlm.nih.gov/geo/query/acc.cgi?acc=GSE266884>). Mass spectrometry data have been deposited in ProteomeXchange with the primary accession code [PXD069969](https://proteomecentral.proteomexchange.org/cgi/GetDataset?ID=PXD069969) (<https://proteomecentral.proteomexchange.org/cgi/GetDataset?ID=PXD069969>) and [PXD070007](https://proteomecentral.proteomexchange.org/cgi/GetDataset?ID=PXD070007) (<https://proteomecentral.proteomexchange.org/cgi/GetDataset?ID=PXD070007>). The human GBM data were derived from the TCGA Research Network (<http://cancergenome.nih.gov/>) and CCGA Research Network (<https://www.cgga.org.cn/>). All other data supporting the findings of this study are available from the corresponding author on reasonable request. Source data are provided with this paper.

### References

- Flavahan, W. A. et al. Brain tumor initiating cells adapt to restricted nutrition through preferential glucose uptake. *Nat. Neurosci.* **16**, 1373–1382 (2013).
- Hu, Y. & Smyth, G. K. ELDA: extreme limiting dilution analysis for comparing depleted and enriched populations in stem cell and other assays. *J. Immunol. Methods* **347**, 70–78 (2009).
- Li, B. et al. Microbiota depletion impairs thermogenesis of brown adipose tissue and browning of white adipose tissue. *Cell Rep.* **26**, 2720–2737.e2725 (2019).
- Zhao, F., Kim, W. & Gao, H. ATE1 promotes shieldin-complex-mediated DNA repair by attenuating end resection. *Nat. Cell Biol.* **23**, 894–904 (2021).
- Ying, W., Cheruku, P. S., Bazer, F. W., Safe, S. H. & Zhou, B. Investigation of macrophage polarization using bone marrow derived macrophages. *J. Vis. Exp.* **23**, 50323 (2013).
- Patro, R., Duggal, G., Love, M. I., Irizarry, R. A. & Kingsford, C. Salmon provides fast and bias-aware quantification of transcript expression. *Nat. Methods* **14**, 417–419 (2017).
- Soneson, C., Love, M. I. & Robinson, M. D. Differential analyses for RNA-seq: transcript-level estimates improve gene-level inferences. *F1000Res* **4**, 1521 (2015).
- Love, M. I., Huber, W. & Anders, S. Moderated estimation of fold change and dispersion for RNA-seq data with DESeq2. *Genome Biol.* **15**, 550 (2014).
- McGinnis, C. S., Murrow, L. M. & Gartner, Z. J. DoubletFinder: doublet detection in single-cell RNA sequencing data using artificial nearest neighbors. *Cell Syst.* **8**, 329–337.e324 (2019).

64. Butler, A., Hoffman, P., Smibert, P., Papalexi, E. & Satija, R. Integrating single-cell transcriptomic data across different conditions, technologies, and species. *Nat. Biotechnol.* **36**, 411–420 (2018).
65. Korsunsky, I., Millard, N. & Fan, J. Fast, sensitive and accurate integration of single-cell data with Harmony. *Nat. Methods* **16**, 1289–1296 (2019).
66. Aibar, S. & Gonzalez-Blas, C. B. SCENIC: single-cell regulatory network inference and clustering. *Nat. Methods* **14**, 1083–1086 (2017).
67. Ravi, V. M. et al. Spatially resolved multi-omics deciphers bidirectional tumor-host interdependence in glioblastoma. *Cancer Cell* **40**, 639–655.e613 (2022).

## Acknowledgements

This work was supported by the National Natural Science Foundation of China (grant nos. 82525047 to X.W and 82573312 to Q.Z).

## Author contributions

X.W., D.L., J.N.R., Q.Z. and X.Q. conceived the project and designed the studies. D.L., G.C., C.F.L., Y.J. and L.Z. conducted the experiments. Q.Z. and D.L. wrote the paper. D.G., J.G., Q.L. and H.Y. performed the data analysis and bioinformatics analysis under the supervision of Q.W.

and Z.S. Z.Z., J.Z., G.J., Y.C., Q.G.Z., Q.W., F.L., J.S., C. Liu, C. Li, Y.Y. and N.Z. commented on the study. X.W., K.Y., R.C.G. and D.D. revised the manuscript and supervised the work.

## Competing interests

The authors declare no competing interests.

## Additional information

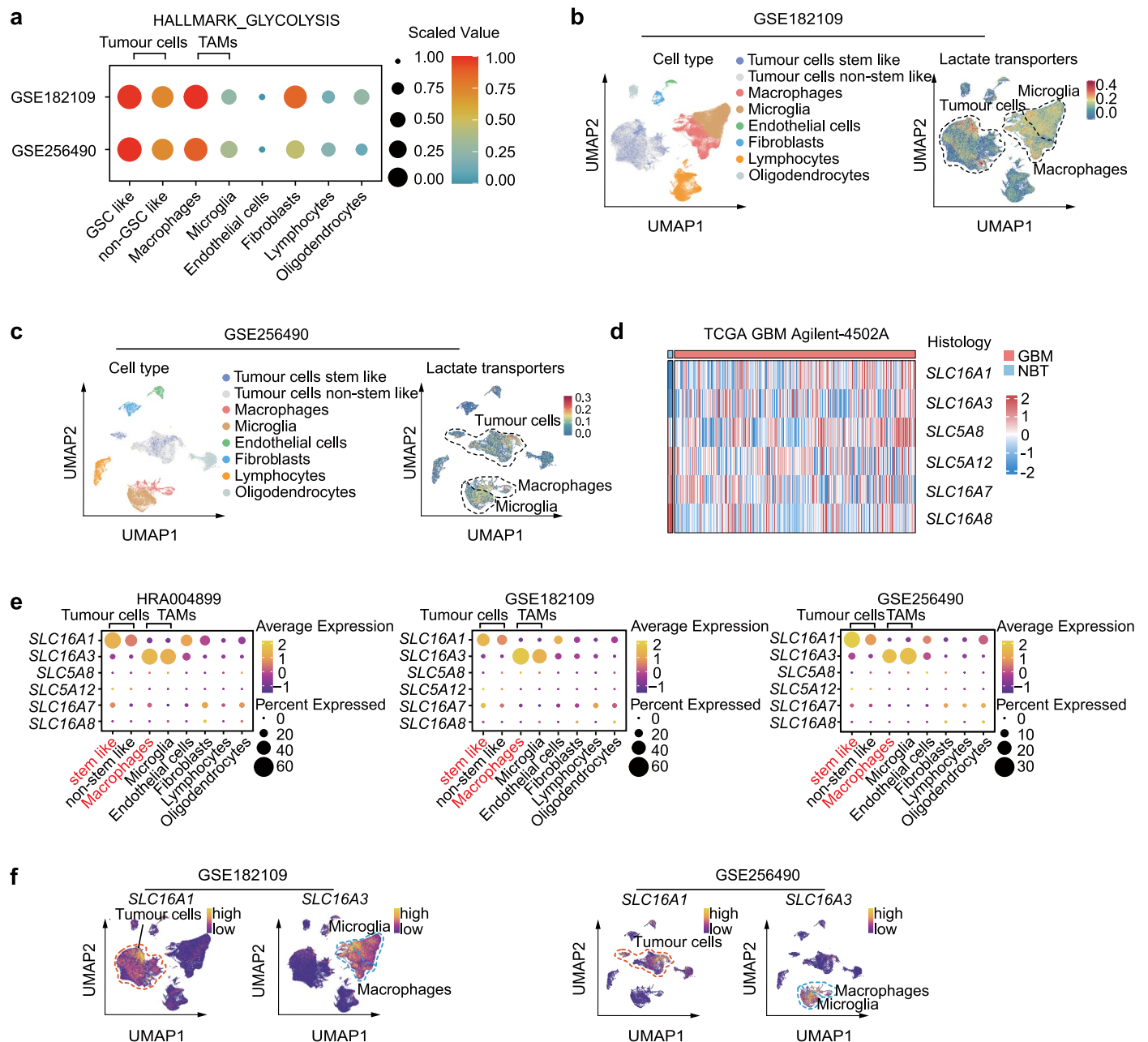
**Extended data** is available for this paper at <https://doi.org/10.1038/s41556-025-01839-y>.

**Supplementary information** The online version contains supplementary material available at <https://doi.org/10.1038/s41556-025-01839-y>.

**Correspondence and requests for materials** should be addressed to Junxia Zhang, Xu Qian, Qian Zhang, Jeremy N. Rich or Xiuxing Wang.

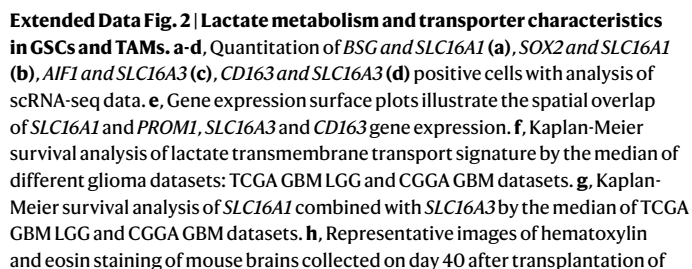
**Peer review information** *Nature Cell Biology* thanks Zhimin Lu and the other, anonymous, reviewer(s) for their contribution to the peer review of this work.

**Reprints and permissions information** is available at [www.nature.com/reprints](http://www.nature.com/reprints).

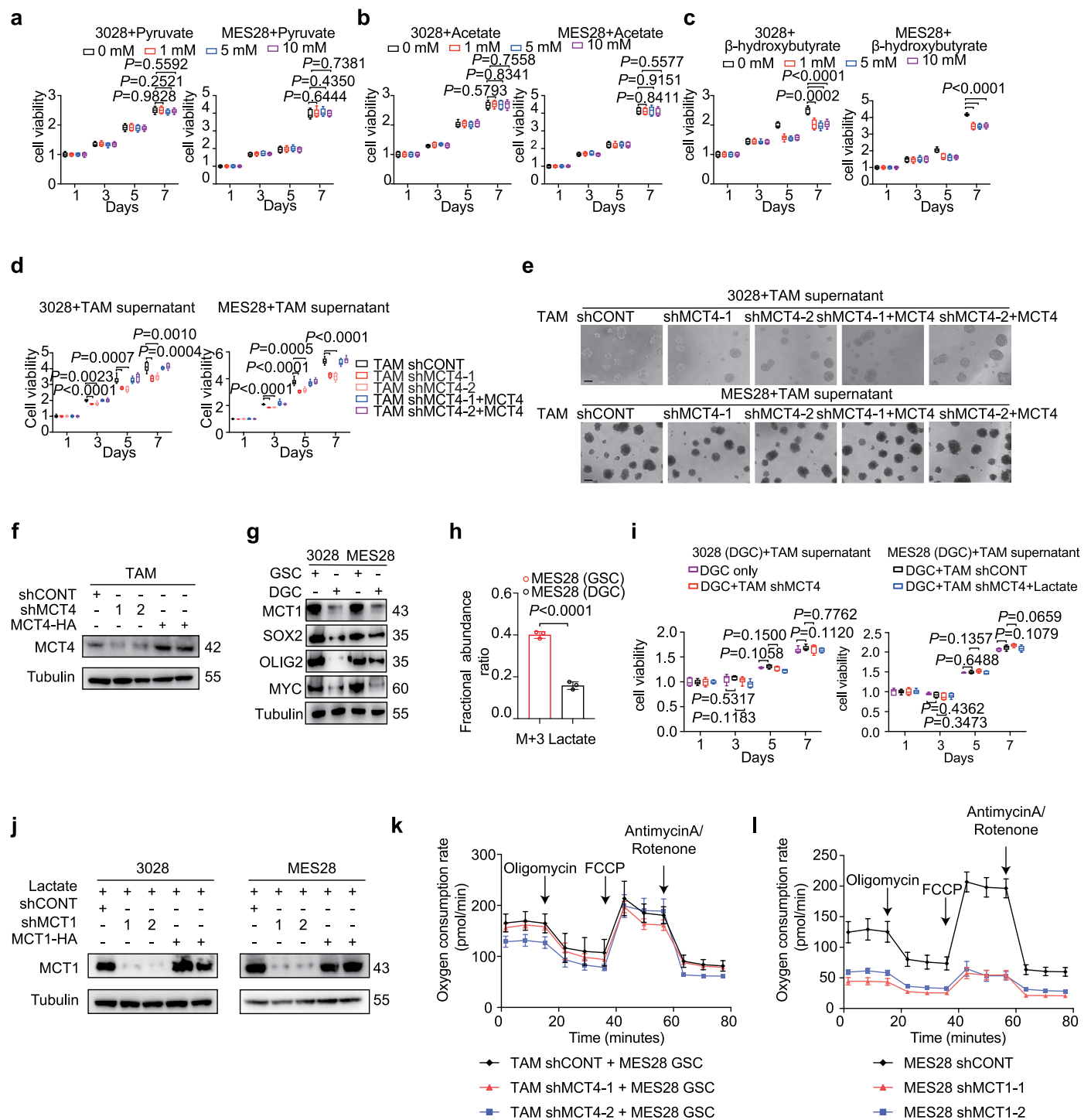


**Extended Data Fig. 1 | Lactate metabolism and transporter characteristics in GSCs and TAMs. a**, Dot plot of analyze HALLMARK\_GLYCOLYSIS pathway in different cell types using scRNA-seq data. **b, c**, UMAP dimensional reduction of the basis of the expression pattern of lactate transmembrane transport in cell-type clusters. **d**, Heatmap of expression of 6 genes in lactate transmembrane

transport pathway from TCGA-GBM Agilent-4502A database. **e**, Dot plot of analyze 6 genes in lactate transmembrane transport pathway using scRNA-seq data (HRA004899, GSE182109 and GSE256490). **f**, UMAP plot showing the expression pattern of *SLC16A1* and *SLC16A3* using single-cell RNA-seq data (GSE182109 and GSE256490).



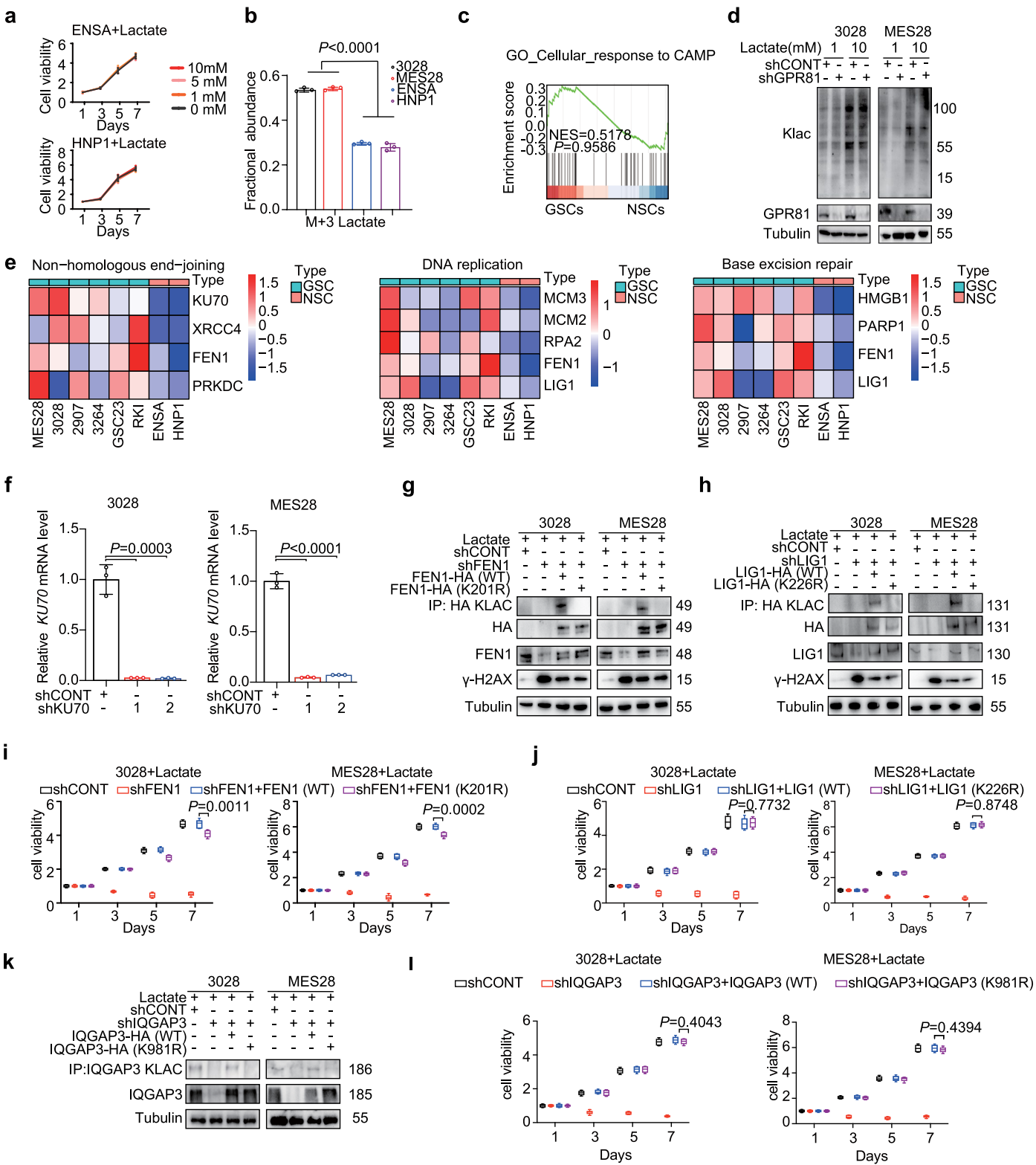
Nature Cell Biology



### Extended Data Fig. 3 | Lactate transporting between GSCs and TAMs via MCT1-MCT4 supports GSC proliferation.

**a**, Cell viability detections after different concentrations (0–10 mM) of pyruvate-stimulated GSCs. Results were measured using the CellTiter-Glo assay (n = 6). **b**, Cell viability detections after different concentrations (0–10 mM) of acetate-stimulated GSCs. Results were measured using the CellTiter-Glo assay (n = 6). **c**, Cell viability detections after different concentrations (0–10 mM) of  $\beta$ -hydroxybutyrate-stimulated GSCs. Results were measured using the CellTiter-Glo assay (n = 6). **d**, Cell viability detections of GSCs after being stimulated with the supernatant of TAMs transduced with shCONT, shMCT4-1, shMCT4-2 and rescued by MCT4 (n = 6). **e**, Representative images of neurospheres of 3028 and MES28 after being stimulated with the supernatant of TAMs transduced with shCONT, shMCT4-1, shMCT4-2 and rescued by MCT4 (n = 6). Scale bar, 100  $\mu$ m. **f**, Immunoblot analysis of MCT4 level in TAM transduced with shCONT, shMCT4-1, shMCT4-2

and rescued by MCT4. **g**, Immunoblot analysis of MCT1 level in 2 GSCs and 2 compared DGCs. **h**, Fractional abundance of M + 3 lactate in MES28 GSC and MES28 DGC when stimulated with 10 mM  $^{13}\text{C}_3$ -labelled lactate (n = 3). **i**, Cell viability detections of DGCs individually or treated with the supernatant of TAMs transduced with control shRNA, shMCT4, or shMCT4 rescued with lactate (n = 6). **j**, Immunoblot analysis of MCT1 level in 3028 and MES28 GSCs transduced with shCONT, shMCT1-1, shMCT1-2 and rescued by MCT1. **k**, Oxygen consumption rates of MES28 GSC co-cultured with supernatant of TAM (n = 4). **l**, Oxygen consumption rates of MES28 GSC expressing non-targeting or MCT1-targeting shRNAs (n = 4). Data are presented as mean  $\pm$  SD (**h**, **k**, **l**), box plots show the median (centre), the 25th and 75th percentiles (bounds of box), and whiskers indicate the minimum and maximum values (**a–d**, **i**). Statistical significance was determined by a two-tailed Student's t-test.

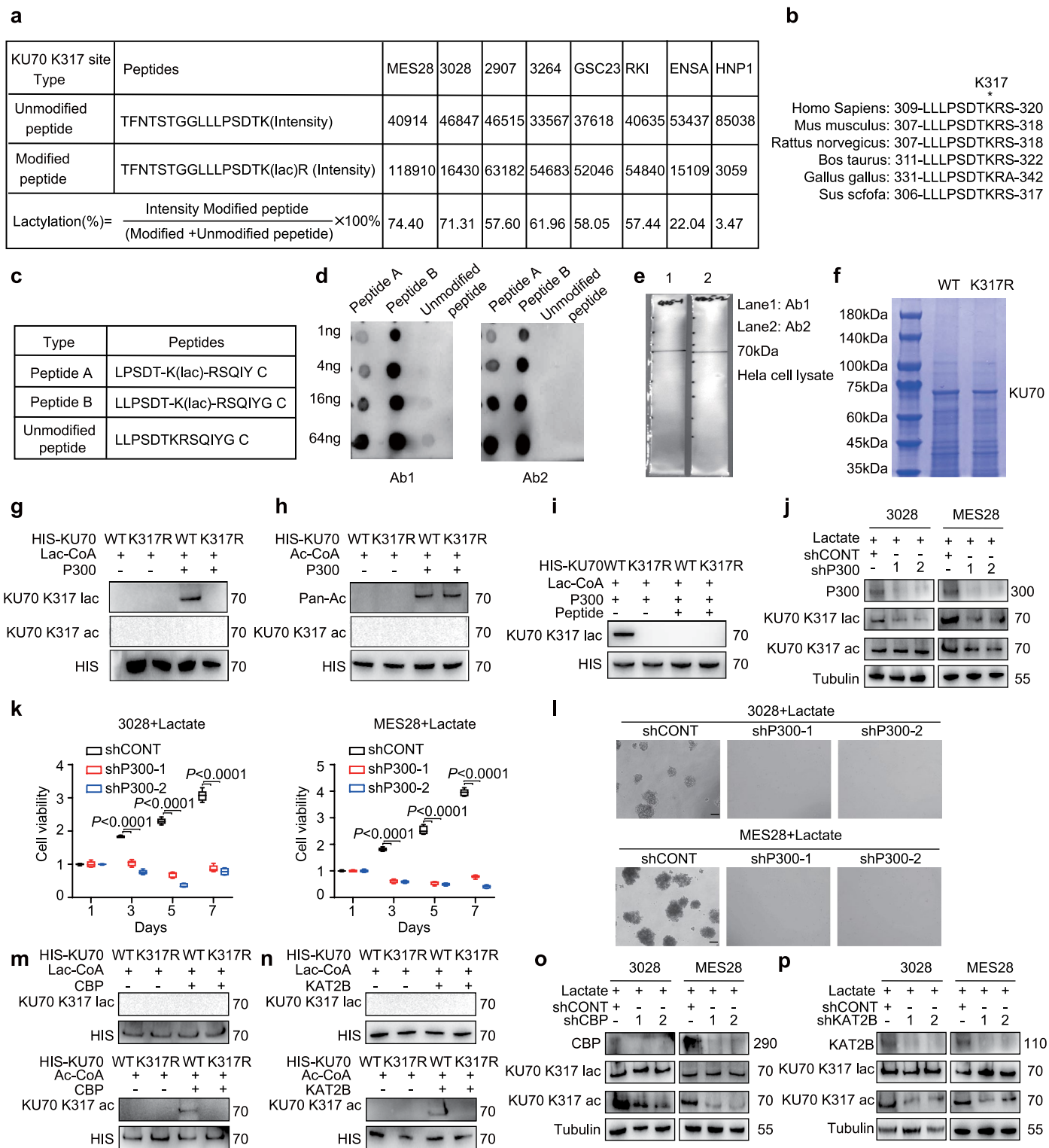


Extended Data Fig. 4 | See next page for caption.

**Extended Data Fig. 4 | TAMs-derived lactate induced the lactylation of DNA damage repair protein KU70 K317 leads to GSC proliferation.**

**a**, Cell viability detections after different concentrations (0–10 mM) of lactate stimulated NSCs (n = 6). **b**, Fractional abundance of M + 3 lactate in GSCs and NSCs when stimulated with 10 mM  $^{13}\text{C}_3$ -labelled lactate (n = 3). **c**, Gene Set Enrichment Analysis (GSEA) scores calculated for RNA sequencing data using Gene Ontology (GO) gene sets showing the correlation between GSCs and NSCs with the Cellular response to CAMP signaling pathway. **d**, Immunoblot analysis of the pan-lactylation level of 3028 (left) and MES28 (right) after transduction with control shRNA and shGPR81 by stimulating with 1 mM or 10 mM lactate. **e**, Heatmaps showing lactylated proteins involved in non-homologous end joining, DNA replication, and base excision repair pathways in GSCs. **f**, *KU70* mRNA levels were assayed by qRT-PCR in GSCs with KU70 knockdown using two independent shRNAs. A shCONT was used as the control (n = 3). **g**, Immunoblot analysis of GSCs  $\gamma$ -H2AX level with the stimulation of 10 mM lactate combined transduced with shCONT, shFEN1, shFEN1 rescued with FEN1-WT or FEN1-K201R. **h**, Immunoblot analysis of GSCs  $\gamma$ -H2AX level with the stimulation of 10 mM

lactate combined transduced with shCONT, shLIG1, or shLIG1 rescued with LIG1-WT or LIG1-K226R. **i**, Cell viability detections of GSCs under the stimulation of 10 mM lactate combined transduced with shCONT, shFEN1, shFEN1 rescued with FEN1-WT or FEN1-K201R. Results were measured using the CellTiter-Glo assay (n = 6). **j**, Cell viability detections of GSCs under the stimulation of 10 mM lactate combined transduced with shCONT, shLIG1, or shLIG1 rescued with LIG1-WT or LIG1-K226R. Results were measured using the CellTiter-Glo assay (n = 6). **k**, Immunoblot analysis of IQGAP3 and IQGAP3 lactylation levels combined transduced with shCONT, shIQGAP3, or shIQGAP3 rescued with IQGAP3-WT or IQGAP3-K981R by stimulating with 10 mM lactate. **l**, Cell viability detections of GSCs under the stimulation of 10 mM lactate combined transduced with shCONT, shIQGAP3, or shIQGAP3 rescued with IQGAP3-WT or IQGAP3-K981R. Results were measured using the CellTiter-Glo assay (n = 6). Data are presented as mean  $\pm$  SD (**a**, **b**, **f**), box plots show the median (centre), the 25th and 75th percentiles (bounds of box), and whiskers indicate the minimum and maximum values (**i**, **j**, **l**). Statistical significance was determined by a two-tailed Student's t-test.

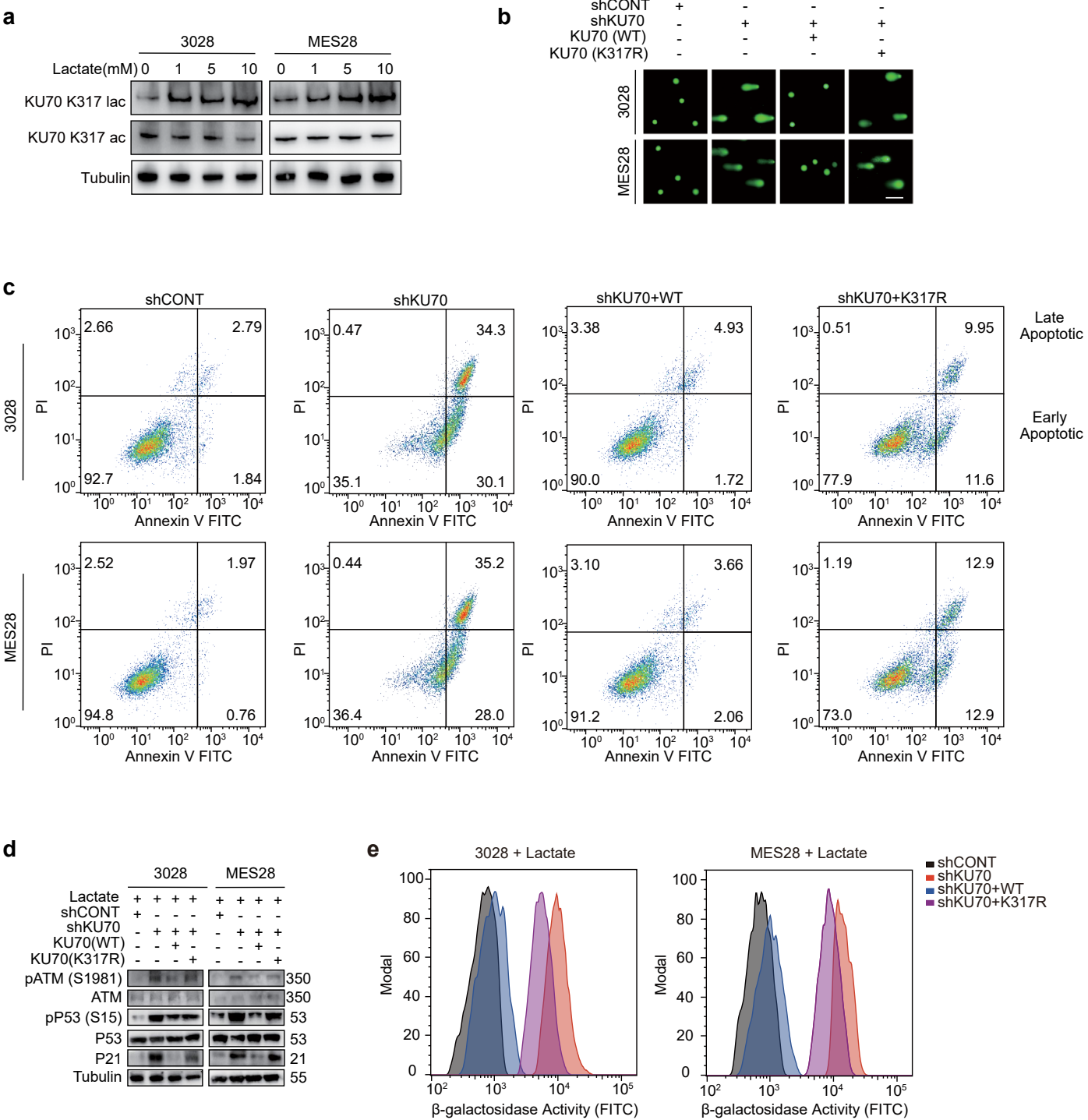


Extended Data Fig. 5 | See next page for caption.

**Extended Data Fig. 5 | TAMs-derived lactate induced the lactylation of DNA damage repair protein KU70 K317 leads to GSCs proliferation.**

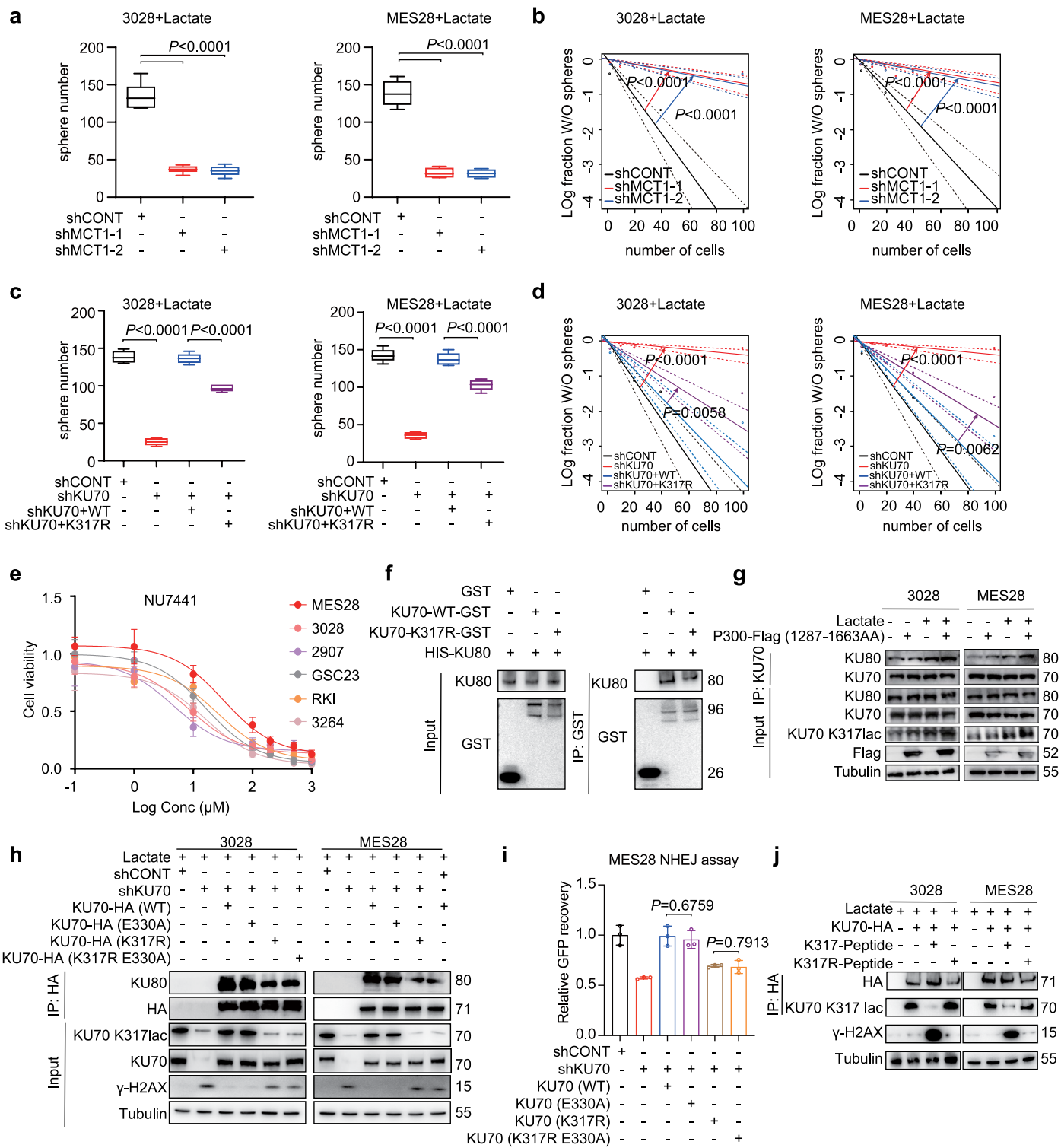
**a**, Quantification of lactylation percentage for KU70 K317 by intensity values of LC/MS. **b**, Sequence alignment of KU70 in various species. \*Lactylation site. **c**, The synthetic KU70 peptides spanning lactylation K317 and non-modified peptide. **d**, Dot-blot results validated the efficiency of the KU70 K317lac specific antibodies when detecting modified peptides. **e**, Immunoblot results showed the KU70 K317lac specific antibodies when detecting the lysate of Hela cell line. **f**, Coomassie blue staining shown the purified His-KU70 WT and His-KU70 K317R. **g**, Purified His-KU70 WT or K317R were incubated with or without P300 for 30 min. Lac-CoA was added. Immunoblot analysis were performed. **h**, Purified His-KU70 WT or K317R were incubated with or without P300 for 30 min. Ac-CoA was added. Immunoblot analysis were performed. **i**, KU70 K317 lactylation-specific antibody was validated by experiments of the purified His-KU70 WT or K317R incubated with or without the modified peptide (Peptide A). P300 and Lac-CoA were added. **j**, KU70 K317 lactylation and KU70 K317 acetylation-specific antibody were used to detect the modification level after

P300 knockdown in GSCs. **k**, Cell viability detections of 3028 and MES28 GSCs after deletion of P300 under the stimulation of lactate ( $n = 6$ ). **l**, Representative images of neurospheres of 3028 (top) and MES28 (bottom) under the stimulation of 10 mM lactate combined transduced with shCONT, shP300-1 and shP300-2 ( $n = 6$ ). Scale bar, 100  $\mu$ m. **m**, Purified His-KU70 WT or K317R were incubated with or without CBP for 30 min. Lac-CoA (top) or Ac-CoA (bottom) was added. Immunoblot analysis were performed. **n**, Purified His-KU70 WT or K317R were incubated with or without KAT2B for 30 min. Lac-CoA (top) or Ac-CoA (bottom) was added. Immunoblot analysis were performed. **o**, KU70 K317 lactylation and KU70 K317 acetylation-specific antibody were used to detect the modification level after CBP knockdown in GSCs. **p**, KU70 K317 lactylation and KU70 K317 acetylation-specific antibody were used to detect the modification level after KAT2B knockdown in GSCs. The experiments were performed three times independently (**d-j**, **m-p**). Box plots show the median (centre), the 25th and 75th percentiles (bounds of box), and whiskers indicate the minimum and maximum values. Statistical significance was determined by a two-tailed Student's *t*-test.



**Extended Data Fig. 6 | Lactylation of KU70 K317 enhances the NHEJ function and maintains stemness of GSC. **a****, KU70 K317 lactylation and acetylation level detection after stimulated with different concentration of lactate. **b**, Representative pictures of comet assay under the stimulation of lactate combined transduced with shCONT, shKU70 and rescued using KU70 WT and KU70 K317R in GSCs. Scale bars, 100 $\mu$ m. **c**, Apoptosis assay under the stimulation of lactate combined transduced with shCONT, shKU70 and rescued using KU70

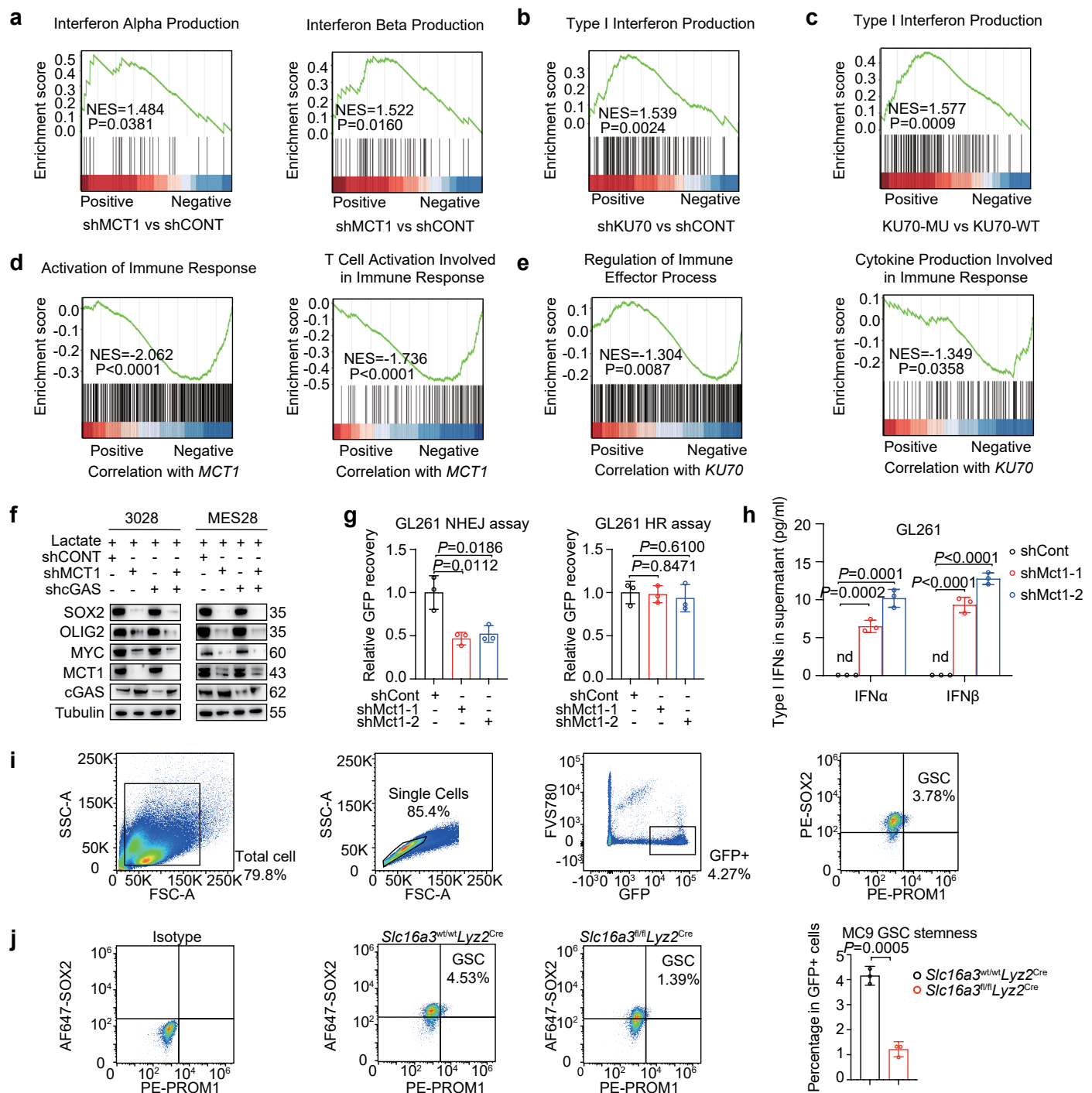
WT and KU70 K317R in GSCs. **d**, Immunoblot analysis under the stimulation of lactate combined transduced with shCONT, shKU70, or shKU70 rescued with KU70 WT or KU70 K317R. **e**, Senescence-associated  $\beta$ -galactosidase assay under the stimulation of lactate combined transduced with shCONT, shKU70 and rescued using KU70 WT and KU70 K317R in GSCs. The experiments were performed three times independently (**a**, **b**, **d**).



Extended Data Fig. 7 | See next page for caption.

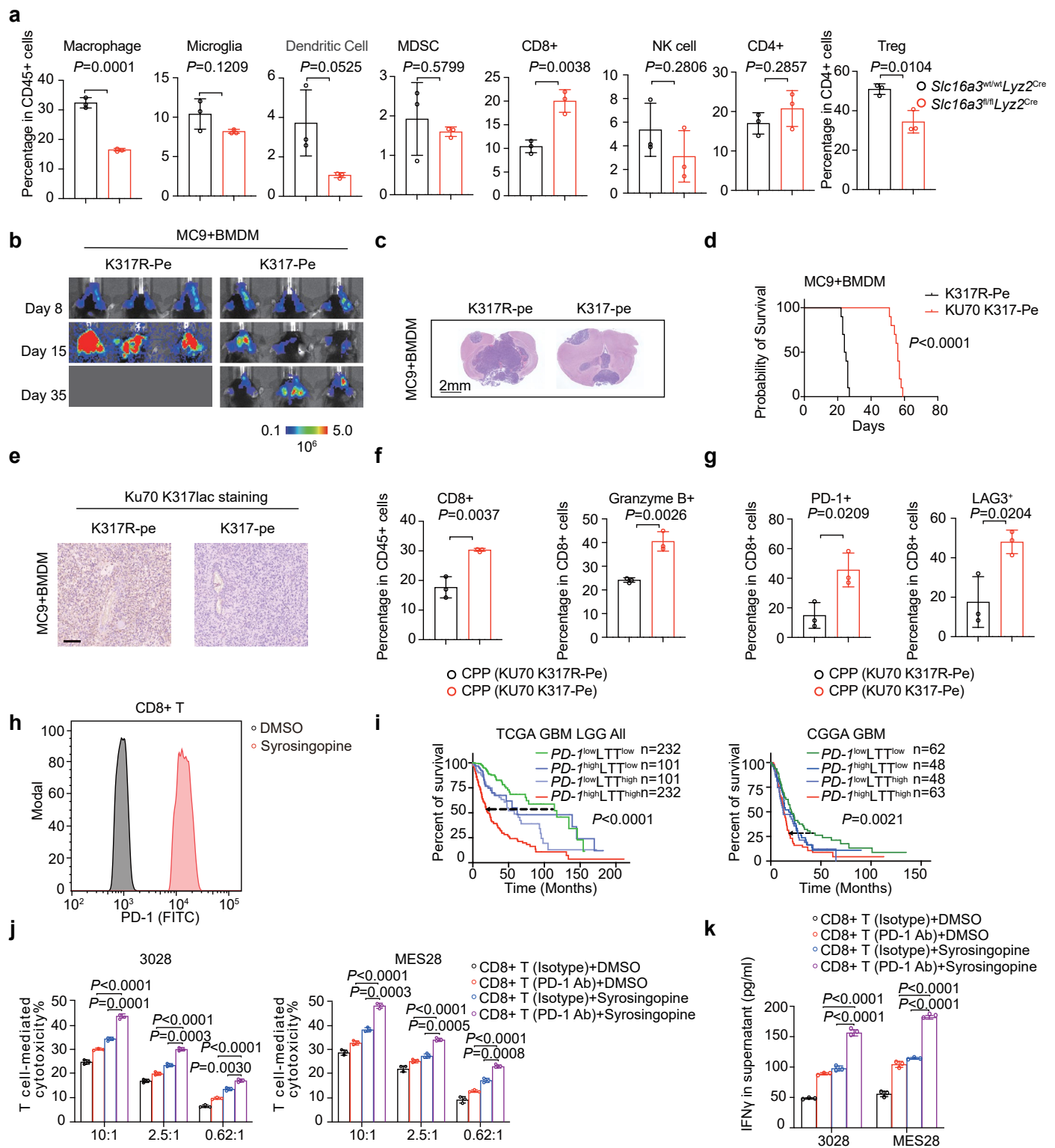
**Extended Data Fig. 7 | Lactylation of KU70 K317 enhances the NHEJ function and maintains stemness of GSC.** **a, b**, Two independent shRNAs targeting MCT1 decreased the self-renewal of GSCs compared with shCONT, as measured by sphere number quantification ( $n = 6$ ) (**a**) and the extreme limiting dilution assays (**b**) in 3O28 and MES28. **c, d**, Sphere number quantification ( $n = 6$ ) (**c**) and the extreme limiting dilution assays (**d**) performed in 3O28 and MES28 with the deletion of KU70 and rescued by KU70 WT and KU70 K317R. **e**, Cell viability of six patient-derived GSCs (MES28, 3O28, 2907, GSC23, RK1 and 3264) after 48 h treatment of vehicle control (DMSO) and various concentrations of NHEJ inhibitor NU7441 combined with the stimulation of lactate ( $n = 6$ ). **f**, GST pull-down assay performed to detect the interaction between KU80 and KU70 WT or KU70 K317R *in vitro*. **g**, Immunoblot results showing the interaction between KU70 and KU80 with anti-KU70 antibody in 3O28 and MES28 GSCs with or without P300-Flag (1287-1663AA) and the 10 mM lactate stimulated.

**h**, Immunoblot analysis of GSCs  $\gamma$ -H2AX level and the interaction level between KU70 and KU80 under the stimulation of 10 mM lactate combined transduced with shCONT, shKU70 and rescued by KU70 (WT) or KU70 (E330A) or KU70 (K317R) or KU70 (K317R E330A) after KU70 knockdown. **i**, Effects of shCONT, shKU70 and rescued by KU70 (WT) or KU70 (E330A) or KU70 (K317R) or KU70 (K317R E330A) after KU70 knockdown on the efficiency of NHEJ in MES28 GSC with the stimulation of lactate ( $n = 3$ ). **j**, Immunoblot analysis after KU70 K317-Peptide blockade in GSCs. The experiments were performed three times independently (**f, g, j**). Data are presented as mean  $\pm$  SD (**e, i**), box plots show the median (centre), the 25th and 75th percentiles (bounds of box), and whiskers indicate the minimum and maximum values (**a, c**). Statistical significance was determined by a two-tailed Student's *t*-test (**a, c, i**) and a likelihood ratio test (LRT) comparing the single-hit model to alternative models (two-sided). P-values were computed based on the  $\chi^2$  distribution of the likelihood ratio statistic (**b, d**).



**Extended Data Fig. 8 | Lactylation of KU70 K317 inhibits cGAS-STING signaling and maintains the immunosuppressive TME. a**, Gene Set Enrichment Analysis (GSEA) scores calculated for RNA sequencing data using Gene Ontology (GO) gene sets showing *MCT1* expression correlates with a transcriptional signature of Interferon Alpha production signaling (left) and Interferon Beta production signaling (right) in MES28 GSC. **b**, GSEA scores calculated for RNA sequencing using GO gene sets showing KU70 expression correlates with type I interferon production signaling in MES28 GSC. **c**, GSEA scores calculated for RNA sequencing using GO gene sets showing KU70 K317lac level correlates with type I interferon production signaling in MES28 GSC. **d, e**, GSEA using GO gene sets showing *MCT1* (**d**) and *KU70* (**e**) expression correlate with immune response

related signals in TCGA GBM dataset. **f**, Immunoblot analysis of stemness marker level of 3028 (left) and MES28 (right) after transduced with control shRNA, shcGAS and shMCT1 by stimulating with lactate. **g**, Diagram of the NHEJ and HR reporter assay. Effects of Mct1 knockdown on the efficiency of NHEJ and HR in mouse glioma cell line GL261 under the stimulation of lactate (n = 3). **h**, ELISA experiments detecting the levels of type I interferon (IFN $\alpha$  and IFN $\beta$ ) while GL261 expressing shCont and shMct1 (n = 3). **i**, The gating strategy of GSCs in flow cytometric analysis. **j**, Flow cytometry plots and quantification of Sox2+ Prom1+ GSCs in GFP+ cells as indicated (n = 3 biologically independent mice). Data are presented as mean  $\pm$  SD. Statistical significance was determined by a two-tailed Student's t-test.

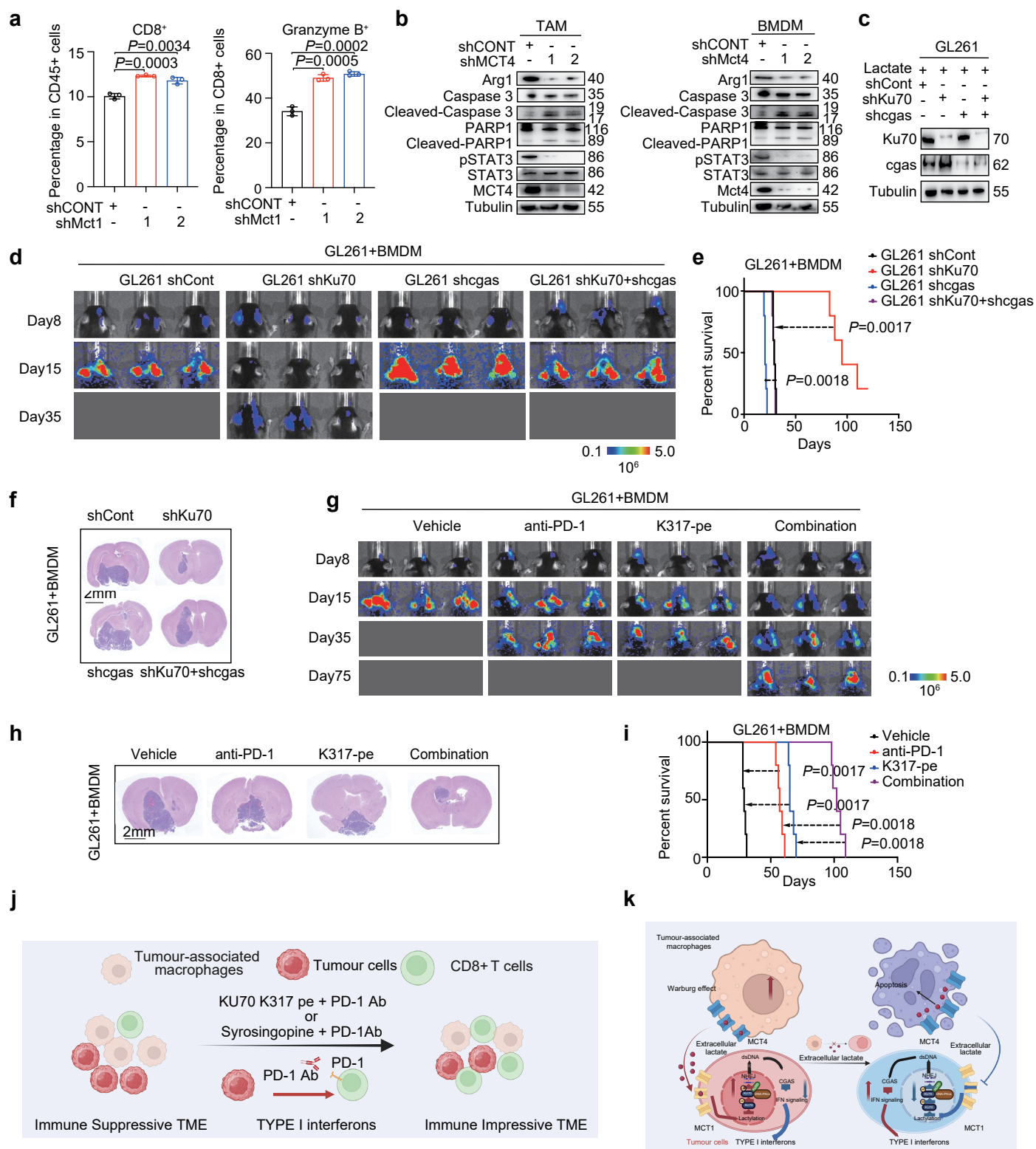


Extended Data Fig. 9 | See next page for caption.

**Extended Data Fig. 9 | Lactylation of KU70 K317 inhibits cGAS-STING**

**signaling and maintains the immunosuppressive TME. a**, Flow cytometry percentage of macrophage, microglia, MDSC, Dendritic cell, CD8 + T cell, NK cell and CD4 + T cell from CD45+ cells and Treg from CD4 + T cells in *Lyz2*-Cre with *Slc16a3*<sup>wt/wt</sup> and *Lyz2*-Cre with *Slc16a3*<sup>fl/fl</sup> C57BL/6 J mice groups bearing  $5 \times 10^4$  mouse glioma stem cell MC9 (n = 3 biologically independent mice). **b**, *In vivo* bioluminescent imaging of tumour growth was performed in immunocompetent mice bearing  $5 \times 10^4$  mouse glioma stem cell MC9 and  $5 \times 10^4$  BMDMs using KU70 K317-Peptide or KU70 K317R-Peptide on days 8, 15, 35. **c**, Representative images of hematoxylin and eosin staining of mouse brains collected on day 25 after transplantation of MC9 and BMDMs treated with KU70 K317-Peptide or KU70 K317R-Peptide. Scale bar, 2 mm. Each image is representative of at least three similar experiments. **d**, Kaplan-Meier survival curves of immunocompetent mice after being treated with KU70 K317-Peptide or KU70 K317R-Peptide (n = 10). **e**, Representative images showing immunohistochemically stained with KU70 K317lac in as indicated brain sections of the indicated mice on day 25 after

treated with KU70 K317-Peptide or KU70 K317R-Peptide. Scale bar, 50  $\mu$ m. **f**, Flow cytometry analysis of CD8 + T cells and granzyme B + CD8 + T cells in BMDMs and treated MC9-derived tumours at day 25 after injection (n = 3 biologically independent mice). **g**, Flow cytometry analysis of exhaustion markers in CD8 + T cells in BMDMs and treated MC9-derived tumours at day 25 after injection (n = 3 biologically independent mice). **h**, Expression of PD-1 on CD8 + T cells after the cytotoxic experiments with or without the syrosingopine treatment. **i**, Kaplan-Meier survival analysis of lactate transmembrane transport signature combined with *PD-1* expression level by the median of TCGA GBM LGG and CGGA GBM datasets. **j**, After co-cultured with the supernatant of PBMC-derived macrophages, cytotoxicity experiments of 3028 and MES28 GSCs with activated CD8 + T cells. The ratios between CD8 + T cells and GSCs are indicated (n = 3). **k**, ELISA experiments detecting the levels of IFN $\gamma$  in the supernatant of co-cultured system of activated T cells and GSCs (n = 3). Data are presented as mean  $\pm$  SD. Statistical significance was determined by a two-tailed Student's t-test (**a**, **f**, **g**, **j**, **k**) or two-tailed log-rank test (**d**, **i**).



Extended Data Fig. 10 | See next page for caption.

**Extended Data Fig. 10 | Inhibition of lactate transporters synergizes with immune checkpoint inhibitor to prolong survival in glioblastoma orthotopic xenograft models.** **a**, Flow cytometry analysis of CD8<sup>+</sup> T cells and granzyme B<sup>+</sup> CD8<sup>+</sup> T cells in BMDMs and treated GL261-derived tumours at day 25 after injection (n = 3 biologically independent mice). **b**, Immunoblot results show tumour-promoting macrophage markers and apoptosis markers after MCT4 knockdown in TAMs (left) and BMDMs (right). **c**, Immunoblot analysis showing the Ku70 and cgas level in GL261 after Ku70 and cgas knockdown. **d**, *In vivo* bioluminescent imaging of tumour growth was performed in C57BL/6J mice bearing  $5 \times 10^4$  BMDMs and  $5 \times 10^4$  GL261 transduced with shCont, shKu70, shcgas or combined with shKu70 and shcgas on days 8, 15, 35. **e**, Kaplan-Meier survival curves of immunocompetent mice bearing GL261 and BMDMs transduced with shCont, shKu70, shcgas or combined with shKu70 and shcgas derived intracranial tumours (n = 5). **f**, Representative images of hematoxylin and eosin staining of mouse brains collected on day 25 after transplantation of BMDMs and GL261 transduced with shCont, shKu70, shcgas or combined with shKu70 and shcgas. Scale bar, 2 mm. Each image is representative of at

least three similar experiments. **g**, *In vivo* bioluminescent imaging of tumour growth was performed in immunocompetent mice bearing GL261 and BMDMs using combination of the KU70 K317-Peptide and PD-1 antibody on days 8, 15, 35. **h**, Representative images of hematoxylin and eosin staining of mouse brains collected on day 25 after transplantation of GL261 and BMDMs treated with KU70 K317-Peptide and PD-1 antibody. Scale bar, 2 mm. Each image is representative of at least three similar experiments. **i**, Kaplan-Meier survival curves of immunocompetent mice after being treated with KU70 K317-Peptide and PD-1 antibody (n = 5). **j**, Schematic diagram illustrating that targeting lactate transporter MCT1 and MCT4 or KU70 K317 lactylation combined with anti-PD-1 remodels the immune suppressive microenvironment. **k**, Schematic diagram illustrating that TAMs-derived lactate remodels glioblastoma immune microenvironment through regulation of NHEJ repair by KU70 K317 lactylation. Data are presented as mean  $\pm$  SD. Statistical significance was determined by a two-tailed Student's t-test (**a**) or two-tailed log-rank test (**e**, **i**). Panels **j** and **k** created with [BioRender.com](https://www.biorender.com).

Reporting Summary

Nature Portfolio wishes to improve the reproducibility of the work that we publish. This form provides structure for consistency and transparency in reporting. For further information on Nature Portfolio policies, see our [Editorial Policies](#) and the [Editorial Policy Checklist](#).

Statistics

For all statistical analyses, confirm that the following items are present in the figure legend, table legend, main text, or Methods section.

- |                                     |  |
|-------------------------------------|--|
| n/a                                 | Confirmed  |
| <input type="checkbox"/>            | <input checked="" type="checkbox"/> The exact sample size ( <i>n</i> ) for each experimental group/condition, given as a discrete number and unit of measurement   |
| <input type="checkbox"/>            | <input checked="" type="checkbox"/> A statement on whether measurements were taken from distinct samples or whether the same sample was measured repeatedly  |
| <input type="checkbox"/>            | <input checked="" type="checkbox"/> The statistical test(s) used AND whether they are one- or two-sided<br><i>Only common tests should be described solely by name; describe more complex techniques in the Methods section.</i>   |
| <input checked="" type="checkbox"/> | <input type="checkbox"/> A description of all covariates tested  |
| <input type="checkbox"/>            | <input checked="" type="checkbox"/> A description of any assumptions or corrections, such as tests of normality and adjustment for multiple comparisons  |
| <input type="checkbox"/>            | <input checked="" type="checkbox"/> A full description of the statistical parameters including central tendency (e.g. means) or other basic estimates (e.g. regression coefficient) AND variation (e.g. standard deviation) or associated estimates of uncertainty (e.g. confidence intervals) |
| <input type="checkbox"/>            | <input checked="" type="checkbox"/> For null hypothesis testing, the test statistic (e.g. <i>F</i> , <i>t</i> , <i>r</i> ) with confidence intervals, effect sizes, degrees of freedom and <i>P</i> value noted<br><i>Give P values as exact values whenever suitable.</i>                     |
| <input checked="" type="checkbox"/> | <input type="checkbox"/> For Bayesian analysis, information on the choice of priors and Markov chain Monte Carlo settings  |
| <input checked="" type="checkbox"/> | <input type="checkbox"/> For hierarchical and complex designs, identification of the appropriate level for tests and full reporting of outcomes  |
| <input type="checkbox"/>            | <input checked="" type="checkbox"/> Estimates of effect sizes (e.g. Cohen's <i>d</i> , Pearson's <i>r</i> ), indicating how they were calculated   |

Our web collection on [statistics for biologists](#) contains articles on many of the points above.

Software and code

Policy information about [availability of computer code](#)

Data collection	RNA-seq data were obtained using MGISEQ-2000 platform (BGI), Mass spectrometry data were obtained using timsTOF Pro (Bruker), Western blot images were acquired using Tanon5200S (Tanon), Immunofluorescence images were acquired using LSM710 (Zeiss), The tumor luciferase images were captured by using IVIS imaging system (Spectrum CT; PerkinElmer), Flow Cytometry data were acquired using FACSymphony A5 SORP (BD Biosciences). Metabolites were analysed on a Jasper HPLC coupled to Sciex 4500 MD system (GENETECH SCIENTIFIC).
Data analysis	R (version 4.1.3), Seurat (version 4.3.0), Cell Ranger (version 6.1.2), SPATA2 (version 0.1.0), Trim Galore (version 0.6.7), Salmon (version 1.10.1), DoubletFinder (version 2.0.4), Harmony (version 1.2.0), AUCell (version 1.24.0), Tximport (version 1.8.0), Macs2 (version 2.1.0), ImageJ (version 1.53k), Cytoscape (version 3.9.0), ClueGO (version 2.5.9), SynergyFinder (version 3.0), OlyVIA (version 4.1.1), FlowJo (version 10.10.0), GraphPad Prism (version 9.2.0)

For manuscripts utilizing custom algorithms or software that are central to the research but not yet described in published literature, software must be made available to editors and reviewers. We strongly encourage code deposition in a community repository (e.g. GitHub). See the Nature Portfolio [guidelines for submitting code & software](#) for further information.

## Data

Policy information about [availability of data](#)

All manuscripts must include a [data availability statement](#). This statement should provide the following information, where applicable:

- Accession codes, unique identifiers, or web links for publicly available datasets
- A description of any restrictions on data availability
- For clinical datasets or third party data, please ensure that the statement adheres to our [policy](#)

GBM scRNA-seq dataset 1: HRA004899 (Shared URL: <https://ngdc.cncb.ac.cn/gsa-human/s/Z2H45inx>);

GBM scRNA-seq dataset 2: GSE182109 (Shared URL: <https://www.ncbi.nlm.nih.gov/geo/query/acc.cgi?acc=GSE182109>);

GBM scRNA-seq dataset 3: GSE256490 (Shared URL: <https://www.ncbi.nlm.nih.gov/geo/query/acc.cgi?acc=GSE256490>);

GBM stRNA-seq data: (Shared URL: <https://datadryad.org/stash/dataset/doi:10.5061/dryad.h70rxwdmj/>);

For RNA-seq results, the results of MCT1 knockdown, KU70 knockdown and KU70 rescue GSE266884 (Shared URL: <https://www.ncbi.nlm.nih.gov/geo/query/acc.cgi?acc=GSE266884>).

Mass spectrometry data have been deposited in ProteomeXchange with the primary accession code PXD069969 (<https://proteomecentral.proteomexchange.org/cgi/GetDataset?ID=PXD069969>) and PXD070007 (<https://proteomecentral.proteomexchange.org/cgi/GetDataset?ID=PXD070007>).

## Research involving human participants, their data, or biological material

Policy information about studies with [human participants or human data](#). See also policy information about [sex, gender \(identity/presentation\)](#), [and sexual orientation](#) and [race, ethnicity and racism](#).

Reporting on sex and gender	Sex and gender were identified as insignificant factor in prognosis analysis.
Reporting on race, ethnicity, or other socially relevant groupings	There was no bias of recruitment in terms of race, ethnicity, or other socially relevant.
Population characteristics	GBM surgical specimens from 4 males and 2 female were used for immunofluorescence staining and TAMs cell sorting. All participants provided written informed consent prior to inclusion in the study. No financial or material compensation was provided to participants. GAM_1: male, 69 years old, IDH wt. GAM_2: female, 72 years old, IDH wt. GAM_3: male, 75 years old, IDH wt. GBM_4: female, 77 years old, IDH wt. GBM_5: male, 71 years old, IDH wt. GBM_6: male, 56 years old, IDH wt.
Recruitment	None selection had been made. Recruitment and collection of human samples adhered to approved IRB protocols.
Ethics oversight	All patient studies were conducted in accordance with the Declaration of Helsinki. Patient-derived cell models: GBM tissues were obtained from excess surgical resection samples from patients at the Case Western Reserve University (Cleveland, OH) after review by neuropathology with appropriate consent and in accordance with an Institutional Review Board-approved protocol (090401), some of the cell models were provided as generous gifts by Dr. Erik Sulman (Duke Health) and transferred via a material transfer agreement from MD Anderson Cancer Center. GBM tissue samples: The study was approved by the Ethical Committee of the First Affiliated Hospital of Nanjing Medical University (2021-SR-076) and complied with all relevant ethical regulations regarding human participants.

Note that full information on the approval of the study protocol must also be provided in the manuscript.

## Field-specific reporting

Please select the one below that is the best fit for your research. If you are not sure, read the appropriate sections before making your selection.

☒ Life sciences ☐ Behavioural & social sciences ☐ Ecological, evolutionary & environmental sciences

For a reference copy of the document with all sections, see [nature.com/documents/nr-reporting-summary-flat.pdf](https://www.nature.com/documents/nr-reporting-summary-flat.pdf)

## Life sciences study design

All studies must disclose on these points even when the disclosure is negative.

Sample size	No statistical methods were used to pre-determine sample sizes but our sample sizes are similar to those reported in previous publications (PMID: 34615656, Cancer Discovery, 2022; PMID: 37198486, Nature, 2023). Group sizes for in vivo experiments were selected empirically based upon prior knowledge of the intragroup variation of tumor growth and drug treatment, in which group sizes of 5-10 mice/genotype or treatment are sufficient. Similarly, group sizes for in vitro experiments were selected on the basis of prior knowledge of variation. These sample sizes are sufficient to allow for the determination of statistical significance between groups and minimize the number of animals and replicates needed for each experiment.
-------------	---

Data exclusions	No data were excluded from the analyses.
Replication	Replicates were used in all experiments as indicated in text, figure legends and methods. Animal experiments have been repeated as indicated in the figure legends.
Randomization	All mice were randomized to in vivo treatment. For experiments not involving mice, cells were randomized into experimental groups.
Blinding	Mice were randomly selected for intracranial injection. Blinding was not done due to the requirements for case labeling and staffing needs, as knowledge of the grouping information was essential for the staff to conduct the studies.

## Reporting for specific materials, systems and methods

We require information from authors about some types of materials, experimental systems and methods used in many studies. Here, indicate whether each material, system or method listed is relevant to your study. If you are not sure if a list item applies to your research, read the appropriate section before selecting a response.

### Materials & experimental systems

n/a	Involved in the study
<input type="checkbox"/>	<input checked="" type="checkbox"/> Antibodies
<input type="checkbox"/>	<input checked="" type="checkbox"/> Eukaryotic cell lines
<input checked="" type="checkbox"/>	<input type="checkbox"/> Palaeontology and archaeology
<input type="checkbox"/>	<input checked="" type="checkbox"/> Animals and other organisms
<input checked="" type="checkbox"/>	<input type="checkbox"/> Clinical data
<input checked="" type="checkbox"/>	<input type="checkbox"/> Dual use research of concern
<input checked="" type="checkbox"/>	<input type="checkbox"/> Plants

### Methods

n/a	Involved in the study
<input checked="" type="checkbox"/>	<input type="checkbox"/> ChIP-seq
<input type="checkbox"/>	<input checked="" type="checkbox"/> Flow cytometry
<input checked="" type="checkbox"/>	<input type="checkbox"/> MRI-based neuroimaging

## Antibodies

### Antibodies used

The following antibodies were used for western blot in this study: anti-Tubulin (Abcepta, AM1031a, 1:5000), anti-MCT4 (Proteintech, 22787-1-AP, 1:1000), anti-MCT1 (ABclonal, A3013, 1:1000), anti-L-Lactyl Lysine (Ptm-biolab, PTM-1401, 1:1000), anti-Acetyllysine (Ptm-biolab, PTM-105RM, 1:1000), anti-KU70-K317a (Ptm-biolab, customized, 1:1000), anti-KU70-K317ac (Ptm-biolab, customized, 1:1000), anti-SOX2 (Cell Signaling Technology, 3579, 1:1000), anti-OLIG2 (Sigma-Aldrich, MABN50, 1:1000), anti-MYC (Cell Signaling Technology, 18583, 1:1000), anti-KU70 (Proteintech, 10723-1-AP, 1:1000), anti-CD133 (Cell Signaling Technology, 48082, 1:1000), anti-GFAP (Cell Signaling Technology, 12389, 1:1000), anti-His Tag (Cell Signaling Technology, 12698, 1:1000), anti-HA Tag (Cell Signaling Technology, 3724, 1:1000), anti-Phospho-Histone H2A.X (Cell Signaling Technology, 80312, 1:1000), anti-Flag Tag (Cell Signaling Technology, 14793, 1:1000), anti-KU80 (Proteintech, 16389-1-AP, 1:1000), anti-DNA-PKcs (Proteintech, 19983-1-AP, 1:1000), anti-GST Tag (Cell Signaling Technology, 2625, 1:1000), anti-cGAS (Cell Signaling Technology, 79978, 1:1000), anti-cGAS (Cell Signaling Technology, 31659, 1:1000), anti-Phospho-STING (Ser366) (Cell Signaling Technology, 19781, 1:1000), anti-Phospho-STING (Ser365) (Cell Signaling Technology, 72971, 1:1000), anti-STING (Cell Signaling Technology, 13647, 1:1000), anti-Phospho-TBK1/NAK (Ser172) (Cell Signaling Technology, 5483, 1:1000), anti-TBK1/NAK (Cell Signaling Technology, 3504, 1:1000), anti-Phospho-IRF-3 (Ser396) (Cell Signaling Technology, 4947, 1:1000), anti-IRF3 (Proteintech, 66670-1-Ig, 1:1000), anti-Arginase-1 (Proteintech, 16001-1-AP, 1:1000), anti-Phospho-Stat3 (Tyr705) (Cell Signaling Technology, 9145, 1:1000), anti-PARP (Cell Signaling Technology, 9542, 1:1000), anti-Caspase-3 (Cell Signaling Technology, 9662, 1:1000), anti-Stat3 (Cell Signaling Technology, 9139, 1:1000), anti-P300 (Cell Signaling Technology, 86377, 1:1000), anti-CBP (Cell Signaling Technology, 7389, 1:1000), anti-PCAF (Cell Signaling Technology, 3378, 1:1000), anti-FEN1 (Cell Signaling Technology, 2746, 1:1000), anti-LRIG1 (Cell Signaling Technology, 59027, 1:1000), anti-IQGAP3 (Proteintech, 25930-1-AP, 1:1000), anti-Phospho-ATM (Ser1981) (Cell Signaling Technology, 5883, 1:1000), anti-ATM (Cell Signaling Technology, 2873, 1:1000), anti-Phospho-p53 (Ser15) (Cell Signaling Technology, 9284, 1:1000), anti-p53 (Cell Signaling Technology, 9282, 1:1000), anti-p21 Waf1/Cip1 (Cell Signaling Technology, 2947, 1:1000) and anti-GPR81 (Proteintech, 20146-1-AP, 1:1000).

The following primary antibodies were used for immunofluorescent staining in this study: anti-MCT4 (Santa Cruz, sc-376465, 1:100), anti-MCT1 (ABclonal, A3013, 1:100), anti-SOX2 (R&D Systems, AF2018, 1:100), anti-CD163 (Proteintech, 16646-1-AP, 1:1000), anti-KU70 (Proteintech, 10723-1-AP, 1:100), anti-Phospho-Histone H2A.X (Cell Signaling Technology, 80312, 1:100), anti-cGAS (Cell Signaling Technology, 79978, 1:100), anti-dsDNA (Abcam, ab27156, 1:100), anti-CD8 (Abcam, ab217344, 1:100), anti-Iba1 (Santa Cruz, sc-32725, 1:100).

This study used the following antibodies for immunoprecipitation: anti-KU70 (Proteintech, 10723-1-AP, 1:100), anti-IQGAP3 (Proteintech, 25930-1-AP, 1:100), anti-HA Tag (Cell Signaling Technology, 3724, 1:100), anti-Flag Tag (Cell Signaling Technology, 14793, 1:100), anti-GST Tag (Cell Signaling Technology, 2625, 1:100).

For isolation of TAMs from GBMs by flow cytometry, the following antibodies were used, APC-conjugated Rat anti-human CD11b (BD Pharmingen, 553312, 1:100) and PE-conjugated Mouse anti-human CD163 (BD Pharmingen, 556018, 1:100).

For flow cytometry experiments, the following antibodies were used, anti-CD133-PE (BioLegend, 141203, 1:100), anti-SOX2-PE (BioLegend, 656103, 1:100), anti-CD45-BV421 (BD Horizon, 567799, 1:100), anti-CD11b-APC (BD Pharmingen, 561690, 1:100), anti-Ly-6G and LY-6C-FITC (BD Pharmingen, 553126, 1:100), anti-F4/80-Pe Cy5.5 (BioLegend, 123127, 1:100), anti-CD11c-Pe Cy7 (BD Pharmingen, 561022, 1:100), anti-MHC-II-PE (BioLegend, 107607, 1:100), anti-NK-1.1-BV605 (BD Horizon, 563220, 1:100), anti-CD3-FITC (BD Pharmingen, 561827, 1:100), anti-CD4-BV650 (BD Horizon, 563232, 1:100), anti-CD8-Pe Cy7 (BD Pharmingen, 561097,

1:100), anti-CD8-BUV395 (BD Horizon, 563786, 1:100), anti-CD8-FITC (BD Pharmingen, 561966, 1:100), anti-CD25-PE (BD Pharmingen, 558642, 1:100), anti-Foxp3-APC (eBioscience, 17-5773-82, 1:100), anti-granzyme B-Pe Cy7 (BioLegend, 372213, 1:100), anti-CD279-APC (BD Pharmingen, 562671, 1:100), anti-CD279-FITC (BD Pharmingen, 561035, 1:100), anti-LAG3-PE (BD Pharmingen, 552380, 1:100) and anti-SOX2-AF647 (BD Pharmingen, 560294, 1:100).

## Validation

anti-Tubulin (Abcepta, AM1031a); Suitable for: WB; Reacts with Human, Mouse  
<https://www.abcepta.com/products/AM1031a-TBB5-Antibody>  
 anti-MCT4 (Proteintech, 22787-1-AP); Suitable for: WB, IHC, IF/ICC, FC (INTRA); Reacts with Human, Mouse, Rat  
<https://www.ptglab.com/products/SLC16A3-Antibody-22787-1-AP.htm>  
 anti-MCT1 (Abclonal, A3013); Suitable for: WB, IP, IF; Reacts with Human, Mouse, Rat  
<https://abclonal.com/catalog-antibodies/MCT1SLC16A1RabbitAb/A3013>  
 anti-L-Lactyl Lysine (Ptm-biolab, PTM-1401); Suitable for: WB, FC; Reacts with All  
<https://www.ptmbio.com/products/anti-l-lactyllysine-rabbit-pab/PTM-1401.htm>  
 anti-Acetyllysine (Ptm-biolab, PTM-105RM); Suitable for: WB, IHC-P; Reacts with All  
<https://www.ptmbio.com/products/anti-acetyllysine-rabbit-mab/PTM-105RM.htm>  
 anti-KU70-K317la (Ptm-biolab, customized); Suitable for: WB, IHC; Reacts with Human, Mouse  
 anti-KU70-K317ac (Ptm-biolab, customized); Suitable for: WB, IHC; Reacts with Human, Mouse  
 anti-SOX2 (Cell Signaling Technology, 3579); Suitable for: WB, IF, FC; Reacts with Human  
<https://www.cellsignal.com/products/primary-antibodies/sox2-d6d9-xp-rabbit-mab/3579>  
 anti-OLIG2 (Sigma-Aldrich, MABN50); Suitable for: WB, IP, IHC, ICC; Reacts with Human, Mouse  
<https://www.sigmaaldrich.com/US/en/search/mabn50?dym=mab858%2Cmab350%2Cmabn10%2Cmab1501&focus=products&page=1&perpage=30&sort=relevance&term=MABN50&type=product>  
 anti-MYC (Cell Signaling Technology, 185830); Suitable for: WB, IP, IF, F, ChIP; Reacts with Human, Mouse, Rat  
<https://www.cellsignal.com/products/primary-antibodies/c-myc-e5q6w-rabbit-mab/18583>  
 anti-KU70 (Proteintech, 10723-1-AP); Suitable for: WB, IHC, IF/ICC, FC (INTRA), IP, CoIP, RIP, ELISA; Reacts with Human, Mouse, Rat  
<https://www.ptglab.com/products/KU70,XRCC6-Antibody-10723-1-AP.htm>  
 anti-CD133 (Cell Signaling Technology, 48082); Suitable for: WB; Reacts with Mouse  
<https://www.cellsignal.com/products/primary-antibodies/cd133-e5e2h-rabbit-mab/48082>  
 anti-GFAP (Cell Signaling Technology, 12389); Suitable for: WB, IF; Reacts with Human, Mouse, Rat  
<https://www.cellsignal.com/products/primary-antibodies/gfap-d1f4q-xp-rabbit-mab/12389>  
 anti-His Tag (Cell Signaling Technology, 12698); Suitable for: WB, IP, IF, FC, CoIP; Reacts with All  
<https://www.cellsignal.com/products/primary-antibodies/his-tag-d310-xp-rabbit-mab/12698>  
 anti-HA Tag (Cell Signaling Technology, 3724); Suitable for: WB, IP, IHC, IF, F, ChIP; Reacts with All  
<https://www.cellsignal.com/products/primary-antibodies/ha-tag-c29f4-rabbit-mab/3724>  
 anti-Phospho-Histone H2A.X (Cell Signaling Technology, 80312); Suitable for: WB, IHC, IF, F; Reacts with Human, Mouse, Rat, Monkey  
<https://www.cellsignal.com/products/primary-antibodies/phospho-histone-h2a-x-ser139-d7t2v-mouse-mab/80312>  
 anti-Flag Tag (Cell Signaling Technology, 14793); Suitable for: WB, IP, IHC, IF, F, ChIP; Reacts with All  
<https://www.cellsignal.com/products/primary-antibodies/dykdddk-tag-d6w5b-rabbit-mab-binds-to-same-epitope-as-sigma-aldrich-anti-flag-m2-antibody/14793>  
 anti-KU80 (Proteintech, 16389-1-AP); Suitable for: WB, IP, IHC, IF/ICC; Reacts with Human, Mouse, Pig  
<https://www.ptglab.com/products/XRCC5-Antibody-16389-1-AP.htm>  
 anti-DNA-PKcs (Proteintech, 19983-1-AP); Suitable for: WB, IP; Reacts with Human, Mouse, Rat  
<https://www.ptglab.com/products/PRKDC-Antibody-19983-1-AP.htm>  
 anti-GST Tag (Cell Signaling Technology, 2625); Suitable for: WB, IP; Reacts with All  
<https://www.cellsignal.com/products/primary-antibodies/gst-tag-91g1-rabbit-mab/2625>  
 anti-cGAS (Cell Signaling Technology, 79978); Suitable for: WB, IHC, IF, F; Reacts with Human  
<https://www.cellsignal.com/products/primary-antibodies/cgas-e5v3w-rabbit-mab/79978>  
 anti-cGAS (Cell Signaling Technology, 31659); Suitable for: WB, IP; Reacts with Mouse  
<https://www.cellsignal.com/products/primary-antibodies/cgas-d3o8o-rabbit-mab/31659>  
 anti-Phospho-STING (Ser366) (Cell Signaling Technology, 19781); Suitable for: WB; Reacts with Human  
<https://www.cellsignal.com/products/primary-antibodies/phospho-sting-ser366-d7c3s-rabbit-mab/19781>  
 anti-Phospho-STING (Ser365) (Cell Signaling Technology, 72971); Suitable for: WB; Reacts with Mouse  
<https://www.cellsignal.com/products/primary-antibodies/phospho-sting-ser365-d8f4w-rabbit-mab/72971>  
 anti-STING (Cell Signaling Technology, 13647); Suitable for: WB, IP, IHC; Reacts with Human, Mouse  
<https://www.cellsignal.com/products/primary-antibodies/sting-d2p2f-rabbit-mab/13647>  
 anti-Phospho-TBK1/NAK (Ser172) (Cell Signaling Technology, 5483); Suitable for: WB, IP, IF, F; Reacts with Human, Mouse, Rat  
<https://www.cellsignal.com/products/primary-antibodies/phospho-tbk1-nak-ser172-d52c2-xp-rabbit-mab/5483>  
 anti-TBK1/NAK (Cell Signaling Technology, 3504); Suitable for: WB, IP; Reacts with Human, Mouse, Rat  
<https://www.cellsignal.com/products/primary-antibodies/tbk1-nak-d1b4-rabbit-mab/3504>  
 anti-Phospho-IRF-3 (Ser396) (Cell Signaling Technology, 4947); Suitable for: WB; Reacts with Human, Mouse  
<https://www.cellsignal.com/products/primary-antibodies/phospho-irf-3-ser396-4d4g-rabbit-mab/4947>  
 anti-IRF3 (Proteintech, 66670-1-Ig); Suitable for: WB, IHC; Reacts with Human, Mouse  
<https://www.ptglab.com/products/IRF3-Antibody-66670-1-Ig.htm>  
 anti-Arginase-1 (Proteintech, 16001-1-AP); Suitable for: WB, IP, IHC, IF/ICC; Reacts with Human, Mouse, Rat  
<https://www.ptglab.com/products/ARG1-Antibody-16001-1-AP.htm>  
 anti-Phospho-Stat3 (Tyr705) (Cell Signaling Technology, 9145); Suitable for: WB, IP, IHC, IF, F, ChIP; Reacts with Human, Mouse, Rat, Monkey  
<https://www.cellsignal.com/products/primary-antibodies/phospho-stat3-tyr705-d3a7-xp-rabbit-mab/9145>  
 anti-PARP (Cell Signaling Technology, 9542); Suitable for: WB; Reacts with Human, Mouse, Rat, Monkey  
<https://www.cellsignal.com/products/primary-antibodies/parp-antibody/9542>  
 anti-Caspase-3 (Cell Signaling Technology, 9662); Suitable for: WB, IP, IHC; Reacts with Human, Mouse, Rat, Monkey  
<https://www.cellsignal.com/products/primary-antibodies/caspase-3-antibody/9662>  
 anti-Stat3 (Cell Signaling Technology, 9139); Suitable for: WB, IP, IHC, IF, F, ChIP; Reacts with Human, Mouse, Rat, Monkey  
<https://www.cellsignal.com/products/primary-antibodies/stat3-124h6-mouse-mab/9139>

anti-P300 (Cell Signaling Technology, 86377); Suitable for: WB, IP, IHC, IF; Reacts with Human, Monkey  
<https://www.cellsignal.com/products/primary-antibodies/p300-d8z4e-rabbit-mab/86377>

anti-CBP (Cell Signaling Technology, 7389); Suitable for: WB, IP, IHC, IF, ChIP; Reacts with Human, Mouse, Rat, Monkey  
<https://www.cellsignal.com/products/primary-antibodies/cbp-d6c5-rabbit-mab/7389>

anti-PCAF (Cell Signaling Technology, 3378); Suitable for: WB, IP, ChIP; Reacts with Human, Mouse, Rat, Monkey  
<https://www.cellsignal.com/products/primary-antibodies/pcaf-c14g9-rabbit-mab/3378>

anti-FEN1 (Cell Signaling Technology, 2746); Suitable for: WB; Reacts with Human, Mouse, Rat, Monkey  
<https://www.cellsignal.com/products/primary-antibodies/fen-1-antibody/2746>

anti-LRIG1 (Cell Signaling Technology, 59027); Suitable for: WB, IP; Reacts with Human  
<https://www.cellsignal.com/products/primary-antibodies/lrig1-e1u2b-rabbit-mab/59027>

anti-IQGAP3 (Proteintech, 25930-1-AP); Suitable for: WB, IHC; Reacts with Human  
<https://www.ptglab.com/products/IQGAP3-Antibody-25930-1-AP.htm>

anti-Phospho-ATM (Ser1981) (Cell Signaling Technology, 5883); Suitable for: WB; Reacts with Human  
<https://www.cellsignal.com/products/primary-antibodies/phospho-atm-ser1981-d6h9-rabbit-mab/5883>

anti-ATM (Cell Signaling Technology, 2873); Suitable for: WB; Reacts with Human, Mouse  
<https://www.cellsignal.com/products/primary-antibodies/atm-d2e2-rabbit-mab/2873>

anti-Phospho-p53 (Ser15) (Cell Signaling Technology, 9284); Suitable for: WB, IP, ChIP; Reacts with Human, Mouse, Rat, Monkey  
<https://www.cellsignal.com/products/primary-antibodies/phospho-p53-ser15-antibody/9284>

anti-p53 (Cell Signaling Technology, 9282); Suitable for: WB, IP, ChIP; Reacts with Human, Monkey  
<https://www.cellsignal.com/products/primary-antibodies/p53-antibody/9282>

anti-p21 Waf1/Cip1 (Cell Signaling Technology, 2947); Suitable for: WB, IP, IHC, IF, F; Reacts with Human, Monkey  
<https://www.cellsignal.com/products/primary-antibodies/p21-waf1-cip1-12d1-rabbit-mab/2947>

anti-GPR81 (Proteintech, 20146-1-AP); Suitable for: WB, IHC; Reacts with Human, Mouse  
<https://www.ptglab.com/products/GPR81-Antibody-20146-1-AP.htm>

anti-CD163 (Proteintech, 16646-1-AP); Suitable for: WB, IP, IHC, IF-P; Reacts with Human, Pig  
<https://www.ptglab.com/products/CD163-Antibody-16646-1-AP.htm>

anti-dsDNA (Abcam, ab27156); Suitable for: IF, IHC-P; Reacts with Human, Mouse  
<https://www.abcam.com/en-us/products/primary-antibodies/ds-dna-antibody-35i9-dna-bsa-and-azide-free-ab27156>

anti-CD8 (Abcam, ab217344); Suitable for: WB, FC, IF, IP; Reacts with Mouse  
<https://www.abcam.com/en-us/products/primary-antibodies/cd8-alpha-antibody-epr21769-ab217344>

anti-Iba1 (Santa Cruz, sc-32725); Suitable for: WB, IP, IF, IHC; Reacts with Human, Mouse, Rat  
<https://www.scbt.com/p/iba1-antibody-1022-5>

APC-conjugated Rat anti-human CD11b (BD Pharmingen, 553312); Suitable for: FC; Reacts with Human, Mouse  
[https://www.bdbiosciences.com/en-us/products/reagents/flow-cytometry-reagents/research-reagents/single-color-antibodies-ruo/apc-rat-anti-cd11b.553312?tab=product\\_details](https://www.bdbiosciences.com/en-us/products/reagents/flow-cytometry-reagents/research-reagents/single-color-antibodies-ruo/apc-rat-anti-cd11b.553312?tab=product_details)

PE-conjugated Mouse anti-human CD163 (BD Pharmingen, 556018); Suitable for: FC; Reacts with Human  
[https://www.bdbiosciences.com/en-us/products/reagents/flow-cytometry-reagents/research-reagents/single-color-antibodies-ruo/pe-mouse-anti-human-cd163.556018?tab=product\\_details](https://www.bdbiosciences.com/en-us/products/reagents/flow-cytometry-reagents/research-reagents/single-color-antibodies-ruo/pe-mouse-anti-human-cd163.556018?tab=product_details)

anti-CD133-PE (BioLegend, 141203); Suitable for: FC; Reacts with Mouse  
<https://www.biolegend.com/ja-jp/products/pe-anti-mouse-cd133-antibody-7066>

anti-SOX2-PE (BioLegend, 656103); Suitable for: FC; Reacts with Human, Mouse  
<https://www.biolegend.com/ja-jp/products/pe-anti-sox2-antibody-9090>

anti-CD45-BV421 (BD Horizon, 567799); Suitable for: FC; Reacts with Mouse  
[https://www.bdbiosciences.com/en-us/products/reagents/flow-cytometry-reagents/research-reagents/single-color-antibodies-ruo/bv421-rat-anti-mouse-cd45.567799?tab=product\\_details](https://www.bdbiosciences.com/en-us/products/reagents/flow-cytometry-reagents/research-reagents/single-color-antibodies-ruo/bv421-rat-anti-mouse-cd45.567799?tab=product_details)

anti-CD11b-APC (BD Pharmingen, 561690); Suitable for: FC; Reacts with Human, Mouse  
[https://www.bdbiosciences.com/en-us/products/reagents/flow-cytometry-reagents/research-reagents/single-color-antibodies-ruo/apc-rat-anti-cd11b.561690?tab=product\\_details](https://www.bdbiosciences.com/en-us/products/reagents/flow-cytometry-reagents/research-reagents/single-color-antibodies-ruo/apc-rat-anti-cd11b.561690?tab=product_details)

anti-Ly-6G and LY-6C-FITC (BD Pharmingen, 553126); Suitable for: FC; Reacts with Mouse  
[https://www.bdbiosciences.com/en-us/products/reagents/flow-cytometry-reagents/research-reagents/single-color-antibodies-ruo/fetc-rat-anti-mouse-ly-6g-and-ly-6c.553126?tab=product\\_details](https://www.bdbiosciences.com/en-us/products/reagents/flow-cytometry-reagents/research-reagents/single-color-antibodies-ruo/fetc-rat-anti-mouse-ly-6g-and-ly-6c.553126?tab=product_details)

anti-F4/80-Pe Cy5.5 (BioLegend, 123127); Suitable for: FC; Reacts with Mouse  
<https://www.biolegend.com/ja-jp/products/percp-cyanine5-5-anti-mouse-f480-antibody-4303>

anti-CD11c-Pe Cy7 (BD Pharmingen, 561022); Suitable for: FC; Reacts with Mouse  
[https://www.bdbiosciences.com/en-us/products/reagents/flow-cytometry-reagents/research-reagents/single-color-antibodies-ruo/pe-cy-7-hamster-anti-mouse-cd11c.561022?tab=product\\_details](https://www.bdbiosciences.com/en-us/products/reagents/flow-cytometry-reagents/research-reagents/single-color-antibodies-ruo/pe-cy-7-hamster-anti-mouse-cd11c.561022?tab=product_details)

anti-MHC-II-PE (BioLegend, 107607); Suitable for: FC; Reacts with Mouse  
<https://www.biolegend.com/ja-jp/products/pe-anti-mouse-i-a-i-e-antibody-367>

anti-NK-1.1-BV605 (BD Horizon, 563220); Suitable for: FC; Reacts with Mouse  
[https://www.bdbiosciences.com/en-us/products/reagents/flow-cytometry-reagents/research-reagents/single-color-antibodies-ruo/bv605-mouse-anti-mouse-nk-1-1.563220?tab=product\\_details](https://www.bdbiosciences.com/en-us/products/reagents/flow-cytometry-reagents/research-reagents/single-color-antibodies-ruo/bv605-mouse-anti-mouse-nk-1-1.563220?tab=product_details)

anti-CD3-FITC (BD Pharmingen, 561827); Suitable for: FC; Reacts with Mouse  
[https://www.bdbiosciences.com/en-us/products/reagents/flow-cytometry-reagents/research-reagents/single-color-antibodies-ruo/fetc-hamster-anti-mouse-cd3e.561827?tab=product\\_details](https://www.bdbiosciences.com/en-us/products/reagents/flow-cytometry-reagents/research-reagents/single-color-antibodies-ruo/fetc-hamster-anti-mouse-cd3e.561827?tab=product_details)

anti-CD4-BV650 (BD Horizon, 563232); Suitable for: FC; Reacts with Mouse  
[https://www.bdbiosciences.com/en-us/products/reagents/flow-cytometry-reagents/research-reagents/single-color-antibodies-ruo/bv650-rat-anti-mouse-cd4.563232?tab=product\\_details](https://www.bdbiosciences.com/en-us/products/reagents/flow-cytometry-reagents/research-reagents/single-color-antibodies-ruo/bv650-rat-anti-mouse-cd4.563232?tab=product_details)

anti-CD8-Pe Cy7 (BD Pharmingen, 561097); Suitable for: FC; Reacts with Mouse  
[https://www.bdbiosciences.com/en-us/products/reagents/flow-cytometry-reagents/research-reagents/single-color-antibodies-ruo/pe-cy-7-rat-anti-mouse-cd8a.561097?tab=product\\_details](https://www.bdbiosciences.com/en-us/products/reagents/flow-cytometry-reagents/research-reagents/single-color-antibodies-ruo/pe-cy-7-rat-anti-mouse-cd8a.561097?tab=product_details)

anti-CD8-BUV395 (BD Horizon, 563786); Suitable for: FC; Reacts with Mouse  
[https://www.bdbiosciences.com/en-us/products/reagents/flow-cytometry-reagents/research-reagents/single-color-antibodies-ruo/buv395-rat-anti-mouse-cd8a.563786?tab=product\\_details](https://www.bdbiosciences.com/en-us/products/reagents/flow-cytometry-reagents/research-reagents/single-color-antibodies-ruo/buv395-rat-anti-mouse-cd8a.563786?tab=product_details)

anti-CD8-FITC (BD Pharmingen, 561966); Suitable for: FC; Reacts with Mouse  
[https://www.bdbiosciences.com/en-us/products/reagents/flow-cytometry-reagents/research-reagents/single-color-antibodies-ruo/fetc-rat-anti-mouse-cd8a.561966?tab=product\\_details](https://www.bdbiosciences.com/en-us/products/reagents/flow-cytometry-reagents/research-reagents/single-color-antibodies-ruo/fetc-rat-anti-mouse-cd8a.561966?tab=product_details)

anti-CD25-PE (BD Pharmingen, 558642); Suitable for: FC; Reacts with Mouse  
[https://www.bdbiosciences.com/en-us/products/reagents/flow-cytometry-reagents/research-reagents/single-color-antibodies-ruo/pe-rat-anti-mouse-cd25.558642?tab=product\\_details](https://www.bdbiosciences.com/en-us/products/reagents/flow-cytometry-reagents/research-reagents/single-color-antibodies-ruo/pe-rat-anti-mouse-cd25.558642?tab=product_details)  
 anti-Foxp3-APC (eBioscience, 17-5773-82); Suitable for: FC; Reacts with Mouse  
<https://www.thermofisher.com/antibody/product/FOXP3-Antibody-clone-FJK-16s-Monoclonal/17-5773-82>  
 anti-granzyme B-PE Cy7 (BioLegend, 372213); Suitable for: FC; Reacts with Human, Mouse  
<https://www.biolegend.com/ja-jp/products/pe-cyanine7-anti-humanmouse-granzyme-b-recombinant-antibody-15582>  
 anti-CD279-APC (BD Pharmingen, 562671); Suitable for: FC; Reacts with Mouse  
[https://www.bdbiosciences.com/en-us/products/reagents/flow-cytometry-reagents/research-reagents/single-color-antibodies-ruo/apc-hamster-anti-mouse-cd279-pd-1.562671?tab=product\\_details](https://www.bdbiosciences.com/en-us/products/reagents/flow-cytometry-reagents/research-reagents/single-color-antibodies-ruo/apc-hamster-anti-mouse-cd279-pd-1.562671?tab=product_details)  
 anti-CD279-FITC (BD Pharmingen, 561035); Suitable for: FC; Reacts with Human  
[https://www.bdbiosciences.com/en-us/products/reagents/flow-cytometry-reagents/research-reagents/single-color-antibodies-ruo/fic-mouse-anti-human-cd279.561035?tab=product\\_details](https://www.bdbiosciences.com/en-us/products/reagents/flow-cytometry-reagents/research-reagents/single-color-antibodies-ruo/fic-mouse-anti-human-cd279.561035?tab=product_details)  
 anti-LAG3-PE (BD Pharmingen, 552380); Suitable for: FC; Reacts with Mouse  
[https://www.bdbiosciences.com/en-us/products/reagents/flow-cytometry-reagents/research-reagents/single-color-antibodies-ruo/pe-rat-anti-mouse-cd223.552380?tab=product\\_details](https://www.bdbiosciences.com/en-us/products/reagents/flow-cytometry-reagents/research-reagents/single-color-antibodies-ruo/pe-rat-anti-mouse-cd223.552380?tab=product_details)  
 anti-SOX2-AF647 (BD Pharmingen, 560294); Suitable for: FC; Reacts with Human  
[https://www.bdbiosciences.com/en-us/products/reagents/microscopy-imaging-reagents/immunofluorescence-reagents/alexa-fluor-647-mouse-anti-sox2.560294?tab=product\\_details](https://www.bdbiosciences.com/en-us/products/reagents/microscopy-imaging-reagents/immunofluorescence-reagents/alexa-fluor-647-mouse-anti-sox2.560294?tab=product_details)

## Eukaryotic cell lines

Policy information about [cell lines and Sex and Gender in Research](#)

Cell line source(s)	GSC3028 was derived from a recurrent GBM from a 65-year-old female patient. MES28 and GSC23 were derived from recurrent GBM biopsy specimens and were provided as generous gifts by Dr. Erik Sulman (Duke Health). GSC2907 was derived from a GBM from a 58-year-old female patient. GSKR1 was derived from a GBM and transferred via a material transfer agreement from MD Anderson Cancer Center. GSC3264 was derived from a recurrent GBM from a 65-year-old female patient. ENSA (ENStem-A) is a human embryonic stem-derived neural progenitor cell (Millipore Sigma, Cat# SCC003). HNP1 (STEMEZ HNP1) is a human neural progenitor cell (Neuro-mics, Cat# HN60001). 293FT cells (Thermo Fisher Scientific, Cat# R70007) were derived from embryonic kidney cells from a female human. GL261 (Cytion, 305225) cell line is a murine glioma model derived from C57BL/6 mice. Mouse glioma stem cell MC9 was provided by Dr. Fan Lin (Nanjing Medical University).
Authentication	All cell lines were routinely subjected to STR testing to confirm their original identity.
Mycoplasma contamination	All cell lines were tested to confirm lack of mycoplasma contamination.
Commonly misidentified lines (See <a href="#">ICLAC</a> register)	No cell line used in the paper is listed in ICLAC database.

## Animals and other research organisms

Policy information about [studies involving animals](#); [ARRIVE guidelines](#) recommended for reporting animal research, and [Sex and Gender in Research](#)

Laboratory animals	Lyz2-cre and Slc16a3-flox (T011091) mice were obtained from GemPharmatech. C57BL/6J (GemPharmatech, Cat# N000013) and BALB/c-Nude mice (GemPharmatech, Cat# D000521), 4-6 weeks old, were randomly selected for intracranial injection. All murine experiments were performed under an animal protocol approved by the Institutional Animal Care and Use Committee (IACUC-2006033) at Nanjing Medical University in accordance with NIH and institutional guidelines. Mice had not undergone prior treatment or procedures. Mice were maintained in 14 hours light/10 hours dark cycle by animal husbandry staff at the Nanjing Medical University, with no more than 5 mice per cage. Experimental animals were housed together. Housing conditions and animal status were supervised by a veterinarian.
Wild animals	We did not use any wild animals.
Reporting on sex	Both male and female mice were used in studies.
Field-collected samples	No field-collected samples were used in this study.
Ethics oversight	All murine experiments were performed under an animal protocol approved by the Institutional Animal Care and Use Committee (IACUC-2006033-2) at Nanjing Medical University in accordance with NIH and institutional guidelines.

Note that full information on the approval of the study protocol must also be provided in the manuscript.

## Plants

Seed stocks	Report on the source of all seed stocks or other plant material used. If applicable, state the seed stock centre and catalogue number. If plant specimens were collected from the field, describe the collection location, date and sampling procedures.
Novel plant genotypes	Describe the methods by which all novel plant genotypes were produced. This includes those generated by transgenic approaches, gene editing, chemical/radiation-based mutagenesis and hybridization. For transgenic lines, describe the transformation method, the number of independent lines analyzed and the generation upon which experiments were performed. For gene-edited lines, describe the editor used, the endogenous sequence targeted for editing, the targeting guide RNA sequence (if applicable) and how the editor was applied.
Authentication	Describe any authentication procedures for each seed stock used or novel genotype generated. Describe any experiments used to assess the effect of a mutation and, where applicable, how potential secondary effects (e.g. second site T-DNA insertions, mosaicism, off-target gene editing) were examined.

## Flow Cytometry

### Plots

Confirm that:

- ☒ The axis labels state the marker and fluorochrome used (e.g. CD4-FITC).
- ☒ The axis scales are clearly visible. Include numbers along axes only for bottom left plot of group (a 'group' is an analysis of identical markers).
- ☒ All plots are contour plots with outliers or pseudocolor plots.
- ☒ A numerical value for number of cells or percentage (with statistics) is provided.

### Methodology

Sample preparation	Tumor-derived GSCs or tumor infiltrating lymphocytes were stained directly from single-cell preparations of dissected tumors as described in materials and methods.
Instrument	LSR Fortessa (BD)
Software	BD DIVA software was used for data collection. FlowJo v.10 software was used for analysis.
Cell population abundance	The population abundance was analyzed with FlowJo v.10.
Gating strategy	All gates were set based on naive mice spleen and isotype control antibodies after appropriate compensation using single-stained compensation controls.

- ☒ Tick this box to confirm that a figure exemplifying the gating strategy is provided in the Supplementary Information.